Multiscale Tunable Hybrid Biomaterials for Engineering Human iPSC-Based Cardiac Microphysiological Systems

Jonathan H. Tsui

A dissertation

submitted in partial fulfillment of the

requirements for the degree of

Doctor of Philosophy

University of Washington

2019

Reading Committee:

Deok-Ho Kim, Chair

Cole A. DeForest

Nathan J. Sniadecki

Program Authorized to Offer Degree:

Department of Bioengineering

University of Washington

Abstract

Multiscale Tunable Hybrid Biomaterials for Engineering Human iPSC-Based Cardiac Microphysiological Systems

Jonathan H. Tsui

Chair of the Supervisory Committee:

Deok-Ho Kim, Ph.D., Associate Professor

Department of Bioengineering

Human induced pluripotent stem cells (hiPSCs) offer tremendous potential for use in engineering human tissues for disease modeling, drug development, and cell therapy. However, differentiated cardiomyocytes are phenotypically immature, reducing assay reliability when translating *in vitro* results to clinical studies and precluding hiPSC-derived cardiac tissues from therapeutic use *in vivo*. To address this, we have developed hybrid hydrogels comprised of decellularized myocardial extracellular matrix (dECM) and reduced graphene oxide (rGO) to provide a more instructive microenvironment for proper cellular and tissue development. A tissue-specific protein

profile was preserved post-decellularization, and through the modulation of rGO content and degree of reduction, the mechanical and electrical properties of the hydrogels could be tuned. Engineered heart tissues (EHTs) generated using dECM-rGO hydrogel scaffolds and hiPSC-derived cardiomyocytes exhibited significantly increased twitch forces even after only 14 days of culture, and the expression of genes that regulate contractile function were also increased. Similar improvements in various aspects of electrophysiological function, such as calcium-handling, action potential duration, and conduction velocity, were also induced by the hybrid biomaterial. Notably, this included a drastic upregulation of genes encoding potassium ion channels and connexin 43 gap junction proteins. dECM-rGO hydrogels could be used as a bioink to bioprint cardiac tissues in a high-throughput manner, and these tissues were utilized to assess the proarrhythmic potential of cisapride. The onset of action potential duration prolongation and beat interval irregularities was observed in dECM-rGO tissues at clinical doses, indicating that the enhanced maturation of these tissues corresponded well with a capability to produce physiologically-relevant drug responses. Taken together, this research demonstrates the versatility of dECM-rGO hydrogels and the feasibility of combining the unique pro-maturation material properties of both components to engineer more functionally developed tissues that are suitable for modeling the adult human myocardium.

Table of Contents

List of Figures

List of Tables

Acknowledgements

I would like to first thank my advisor, Prof. Deok-Ho Kim, for providing the guidance and support that I needed to succeed as a graduate student. Beginning from day one, you were incredibly open-minded and passionate about my research projects, and you continually provided the training, advice, and resources that I needed to pursue my dreams of one day becoming a professor with my own lab.

I would like to thank the members of my supervisory committee, Prof. Charles Murry, Prof. Cole DeForest, Prof. Nathan Sniadecki, and Prof. Jeffrey Chamberlain, for their expertise and invaluable feedback on my thesis work. You have inspired me to uphold a standard of scientific excellence that I hope to maintain and pass on for the rest of my career.

It would hardly be hyperbole if I were to say that without the support of my colleagues and friends in the Kim, Sniadecki, and Murry Labs, I would have struggled mightily to produce the work that I have. Their willingness to freely share their insights, knowledge, and companionship with me is truly appreciated. In no particular order, many thanks go to Dr. Alec Smith, Nisa Williams, Travis Moerk, Som Chavanachat, David Yama, Joseph Long, Elisa Clark, Saffie Mohran, Dr. Andrea Leonard, Zeid Nawas, Dr. Jesse Macadangdang, Dr. Alex Jiao, Dr. Kajohnkiart Janebodin, Dr. Nick Ieronimakis, Dr. Sam Frankel, Paulos Mengsteab, Jasmine Rinnofner, Marcus Rhodehamel, John Foster, Ty Higashi, Nicholas Neal, Yu Jung Shin, Dr. Jong Seob Choi, Changho Chun, Hyejin Kim, Dr. Joy Su, Cameron Nemeth, Dr. Lil Pabon, Dr. Peter Kim, and Dr. Kshitiz.

A tremendous amount of gratitude goes towards Dr. Blake Bluestein, Dr. Bob Lamm, Dr. Andrew Wang, Dr. Jason Stevens, and Dr. David Younger. You are some of the most talented, brilliant, and generous people I have ever met, and are also the greatest group of friends that anyone could ever ask for. It has been a privilege to have gone through this graduate school experience with you all, and I look forward to seeing what you accomplish in the years to come.

I would also like to take this opportunity to thank Prof. Daniel Kohane, Prof. Lawrence Bonassar, Stephen Marsden, and Larry Axelrod. Prof. Bonassar provided the opportunity for me as an undergraduate student to get my first real taste of research, while Prof. Kohane gave me the confidence and courage I needed to embark on this journey of becoming an independent scientist. Mr. Marsden and Mr. Axelrod were the two incredible teachers in high school who, through their own passion for the sciences, lit the spark that started it all.

Finally, and most importantly, I would like to thank Mom and Dad for their constant love, support, patience, and encouragement. You have pushed me to be the best that I can be every step of the way, helped me grow as a person, and have had to make numerous sacrifices to get me to where I am today. I hope I've made you proud.

This work was supported by National Institutes of Health grants R01 HL135143, R21 EB020132, and UG3 EB028094, as well as by as well as by American Heart Association pre-doctoral fellowship 16PRE30760018, and by National Institutes of Health training grant TL1 TR002318.

Chapter 1. Introduction

1.1 Cardiac Tissue Engineering and Implications for Human Health

Cardiovascular disease (CVD) remains a leading cause of death for both men and women worldwide, with the economic costs of healthcare related to treatment or quality of life improvements forecasted to exceed $1 trillion per year in the United States alone by 2030[1,2]. The devastating impact of CVD is largely due to the limited regenerative ability of the heart, especially after suffering from chronic or acute injury, with a cardiomyocyte turnover rate of only 1 – 2% per year[3]. With the healthcare burden of CVD only increasing every year, considerable research efforts are expended to not only better understand the underlying disease pathologies, but to also use these findings to develop improved pharmacological treatments. However, the non-proliferative nature of terminally differentiated cardiomyocytes has served as a bottleneck for such work, as obtaining sufficient numbers of cells for studies is difficult and time-consuming. Animal models have provided tremendous insight into the basic biology and pathophysiology underlying CVDs, and the establishment of transgenic and gene knock-out strains that mimic the genetic abnormalities seen in human patients have contributed to important discoveries[4-8]. Unfortunately, despite these advances, significant differences in physiology between animals and humans have limited the translational utility such models. For example, mismatches in genetic profile, pharmacokinetics, disease progression, and cardiac function have often led to aborted clinical trials where promising results seen in animal studies were not able to be replicated in human trials[9-11]. Furthermore, large-scale animal studies are costly

and low throughput, leading to increased time to translate research discoveries to patient care. As such, cardiac tissue engineering has emerged as a potential solution to these barriers to cardiovascular research[12]. The ultimate goal of this concept is to be able to generate fully functional three-dimensional (3D) human cardiac tissues *de novo* through the use of cells that are grown in a culture microenvironment that provides the appropriate developmental cues. If successful, these tissues can serve as biologically-relevant models for the *in vitro* study of cardiac physiology[13] or as an implantable therapy for *in vivo* regeneration and repair.

1.1.1 *In Vitro* Applications of Engineered Cardiac Tissues

In the realm of drug discovery and development, a significant concern and regulatory hurdle is drug-induced cardiotoxicity. Cardiotoxic effects have contributed to a very high attrition rate of drug candidates and are the cause of the most frequent serious adverse drug reactions that result in drug withdrawal from market[14,15]. In fact, it has been found that safety liabilities related to cardiovascular toxicity account for 45% of the total post-approval drug withdrawals from the market[16]. Based on these observations, it is evident that there is a need for better screening assays that can accurately predict the cardiotoxic risk of drugs before they are approved for usage in in late-stage preclinical and clinical trials. Historically, initial toxicity testing has been performed with immortalized or primary cell lines cultured on simple two-dimensional (2D) polystyrene substrates, with the premise that this simplification of organ systems can assist in increasing assay throughput and analysis of functional outputs. However, it is becoming increasingly obvious that these models do not fully recapitulate the

function of the tissues being investigated, and a shift has been made towards the use of engineered cardiac tissues that are better mimics of their *in vivo* counterparts. In two similar approaches, neonatal rat cardiomyocytes were seeded in fibrin-based hydrogels to form 3D tissue-like constructs[17,18]. Formed tissues exhibited an expression profile of cardiac-specific contractile proteins and ion channels that suggested that they would respond appropriately to administered drug compounds. These tissues were cast around flexible silicone posts that allow for the measurements of tissue force production in response to cardiotoxic drugs such as doxorubicin, quinidine, and erythromycin. When exposed to these drugs, the engineered tissues developed arrhythmic behavior as expected; however, obtained IC_{50} values were much higher than those seen clinically, indicating that these tissues were not quite fully representative of native human tissues. Recent developments in human stem cell technologies have allowed researchers to generate humanized tissues that are an even further improvement on prior approaches, particularly with respect to drugs that are human-specific and cannot be tested in animals. Mathur et al. utilized cardiomyocytes derived from human induced pluripotent stem cells (hiPSCs) to develop a cardiac microphysiological system in which 3D cardiac tissues were formed within a microfluidic perfusion chamber that enabled the precise delivery of drugs from “vascular” channels[19]. When combined with a custom-made motion-tracking software, they were able to demonstrate physiologically relevant changes in cardiac contraction kinetics in response to increasing doses of a number of cardiotoxic compounds, including verapamil and metoprolol. In order for engineered tissues to make an impact in cardiotoxicity screening, however, improvements still need to be

made since cost-effective drug discovery is predicated on the ability to screen hundreds, if not thousands, of candidate compounds so that resource allocation can be managed correctly.

In vitro disease modeling has also emerged as an area in which engineered human cardiac tissues have been proposed to play a significant role. While various animal models have been developed that approximate the pathological effects of cardiomyopathies, disease progression in these models are often different from that seen in human patients. With the ability to induce or replicate mutations in cells with genome editing techniques like CRISPR-Cas9 and adeno-associated virus transduction, tissues can now be engineered with modified cells to better replicate dysfunctions observed *in vivo*. In one example, engineered cardiac tissues were even able to examine a hypothesis that a mutation of FHL1, a protein thought to contribute to sarcomere synthesis, assembly and biomechanical stress sensing, that was identified in human patients with hypertrophic cardiomyopathy contributed to the disease phenotype[20]. AAV-mediated transduction was used to impart this mutation to murine cardiomyocytes, and alterations in contractile function were seen in myocardial tissues engineered with these cells. Other techniques have involved the physical manipulation of engineered tissues to replicate disease states, such as inducing pathological hypertrophy by increasing afterload *via* mechanical restriction of beating tissues[21] or producing tachycardia by generating ring-shaped tissues that promoted the formation of reentrant propagation waves[22]. The transition into using patient-derived hiPSCs to generate disease models is becoming more widespread, and in one study, hiPSCs from an individual with long QT syndrome type 3 (LQT3) was used to

form tissues that reproduced the electrophysiological abnormalities that are associated with this disease[23]. Moving forward, it is anticipated that as engineered cardiac systems become more advanced, disease-on-a-dish models can be combined with drug screening to investigate the therapeutic potential of compounds that are either under development or have been hypothesized to have beneficial off-label effects.

1.1.2 Engineered Cardiac Tissues as for *In Vivo* Therapy

Due to the non-regenerative nature of the damaged human heart, whole organ transplants are currently the only method of successfully treating heart failure. As a result, researchers have turned to the idea of replacing injured tissues with viable, functional tissues or organs that are engineered and grown in the laboratory. An early example of this approach is the study conducted by Leor et al., in which fetal cardiac cells were seeded within alginate scaffolds[24]. In the study, cells were cultured within scaffolds for 4 days before the entire construct is implanted into a rat model for MI with the use of sutures. Rats were assessed with echocardiography, then sacrificed 9 weeks post-implantation and their cardiac tissue was examined histologically. Intense neovascularization into the cell-seeded scaffold was observed, and cells appeared to be able to form striated myofibers and cellular gap junctions, although the arrangement of these features were often found to be random, as opposed to in a parallel fashion as seen in native myocardium. Echocardiography data revealed an attenuation of LV remodeling in treated rats and a preservation of baseline fractional shortening. Conversely, sham-operated rats developed progressive LV dilation. These results

demonstrate the feasibility of implanting engineered tissue constructs at the site of infarction as a form of treatment. However, the brief culture period of the fetal cardiomyocytes and the observation that the organization of grafted tissue was dissimilar to that of host tissue are significant concerns. Without establishing methods of first maturing seeded cardiomyocytes before implantation, there is no guarantee that although LV remodeling is attenuated, restoration of cardiac function can likewise be achievable. Similar results have been achieved by groups that have seeded cells into scaffolds comprised of other biocompatible and biodegradable materials such as Matrigel[25,26], collagen type I[27], and poly(lactic-co-glycolic acid) (PLGA)[28]. Zimmermann et al. sought to improve cardiomyocyte maturation prior to implantation by placing cell-seeded scaffolds under a 10% static load for the last week of culture, and this appeared to improve cellular morphology and phenotype within the implant[25]. It was noted, however, that host immune response appeared to completely degrade the engrafted tissues in the absence of immunosuppression. This was likely due to the presence of allogenic non-soluble matrix components within the Matrigel, highlighting the need for further advancements in biomaterials development. Furthermore, the cardiomyocytes used in this study were sourced from neonatal rats, raising the possibility of eventual cardiac dysfunction due to the aforementioned differences in animal and human physiology.

Formation of mature cardiac tissue during development does not occur in controlled, static environments, and attempts to mimic these conditions during cell culture have been made to address concerns regarding cardiomyocyte maturity, organization, and sufficient nutrient flow through thick tissue constructs. One strategy is

to use scaffolds subjected to pulsatile flow regimens, a technique commonly referred to as a bioreactor system[29]. With perfusion, Radisic et al. were able to generate tissues with thicknesses up to 650 μm, with viable cells uniformly distributed throughout. Brown et al. demonstrated the advantages conferred by a bioreactor in which cell-seeded collagen sheets are cultured under pulsatile perfusion conditions at high (1.50 mL/min) and low (0.32 mL/min) flow pulsed at a frequency of 1 Hz[30]. Engineered tissues under PP conditions displayed a lower excitation threshold compared to static controls, as well as significantly increased contraction amplitudes. Pulsatile perfusion also appeared to increase cellular hypertrophy, as cardiomyocytes cultured under these conditions were observed to be larger in both diameter and length. Unfortunately, only slight differences were observed for other phenotypical markers, although it should be noted that the 1 Hz pulsatile flow frequency used in this study is physiological for human cells, and the cells utilized were derived from neonatal rats. It is thus possible that adjusting the pulse frequency could generate even more mature tissue constructs. Cyclic mechanical stretch protocols have been shown to improve cell differentiation in other studies, but some hallmarks of differentiated cardiac tissue were still found to be missing (such as M bands and intercalated (IC) disks)[31]. This concept has been taken to an even more complex level where by gradually increasing the frequency intensity of contractions in hiPSC-derived engineered tissues through electrical stimulation, a corresponding increase in tissue maturity was observed[32]. However, even with this technique, the development of the electromechanical function of these tissues was still delayed and did not achieve the stage of maturity seen in the adult human myocardium. Therefore, though promising, the evidence suggests that mechanical

stresses alone cannot fully ensure differentiation of seeded cells, and that other cues may be required.

From the examples given above, it is clear that for cardiac tissue engineering to succeed as a viable strategy for combating CVD, the appropriate combination of cell source, scaffold material, and culture microenvironment must be optimized such that functional and physiologically-representative cardiac tissues can be generated.

1.2 Human Induced Pluripotent Stem Cells: Applications and Limitations

Human induced pluripotent stem cells (hiPSCs) are a tractable source of cardiomyocytes for a variety of applications, as they are amenable to both scaled production and genetic manipulation[33,34]. Unlike human embryonic stem cells (hESCs), iPSCs are generated by reprogramming adult somatic cells, such as dermal fibroblasts, with the forced expression of stem cell-related transcription factors[34] or miRNAs[35], thereby avoiding the destruction of human embryos and the ethical roadblocks that are associated with that process. As highlighted previously, there is a current unmet need for representative *in vitro* models capable of serving as drug screening or disease modeling platforms. While the use of 3D tissues engineered from hiPSC-derived cardiomyocytes (hiPSC-CMs) for these purposes is ideal, cultured monolayers of these cells can serve as a short-term stopgap method.

When differentiated, hiPSC-CMs have been shown to possess all major types of ion channels that are present in adult cardiomyocytes[36]. This is immensely useful for cardiotoxicity drug screening assays since many of the most serious forms of drug-

induced adverse events impact electrophysiological function. Indeed, several studies have demonstrated the utility of these cells in high-throughput screens of drugs with known QT prolongation effects[37,38]. Additionally, the derivation of hiPSCs from adults has allowed for the generation of disease- or patient-specific cell lines that enable further use in modeling inherited dysfunctions[39]. A prominent example is that of channelopathies such as long QT syndrome (LQTS) which is characterized by a propensity for Torsades de Pointes (TdP), a form of polymorphic ventricular tachycardia. hiPSC-CMs containing mutations in the potassium channels (KCNQ1 and KCNH2) responsible for Type I and Type II LQTS have not only been able to exhibit prolonged action potential durations and reduced inward potassium currents, but have also been used with some success to screen for novel therapeutics capable of improving electrophysiological function[40-43]. Similarly, hiPSC lines containing mutations that cause inherited disorders affecting sarcomeric organization and hypertrophic cardiomyopathies have been developed, with hiPSC-CMs differentiated from these lines able to recapitulate numerous aspects of the disease[44,45].

Although hiPSC-CMs are good candidates for use in drug screening, disease modeling, and tissue engineering, they are not without their limitations. While cells differentiated from pluripotent sources possess a definite cardiac identity, they are typically developmentally immature and exhibit structural and functional characteristics that are significantly different from those of adult cardiomyocytes[46]. Morphologically, hiPSC-CMs tend to be circular and lack a functional transverse tubule (T-tubule) network. Sarcomeric organization is also in disarray, with much shorter sarcomere lengths and Z-band widths. Various indications of impaired electrophysiological function,

such as a relatively depolarized resting membrane potential, slower upstroke and conduction velocities, and slow Ca^{2+} response, suggest an overall deficiency in ion channel functional density[47,48]. Additionally, the profile of myofibrillar protein isoforms in hiPSC-CMs is more akin to that of a fetal rather than adult stage of development, with a higher proportion of N2BA titin, α-myosin heavy chain (α-MHC), and slow skeletal troponin I (ssTnI). This underdeveloped state of differentiated cardiomyocytes has serious implications for their suitability for downstream applications since the clinical relevance of the results obtained from studies utilizing these cells is predicated on their ability to accurately recapitulate the properties of the adult native myocardium. Therefore, a significant thrust of the field is towards investigating a variety of methods to engineer more biomimetic cardiac niches that are capable of promoting the proper development and functional maturation of hiPSC-CMs.

1.3 Biomaterials for Human Cardiac Tissue Engineering

An important factor to consider when attempting to faithfully recreate the myocardial niche is the inclusion of a 3D culture environment to more closely mimic cell-cell and cell matrix mechanics and structural organization. In native tissue, the extracellular matrix (ECM) provides the specific physical and biochemical cues that enable the proper development and function of all biological tissues (**Figure 1.1**)[49]. To this end, a multitude of biomaterials have been used and developed to provide microenvironments that are supportive of cell growth, organization, and maturation. Due to the wide array of biomaterials available for fabricating scaffolding, each with their own inherent advantages and disadvantages, a single “optimal” scaffold has yet to be established,

illustrating the fact that there currently remains substantial room for further development and improvement.

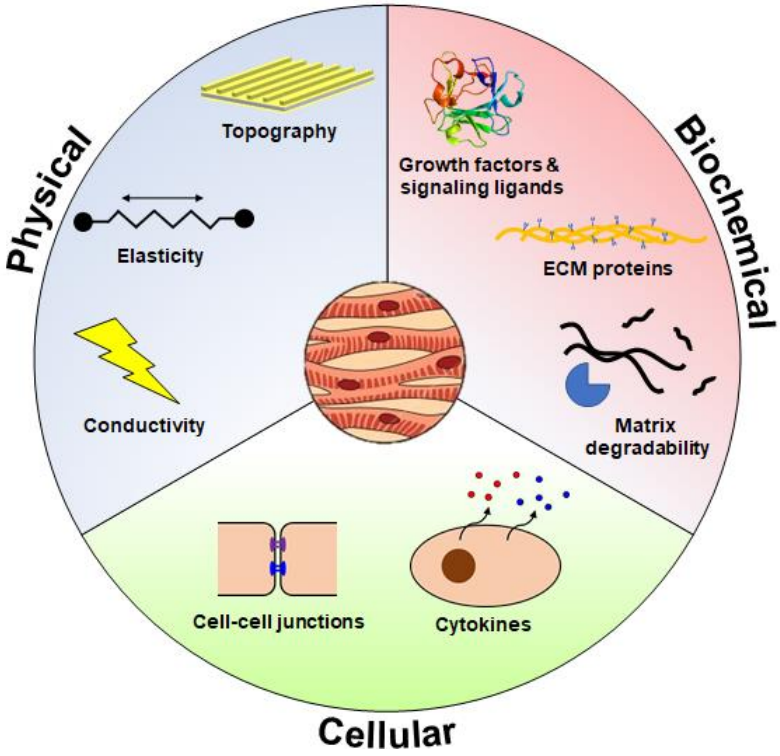

Figure 1.1. The tissue microenvironment encompasses a multitude of cues that direct cell fate and function. Current scaffold design is focused on recapitulating these cues to their fullest extent so that physiologically-representative tissues can be successfully engineered.

1.3.1 Naturally-Derived Materials

Naturally-derived polymers are an attractive option for use in tissue engineering due to their high biocompatibility and biodegradability, and are generally more representative of the native tissue microenvironment. Perhaps the most widely used material is collagen type I[31,50-52]. As it is the most abundant protein in mammalian tissues and is the main component of the ECM[53], collagen offers a degree of inherent cell-adhesiveness and biomimicry that is often unmatched by other materials. When enzymatically digested, neutralized collagen solutions can be formed into self-

assembled porous hydrogels that are well-suited for cell encapsulation and the diffusion of nutrients and waste[54]. However, the slow gelation rate of collagen is sometimes a significant issue, as cells could settle before the gel is fully crosslinked, leading to a heterogenous distribution in the resulting tissue. To address this, researchers have often used a mixture of fibrin and collagen or simply fibrin alone to form hydrogel scaffolds[32,55-57]. Fibrin is the biopolymer form of fibrinogen and both have critical roles in blood clotting and wound healing processes in the body[58]. Because of this, fibrin crosslinks very rapidly and is therefore better able to preserve the desired structure and cell distribution of engineered tissues. Furthermore, fibrin can be easily modified using a transglutaminase-catalyzed reaction to include signaling peptide groups such as RGD and YIGSR thereby increasing the bioactivity of the resulting scaffold[59].

In an alternative approach, Matrigel, a material derived from the basement membrane secreted by Engelbreth-Holm-Swarm (EHS) mouse sarcoma cells, has been used in combination with fibrin or collagen to further increase cell viability and attachment due to its various growth factors, hormones, and matrix components[60]. Like fibrin, it has been demonstrated that Matrigel can be used either alone or in combination with other materials to form scaffolds[61]. However, Matrigel is much more expensive than the aforementioned polymers and lot-to-lot variation can be quite high, making it a relatively poor candidate for applications that require large scale fabrication.

Closely related to collagen are decellularized extracellular matrices (dECM)[62-64]. In the context of engineering cardiac tissues, dECM is usually derived from freshly-harvested animal hearts that have had their cellular components removed using a detergent-mediated process. The single major advantage of utilizing dECM or dECM-

based materials is that their inherent biochemical composition is nearly identical to that of the native ECM's and is thus potentially one of the best and simplest methods currently available for recapitulating tissue-specific and pro-maturation cues in a scaffold. dECM can be solubilized and reformed into hydrogels to form 3D constructs, but like collagen, the crosslinking rate of these hydrogels is quite low. Alternatively, dECM sheets can be utilized instead to not only preserve tissue biochemical cues, but to also preserve matrix topographical cues to aid in cell guidance. However, ensuring a homogenous cellular distribution through sheet scaffolds is often difficult, leading to the possibility of areas within the engineered tissue where no cells are present.

Alginate is an anionic polysaccharide derived from brown algae and has a long history of use in the food and pharmaceutical industries. Its ability to form porous hydrogels with the simple addition of divalent cations such as Ca^{2+} make it an attractive biomaterial for use as tissue engineering scaffolds. Although traditionally not as commonly used as collagen for engineering cardiac tissues, alginate use has become more widespread in recent years as a supplementary scaffold material, particularly in tissue bioprinting applications[65], due to its rapid crosslinking properties. Alginate's polymer backbone also lends itself well to chemical modification *via* carbodiimide chemistries, with numerous reports describing the addition of side groups that assist with cell adhesion and signaling[66,67].

Gelatin methacrylate (GelMA) is comprised of denatured collagen that has been chemically modified to include methacrylate groups that in the presence of a photoiniator can be photocrosslinked on demand[68,69]. This property has also made GelMA an attractive option for tissue bioprinting and 3D micropatterning applications

where very rapidly and precisely crosslinked hydrogels can be utilized to generate tissue constructs with complex architectures but still retain a cell-supportive microenvironment[70,71]. With this crosslinking mechanism, hydrogel pore sizes and modulus can also be accurately tuned, thereby increasing the versatility in the mechanical cues with which a single scaffold can present.

Despite their widespread use and noted advantages, naturally-derived biomaterials are often most lacking in their mechanical properties, as many of the hydrogels formed with these materials feature elastic moduli that are far below that of the native myocardium. This is a critical factor to consider as prior studies have found that the development of cardiomyocyte contractile function and striation is significantly improved in microenvironments that closely approximate myocardial stiffnesses[72-74].

1.3.2 Synthetic Materials

In contrast to their naturally-derived counterparts, synthetic materials offer greater flexibility and reproducibility in tailoring the structural, mechanical, electrical, and biochemical properties, but at a cost of low inherent bioactivity and biocompatibility. Some of the most frequently used synthetic materials in tissue engineering applications are thermoplastic biodegradable polymers such as polylactide (PLA), polyglycolide (PGA), poly(lactic-co-glycolic acid) (PLGA), poly(ε-caprolactone) (PCL), and their copolymers[75]. They are inexpensive, well-characterized, and perhaps most importantly, have been approved by the Food and Drug Administration (FDA) for clinical use. However, they are also significantly stiffer than the tissues they are supposed to model and often require additional functionalization with peptide groups in order to support cell

growth and development[76]. Additionally, these polymers cannot be formed into hydrogels, so in order to create porous 3D matrices, they must be either templated during scaffold fabrication, electrospun, or used in combination with another material that is capable of forming a hydrogel matrix.

Poly(ethylene glycol) (PEG) hydrogels have also been used with good results as a scaffold material. One of the major advantages of PEG is the ease with which it can be molded and patterned[77] to, for example, better mimic native tissue nanotopographical cues. Studies have shown that anisotropically nanofabricated substratum (ANFS) formed from PEG hydrogels with a range of groove and ridge widths (150 nm to 800 nm) and ridge heights (200 nm to 500 nm) that best match the dimensions of ECM fibrils in the myocardium are capable of promoting cardiomyocyte organization, sarcomere development, and hypertrophy[78,79]. Unfortunately, due to its relatively hydrophobic nature, PEG also requires the addition of cell-adhesive motifs to improve cell viability and biocompatibility[80]. However, with its relatively simple polymer structure, PEG lends itself well to several chemical modification schemes that impart functionalities such as photocrosslinkability[81,82] and enzymatic degradation[82-84].

One of the newest classes of synthetic materials that is seeing increasingly widespread use in biological applications is that of carbon-based nanomaterials such as graphene, graphene oxide (GO), and carbon nanotubes (CNTs)[85]. The single-layered lattices of sp^2 hybridized carbon that are the basis of these materials are what imbues them with their prized mechanical strength and high conductivity. Additionally, the presence of reactive oxygen sites in GO facilitates the covalent attachment of functional molecules. However, even in their unmodified state, carbon-based nanomaterials are

capable of supporting the adhesion and proliferation of a variety of mammalian cells including neurons[86], human mesenchymal stem cells (hMSCs)[87], human osteoblasts[88], hiPSCs[89], and human embryonic stem cells (hESCs)[90] without additional functionalization. Remarkably, both graphene and graphene oxide substrates have shown an ability to drive hiPSC and hESC differentiation towards mesodermal lineages and induce an upregulation of genes involved in cardiomyogenic development[89,90]. Although the precise mechanisms behind these processes is still poorly understood, usage of these types of materials in cardiac tissue engineering scaffolds may prove to be beneficial.

1.3.3 Hybrid Materials

Advances in polymer chemistry have allowed for further improvements in the versatility and functionality of materials used to create scaffolds for 3D cardiac tissue engineering. An area in which rapid progress has been seen in recent years is the development of so-called hybrid materials, where synthetic and natural materials are combined to take full advantage of the respective properties that are best suited for promoting tissue formation and maturation.

The most basic concept of this approach is the homogenous mixing of one or more materials, typically the synthetic component, with another to form a composite biomaterial, and one of the most common applications of this is the mechanical reinforcement of natural polymer hydrogels in order to increase the overall stiffnesses such that they are better approximations of tissue moduli[91,92]. For instance, the increased matrix elasticity that was achieved through the addition of PLGA and PLA-

PCL copolymers to collagen hydrogels led to an overall increase in contractile function and connexin 43 (Cx43) gap junction formation in engineered cardiac tissues[93]. When carbon-based nanomaterials or gold (Au) are used as the synthetic component, enhancement of mechanical properties is further supplemented by the presentation of electroconductive cues[94-96]. In electroconductive rGO-GelMA[91], CNT-GelMA[97], Au-pHEMA[98], and graphene-PEG[99] hydrogels, significant improvements in cardiomyocyte electrophysiological function, Cx43 expression, and myofibril protein expression were observed compared to cells cultured in non-hybrid scaffold controls. Nanoparticles can also be incorporated into hydrogel matrices to impart dynamic functional capabilities such as externally-triggered shape changes and on-demand delivery of bioactive factors[100].

Hybrid materials can also be synthesized through covalent modification or copolymerization to generate matrices with highly-controllable properties. For example. hydrogels formed from the conjugation of glycidyl methacrylate with PEG-peptides featured tunable enzymatic degradation rates and photocrosslinking-mediated stiffnesses[101]. Electroconductivity can also be imparted onto non-conductive biological materials using covalent deposition techniques; culture of hESC-derived cardiomyocytes on nanopatterned silk fibroin hydrogels functionalized with poly(pyrrole) (PPy) induced anisotropic organization and increased expression of Cx43, and the expression of genetic markers indicative of cardiac maturation[102]. With the knowledge that cardiomyocyte function can be significantly impacted by dynamic changes in ECM stiffness and elasticity as a result of disease progression or developmental processes, there exists a need for scaffolds that can replicate these scenarios. In one approach, Liu

et al. developed protein-polymer hydrogels that employed chemoenzymatic modification of PEG to enable the reversible and spatiotemporally-controlled modulation of matrix stiffness in response to external stimuli[103]. With this material, it was demonstrated that induced cyclic mechanical loading could drive myofibroblast activation and could therefore potentially serve as a platform for studying the role that dynamic mechanics plays in fibroblast transdifferentiation. It is also well known that cellular differentiation and overall tissue morphogenesis is regulated by well-defined gradients of biological factors during development. The functionalization of agarose hydrogels with thiol groups that could be photodeprotected enabled the immobilization of FGF2 with 3D spatial control[104], while the utilization of orthogonal click chemistries to attach small molecules to PEG hydrogels enabled their stimuli-triggered release at user-defined concentrations[105]. Strategies such as these have the potential to recapitulate the variable biochemical signaling encountered by cells *in vivo* and therefore lead to substantial improvements in generating developmentally-appropriate tissues.

1.4 Three-Dimensional Tissue Biofabrication Techniques

In addition to identifying the relevant cell types and optimal scaffolding biomaterials for engineering cardiac tissues, strong consideration must also be given to the specific processes used to fabricate these constructs.

The current gold standard for fabricating 3D cardiac tissues is what is commonly referred to as the engineered heart tissue (EHT) method that was first established by Eschenhagen and colleagues[50]. Generally speaking, this process involves the casting of a hydrogel-cell mixture in a mold around two-post arrays that are typically made from

silicone and are designed to impart passive tension to induce the anisotropic organization of the EHT. Once the tissues have formed and are suspended between the posts, their contractile function can be assessed *in situ* by measuring post deflections that can then be converted into force outputs, while electrophysiological function can be investigated through the use of fluorescent calcium- or voltage-sensing dyes[17,22,31,32,61,106]. Furthermore, these posts can be braced by additional components to increase mechanical loading or afterload on the EHTs, which has been demonstrated to induce improved cardiac maturation[56]. A similar tissue fabrication technique, named "biowire", was described by Nunes et al., where stem cell-derived cardiomyocytes encapsulated in a collagen hydrogel were cast into a poly(dimethysiloxane) (PDMS) channel around a sterile suture. Like the two-post platforms, once seeded cells had remodeled and contracted the surrounding matrix around the suture, the formation of tissues with high cellular alignment was achieved[52]. These and similar techniques are not without their drawbacks, however. While the casting process itself is straightforward, the use of ancillary components like molds and posts necessitates additional labor-intensive fabrication steps which can introduce unwanted variability to overall tissue quality.

Tremendous strides have been made in adapting additive manufacturing, or 3D printing, technologies for tissue engineering applications. Known as bioprinting, these techniques allow for the precise deposition of multiple materials in an automated and reproducible manner. Some of the earliest example of bioprinted tissue constructs consisted of a single layer of dECM hydrogel bioink extruded directly onto tissue culture polystyrene in simple square waves or as text[107]. These designs gradually evolved into

multiple layers of different cell types that were deposited within a slightly more complex series of PCL support lattices arrayed either in a cube or in the shape of anatomical structures like the ear[63,108,109]. Development of techniques like FRESH that utilize sacrificial structures or baths that temporarily support printed tissues further increased complexity and versatility, as these methods now allowed for the use of bioinks that were previously deemed too mechanically weak to form multilayered constructs[110,111]. Recently, Grigoryan et al. have reported on the ability to use synthetic and natural food dye photoabsorbers in conjunction with photocrosslinkable PEG diacrylate (PEGDA) hydrogels to stereolithographically print perfusable entangled 3D networks of a heretofore unachievable level of complexity[112]. Remarkably, with this method a fully functioning distal lung subunit, complete with a ventilating air sac that oxygenated the blood in the surrounding vasculature, could be printed. From these studies, it is evident that the high degree of spatial control over tissue composition in a complex three-dimensional space that bioprinting offers is a significant improvement over more conventional methods and represents the ability to generate truly physiologically and anatomically accurate models. Bioprinting has also enabled the facile fabrication of instrumented cardiac microphysiological devices *via* multimaterial printing. By sequentially depositing functional polymer bioinks that were piezo-resistive, highly conductive, and biocompatible, soft strain gauge sensors capable of providing real-time contractile function measurements could be integrated directly into organized cardiac tissues[113]. Despite the rapid advances in the field, however, significant improvements in biomaterials science and printing hardware must still be made in order for bioprinting to

fully realize the potential to generate full-thickness tissues or whole organs comprised of multiple hierarchically-organized tissues.

Even with the use of biocompatible and biodegradable materials as tissue engineering scaffolds, some degree of foreign body response is still observed *in vivo*, and evidence suggests that the degradation products of implanted scaffold materials may also adversely affect outcomes[114]. In response to this, researchers have thus sought to develop tissue engineering methods that are scaffold-free. One study aimed to develop a cell-sheet technique in which sheets of differentiated hiPSCs would be able to be stably cultured *in vitro* before engraftment in a porcine ischemic cardiomyopathy model without the subsequent loss of transplanted cells[115]. This was achieved by functionalizing culture surfaces with poly(N-isopropylacrylamide) (PNIPAM), a well-known thermoresponsive polymer hydrogel that transitions from a hydrophilic and cell-resistant hydrated gel below 32ºC, to a slightly hydrophobic and cell-adhesive dehydrated form at 37ºC. By culturing cells on PNIPAM-functionalized substrates, entire cell sheets can be dissociated intact from the culture surface without the need for digestive enzymes such as trypsin, which preserves cell-cell junctions and adhesive proteins within the confluent monolayers.

As an alternative approach, it has been suggested that rather than create discrete sheets or pieces of tissues, an entire heart could be grown in the laboratory from the patient's own stem cells and then subsequently implanted, thereby serving as a form of autologous transplantation. Recent developments in tissue decellularization techniques in which the cell removal does not result in ECM degradation have opened the doors for such an approach[116]. As mentioned previously, the ECM plays a significant role in

regulating tissue and organ function through physical and biochemical cues presented. These cues are often difficult to accurately reproduce with conventional synthetically-derived materials, and are spatially specific within even the same organ. Thus, if an entire heart's structure and ECM composition could be preserved and used as a sort of natural scaffold, it stands to reason that introduced immature cells would be able to self-organize and mature to form a new functioning organ. In one study, Ott et al. attempted to generate a whole-heart scaffold that contained the intact 3D geometry and vasculature of the native organ by way of perfusion-based decellularization. Cadaveric rat hearts were serially perfused with SDS and Triton-X100, and it was shown that the remaining matrix was essentially cell-free and detergent-free. Histological analysis revealed that essential ECM proteins (collagen I & III, laminin, fibronectin) and native matrix architecture were well preserved. Mechanical testing revealed that in general the moduli of the decellularized tissues was greater than that of the cadaveric tissues, although the stiffness of the two were similar. To test whether perfusion culture and physiological stimulation, in conjunction with the decellularized matrices, would support tissue formation and maturation, matrices were recellularized with neonatal cardiac cells and cultured in bioreactors for up to 28 days. Functionally, it was found that contractile forces exerted by the bioartificial hearts were only approximately 2% of those exerted by adult rat hearts. Additionally, it was found that at day 8 approximately 35% of the ECM was repopulated by cells, and that the cells were generally viable. The presence of proteins normally expressed by mature cardiomyocytes was observed in the cultures, and it was suggested that the gap junction proteins (particularly Cx43) were functional. If perfected, this technique could drastically change the organ transplantation

landscape, allowing for the growing of organs containing patient-derived cells as needed. However, there appears to be significant variations in functional restoration of the tissues between recellularized hearts, with only two hearts showing significant maximal left ventricular pressure (LVP) and maximal change in pressure over change in time. Contractile forces were also relatively poor compared to adult rat hearts. It was noted that these results may be related to the heterogenous distribution of cells within the ECM, and it was acknowledged that this aspect of recellularization needed to be further optimized.

1.5 Unmet Needs and Future Perspectives

Despite the numerous advances detailed in this review, is still a dire need for an engineered cardiac tissue platform that is capable of completely restoring cardiac function or accurately recapitulating pathological responses to diseases and drugs. In fact, after nearly two decades of progress, engineered tissues have yet to make a significant clinical or commercial impact. Clearly, inducing cells to replicate the appropriate developmental processes seen *in vivo* in an artificial and unfamiliar environment *in vitro* is a non-trivial task, and the ideal combination of conditions that would solve this challenge continues to be elusive. Thus, there is an intense focus on developing bioengineering strategies to improve engineered cardiac tissue development *in vitro*. These techniques seek to mimic multiple aspects of the cardiac microenvironmental niche, using manipulation of scaffold biomaterial composition, small molecule doping, and electromechanical and mechanical stimulation to improve the differentiation, development, and maturation of cultured cardiomyocytes. In time,

improvements in our ability to replicate the intricate cell-cell and cell-matrix interactions that occur within the native myocardium will likely lead to more physiologically-representative models of the human heart for numerous downstream applications.

1.6 Dissertation Specific Aims

The overarching goal of the research presented in this dissertation was to develop composite hydrogel scaffolds that mimic the electrical, mechanical and biochemical environmental cues seen in the healthy human myocardium by combining the unique characteristics of reduced graphene oxide and decellularized myocardial matrices synergistically, and to test this novel biomaterials ability to generate functional cardiac tissues for *in vitro* applications. This was accomplished by pursing the following specific aims:

Aim 1. Develop and characterize a library of myocardial matrix-based hybrid hydrogels with tunable electrical and mechanical properties

It was hypothesized that the integration of reduced graphene oxide (rGO) with decellularized myocardial extracellular matrix (dECM) hydrogels would lead to the development of bioactive 3D scaffolds that would improve the electrical and mechanical function of human stem cell-derived cardiomyocytes. The conductivity and modulus of the scaffolds across a range of both rGO concentration and degree of GO reduction was characterized, and the preservation of the biochemical properties of the dECM component of the scaffold post-decellularization was assessed. Biocompatibility of the hybrid hydrogels with hiPSC-derived cardiomyocytes was also examined.

Aim 2: Assess the effects of electroconductive dECM hydrogels on engineered 3D cardiac tissue maturation and function

To assess hydrogel-mediated effects on cardiomyocyte function, hiPSC-derived cardiomyocytes were seeded, along with HS-27A stromal cells, into hydrogels to form 3D engineered heart tissues (EHTs). Contractile function of the engineered cardiac tissues was assessed over the course of 35 days. Tissues were then be stained for α-actinin to assess scaffold-mediated contractile apparatus and structural development. The expression levels of key genetic markers for cardiac maturation, such as cardiac troponin T and β-MHC, was assessed and quantified with RT-qPCR. Electrophysiological assessment of the effects of biomimetic conductive scaffolds on calcium handling, conduction velocity, and action potential duration was performed using fluorescent imaging of tissues in the presence of calcium- and voltage-sensing dyes.

Aim 3: Validate the use of 3D cardiac tissue models for predictive drug cardiotoxicity screening

It was hypothesized that with the ability to engineer 3D cardiac tissue constructs that better recapitulate the function and phenotype of adult human myocardial tissue, we could improve on existing *in vitro* models for drug screening. A bioprinting strategy for the fabrication of human cardiac tissues in a high-throughput manner that would not only induce physiologically-relevant structural organization, but also allow for end-user flexibility in regards to culture platform. The capability of bioprinted cardiac tissue models to be feasibly employed as a predictive screening platform for drugs with potential arrhythmogenic effects was then assessed.

1.7 References

1 Celermajer, D. S., Chow, C. K., Marijon, E., Anstey, N. M. & Woo, K. S. Cardiovascular disease in the developing world: prevalences, patterns, and the potential of early disease detection. *J. Am. Coll. Cardiol.* **60**, 1207-1216 (2012).

2 Heidenreich, P. A. *et al.* Forecasting the future of cardiovascular disease in the United States: a policy statement from the American Heart Association. *Circulation* **123**, 933-944 (2011).

3 Bergmann, O. *et al.* Evidence for cardiomyocyte renewal in humans. *Science* **324**, 98-102 (2009).

4 Puccio, H. *et al.* Mouse models for Friedreich ataxia exhibit cardiomyopathy, sensory nerve defect and Fe-S enzyme deficiency followed by intramitochondrial iron deposits. *Nat. Genet.* **27**, 181-186 (2001).

5 Geisterfer-Lowrance, A. A. *et al.* A mouse model of familial hypertrophic cardiomyopathy. *Science* **272**, 731-734 (1996).

6 Megeney, L. A. *et al.* Severe cardiomyopathy in mice lacking dystrophin and MyoD. *Proc. Natl. Acad. Sci. U. S. A.* **96**, 220-225 (1999).

7 Arber, S. *et al.* MLP-deficient mice exhibit a disruption of cardiac cytoarchitectural organization, dilated cardiomyopathy, and heart failure. *Cell* **88**, 393-403 (1997).

8 Patten, R. D. & Hall-Porter, M. R. Small animal models of heart failure: development of novel therapies, past and present. *Circ. Heart Fail.* **2**, 138-144 (2009).

9 Perel, P. *et al.* Comparison of treatment effects between animal experiments and clinical trials: systematic review. *BMJ* **334**, 197 (2007).

10 Hasenfuss, G. Animal models of human cardiovascular disease, heart failure and hypertrophy. *Cardiovasc. Res.* **39**, 60-76 (1998).

11 Leung, D. G. *et al.* Sildenafil does not improve cardiomyopathy in Duchenne/Becker muscular dystrophy. *Ann. Neurol.* **76**, 541-549 (2014).

12 Fine, B. & Vunjak-Novakovic, G. Shortcomings of animal models and the rise of engineered human cardiac tissue. *ACS Biomater. Sci. Eng.* **3**, 1884-1897 (2017).

13 Vunjak Novakovic, G., Eschenhagen, T. & Mummery, C. Myocardial tissue engineering: in vitro models. *Cold Spring Harb. Perspect. Med.* **4** (2014).

14 Ferri, N. *et al.* Drug attrition during pre-clinical and clinical development: Understanding and managing drug-induced cardiotoxicity. *Pharmacol. Ther.* **138**, 470-484 (2013).

15 Redfern, W. S. *et al.* Relationships between preclinical cardiac electrophysiology, clinical QT interval prolongation and torsade de pointes for a broad range of drugs: evidence for a provisional safety margin in drug development. *Cardiovasc. Res.* **58**, 32-45 (2003).

16 Stevens, J. L. & Baker, T. K. The future of drug safety testing: expanding the view and narrowing the focus. *Drug Discov. Today* **14**, 162-167 (2009).

17 Hansen, A. *et al.* Development of a drug screening platform based on engineered heart tissue. *Circ. Res.* **107**, 35-44 (2010).

18 Boudou, T. *et al.* A microfabricated platform to measure and manipulate the mechanics of engineered cardiac microtissues. *Tissue Eng. Part A* **18**, 910-919 (2012).

19 Mathur, A. *et al.* Human iPSC-based cardiac microphysiological system for drug screening applications. *Sci. Rep.* **5**, 8883 (2015).
20 Friedrich, F. W. *et al.* Evidence for FHL1 as a novel disease gene for isolated hypertrophic cardiomyopathy. *Hum. Mol. Genet.* **21**, 3237-3254 (2012).
21 Hirt, M. N. *et al.* Increased afterload induces pathological cardiac hypertrophy: a new in vitro model. *Basic Res. Cardiol.* **107**, 307 (2012).
22 Thavandiran, N. *et al.* Design and formulation of functional pluripotent stem cell-derived cardiac microtissues. *Proc. Natl. Acad. Sci. U. S. A.* **110**, E4698-4707 (2013).
23 Ma, Z. *et al.* Three-dimensional filamentous human diseased cardiac tissue model. *Biomaterials* **35**, 1367-1377 (2014).
24 Leor, J. *et al.* Bioengineered cardiac grafts: A new approach to repair the infarcted myocardium? *Circulation* **102**, III56-61 (2000).
25 Zimmermann, W. H. *et al.* Cardiac grafting of engineered heart tissue in syngenic rats. *Circulation* **106**, I151-157 (2002).
26 Zimmermann, W. H. *et al.* Engineered heart tissue grafts improve systolic and diastolic function in infarcted rat hearts. *Nat. Med.* **12**, 452-458 (2006).
27 Kofidis, T. *et al.* Myocardial restoration with embryonic stem cell bioartificial tissue transplantation. *J. Heart Lung Transplant.* **24**, 737-744 (2005).
28 Zong, X. *et al.* Electrospun fine-textured scaffolds for heart tissue constructs. *Biomaterials* **26**, 5330-5338 (2005).
29 Radisic, M. *et al.* Biomimetic approach to cardiac tissue engineering. *Philos. Trans. R. Soc. Lond. B. Biol. Sci.* **362**, 1357-1368 (2007).
30 Brown, M. A., Iyer, R. K. & Radisic, M. Pulsatile perfusion bioreactor for cardiac tissue engineering. *Biotechnol. Prog.* **24**, 907-920 (2008).
31 Tulloch, N. L. *et al.* Growth of engineered human myocardium with mechanical loading and vascular coculture. *Circ. Res.* **109**, 47-59 (2011).
32 Ronaldson-Bouchard, K. *et al.* Advanced maturation of human cardiac tissue grown from pluripotent stem cells. *Nature* **556**, 239-243 (2018).
33 Stadtfeld, M. & Hochedlinger, K. Induced pluripotency: history, mechanisms, and applications. *Genes Dev.* **24**, 2239-2263 (2010).
34 Takahashi, K. *et al.* Induction of pluripotent stem cells from adult human fibroblasts by defined factors. *Cell* **131**, 861-872 (2007).
35 Anokye-Danso, F. *et al.* Highly efficient miRNA-mediated reprogramming of mouse and human somatic cells to pluripotency. *Cell Stem Cell* **8**, 376-388 (2011).
36 Del Alamo, J. C. *et al.* High throughput physiological screening of iPSC-derived cardiomyocytes for drug development. *Biochim. Biophys. Acta* **1863**, 1717-1727 (2016).
37 Gilchrist, K. H., Lewis, G. F., Gay, E. A., Sellgren, K. L. & Grego, S. High-throughput cardiac safety evaluation and multi-parameter arrhythmia profiling of cardiomyocytes using microelectrode arrays. *Toxicol. Appl. Pharmacol.* **288**, 249-257 (2015).
38 Guo, L. *et al.* Refining the human iPSC-cardiomyocyte arrhythmic risk assessment model. *Toxicol. Sci.* **136**, 581-594 (2013).

39 Smith, A. S. T., Macadangdang, J., Leung, W., Laflamme, M. A. & Kim, D. H. Human iPSC-derived cardiomyocytes and tissue engineering strategies for disease modeling and drug screening. *Biotechnol. Adv.* **35**, 77-94 (2017).
40 Ma, D. *et al.* Characterization of a novel KCNQ1 mutation for type 1 long QT syndrome and assessment of the therapeutic potential of a novel IKs activator using patient-specific induced pluripotent stem cell-derived cardiomyocytes. *Stem Cell Res. Ther.* **6**, 39 (2015).
41 Mehta, A. *et al.* Re-trafficking of hERG reverses long QT syndrome 2 phenotype in human iPS-derived cardiomyocytes. *Cardiovasc. Res.* **102**, 497-506 (2014).
42 Itzhaki, I. *et al.* Modelling the long QT syndrome with induced pluripotent stem cells. *Nature* **471**, 225-229 (2011).
43 Moretti, A. *et al.* Patient-specific induced pluripotent stem-cell models for long-QT syndrome. *N. Engl. J. Med.* **363**, 1397-1409 (2010).
44 Sun, N. *et al.* Patient-specific induced pluripotent stem cells as a model for familial dilated cardiomyopathy. *Sci. Transl. Med.* **4**, 130ra147 (2012).
45 Han, L. *et al.* Study familial hypertrophic cardiomyopathy using patient-specific induced pluripotent stem cells. *Cardiovasc. Res.* **104**, 258-269 (2014).
46 Yang, X., Pabon, L. & Murry, C. E. Engineering adolescence: maturation of human pluripotent stem cell-derived cardiomyocytes. *Circ. Res.* **114**, 511-523 (2014).
47 Knollmann, B. C. Induced pluripotent stem cell-derived cardiomyocytes: boutique science or valuable arrhythmia model? *Circ. Res.* **112**, 969-976; discussion 976 (2013).
48 Keung, W., Boheler, K. R. & Li, R. A. Developmental cues for the maturation of metabolic, electrophysiological and calcium handling properties of human pluripotent stem cell-derived cardiomyocytes. *Stem Cell Res. Ther.* **5**, 17 (2014).
49 Bissell, M. J., Hall, H. G. & Parry, G. How does the extracellular-matrix direct gene-expression. *J. Theor. Biol.* **99**, 31-68 (1982).
50 Eschenhagen, T. *et al.* Three-dimensional reconstitution of embryonic cardiomyocytes in a collagen matrix: a new heart muscle model system. *FASEB J.* **11**, 683-694 (1997).
51 Zimmermann, W. H. *et al.* Three-dimensional engineered heart tissue from neonatal rat cardiac myocytes. *Biotechnol. Bioeng.* **68**, 106-114 (2000).
52 Nunes, S. S. *et al.* Biowire: a platform for maturation of human pluripotent stem cell-derived cardiomyocytes. *Nat. Methods* **10**, 781-787 (2013).
53 Lee, C. H., Singla, A. & Lee, Y. Biomedical applications of collagen. *Int. J. Pharm.* **221**, 1-22 (2001).
54 Mizuno, S. & Glowacki, J. Three-dimensional composite of demineralized bone powder and collagen for in vitro analysis of chondroinduction of human dermal fibroblasts. *Biomaterials* **17**, 1819-1825 (1996).
55 Zhang, D. *et al.* Tissue-engineered cardiac patch for advanced functional maturation of human ESC-derived cardiomyocytes. *Biomaterials* **34**, 5813-5820 (2013).
56 Leonard, A. *et al.* Afterload promotes maturation of human induced pluripotent stem cell derived cardiomyocytes in engineered heart tissues. *J. Mol. Cell. Cardiol.* **118**, 147-158 (2018).

57 Boudou, T. *et al.* A microfabricated platform to measure and manipulate the mechanics of engineered cardiac microtissues. *Tissue Eng. Part A* **18**, 910-919 (2012).
58 Ahmed, T. A., Dare, E. V. & Hincke, M. Fibrin: a versatile scaffold for tissue engineering applications. *Tissue Eng. Part B Rev.* **14**, 199-215 (2008).
59 Schense, J. C. & Hubbell, J. A. Cross-linking exogenous bifunctional peptides into fibrin gels with factor XIIIa. *Bioconjug. Chem.* **10**, 75-81 (1999).
60 Birgersdotter, A., Sandberg, R. & Ernberg, I. Gene expression perturbation in vitro--a growing case for three-dimensional (3D) culture systems. *Semin. Cancer Biol.* **15**, 405-412 (2005).
61 Tiburcy, M. *et al.* Defined engineered human myocardium with advanced maturation for applications in heart failure modeling and repair. *Circulation* **135**, 1832-1847 (2017).
62 Singelyn, J. M. *et al.* Naturally derived myocardial matrix as an injectable scaffold for cardiac tissue engineering. *Biomaterials* **30**, 5409-5416 (2009).
63 Pati, F. *et al.* Printing three-dimensional tissue analogues with decellularized extracellular matrix bioink. *Nat. Commun.* **5** (2014).
64 Eitan, Y., Sarig, U., Dahan, N. & Machluf, M. Acellular cardiac extracellular matrix as a scaffold for tissue engineering: in vitro cell support, remodeling, and biocompatibility. *Tissue Eng. Part C Methods* **16**, 671-683 (2010).
65 Gaetani, R. *et al.* Cardiac tissue engineering using tissue printing technology and human cardiac progenitor cells. *Biomaterials* **33**, 1782-1790 (2012).
66 Rowley, J. A., Madlambayan, G. & Mooney, D. J. Alginate hydrogels as synthetic extracellular matrix materials. *Biomaterials* **20**, 45-53 (1999).
67 Shachar, M., Tsur-Gang, O., Dvir, T., Leor, J. & Cohen, S. The effect of immobilized RGD peptide in alginate scaffolds on cardiac tissue engineering. *Acta Biomater.* **7**, 152-162 (2011).
68 Nichol, J. W. *et al.* Cell-laden microengineered gelatin methacrylate hydrogels. *Biomaterials* **31**, 5536-5544 (2010).
69 Loessner, D. *et al.* Functionalization, preparation and use of cell-laden gelatin methacryloyl–based hydrogels as modular tissue culture platforms. *Nat. Protoc.* **11**, 727 (2016).
70 Duan, B., Kapetanovic, E., Hockaday, L. A. & Butcher, J. T. Three-dimensional printed trileaflet valve conduits using biological hydrogels and human valve interstitial cells. *Acta Biomater.* **10**, 1836-1846 (2014).
71 Annabi, N. *et al.* Highly elastic micropatterned hydrogel for engineering functional cardiac tissue. *Adv. Funct. Mater.* **23** (2013).
72 Rodriguez, A. G., Han, S. J., Regnier, M. & Sniadecki, N. J. Substrate stiffness increases twitch power of neonatal cardiomyocytes in correlation with changes in myofibril structure and intracellular calcium. *Biophys. J.* **101**, 2455-2464 (2011).
73 Bhana, B. *et al.* Influence of substrate stiffness on the phenotype of heart cells. *Biotechnol. Bioeng.* **105**, 1148-1160 (2010).
74 Engler, A. J. *et al.* Embryonic cardiomyocytes beat best on a matrix with heart-like elasticity: scar-like rigidity inhibits beating. *J. Cell Sci.* **121**, 3794-3802 (2008).

75 Chun, Y. W. *et al.* Combinatorial polymer matrices enhance in vitro maturation of human induced pluripotent stem cell-derived cardiomyocytes. *Biomaterials* **67**, 52-64 (2015).
76 Kim, T. G. & Park, T. G. Biomimicking extracellular matrix: cell adhesive RGD peptide modified electrospun poly(D,L-lactic-co-glycolic acid) nanofiber mesh. *Tissue Eng.* **12**, 221-233 (2006).
77 Iyer, R. K. & Radisic, M. A138. Microfabricated poly(ethylene glycol) templates for cell tri-culture in cardiac tissue engineering. *J. Mol. Cell. Cardiol.* **40**, 877 (2006).
78 Kim, D. H. *et al.* Nanoscale cues regulate the structure and function of macroscopic cardiac tissue constructs. *Proc. Natl. Acad. Sci. U. S. A.* **107**, 565-570 (2010).
79 Carson, D. *et al.* Nanotopography-induced structural anisotropy and sarcomere development in human cardiomyocytes derived from induced pluripotent stem cells. *ACS Appl. Mater. Interfaces* **8**, 21923-21932 (2016).
80 Miller, J. S. *et al.* Bioactive hydrogels made from step-growth derived PEG–peptide macromers. *Biomaterials* **31**, 3736-3743 (2010).
81 Fairbanks, B. D., Schwartz, M. P., Bowman, C. N. & Anseth, K. S. Photoinitiated polymerization of PEG-diacrylate with lithium phenyl-2,4,6-trimethylbenzoylphosphinate: polymerization rate and cytocompatibility. *Biomaterials* **30**, 6702-6707 (2009).
82 DeForest, C. A., Polizzotti, B. D. & Anseth, K. S. Sequential click reactions for synthesizing and patterning three-dimensional cell microenvironments. *Nat. Mater.* **8**, 659 (2009).
83 Pratt, A. B., Weber, F. E., Schmoekel, H. G., Muller, R. & Hubbell, J. A. Synthetic extracellular matrices for in situ tissue engineering. *Biotechnol. Bioeng.* **86**, 27-36 (2004).
84 West, J. L. & Hubbell, J. A. Polymeric biomaterials with degradation sites for proteases involved in cell migration. *Macromolecules* **32**, 241-244 (1999).
85 Ku, S. H., Lee, M. & Park, C. B. Carbon-based nanomaterials for tissue engineering. *Adv. Healthc. Mater.* **2**, 244-260 (2013).
86 Agarwal, S. *et al.* Interfacing live cells with nanocarbon substrates. *Langmuir* **26**, 2244-2247 (2010).
87 Kalbacova, M., Broz, A., Kong, J. & Kalbac, M. Graphene substrates promote adherence of human osteoblasts and mesenchymal stromal cells. *Carbon* **48**, 4323-4329 (2010).
88 Kalbacova, M., Broz, A. & Kalbac, M. Influence of the fetal bovine serum proteins on the growth of human osteoblast cells on graphene. *J. Biomed. Mater. Res. A* **100A**, 3001-3007 (2012).
89 Chen, G. Y., Pang, D. W., Hwang, S. M., Tuan, H. Y. & Hu, Y. C. A graphene-based platform for induced pluripotent stem cells culture and differentiation. *Biomaterials* **33**, 418-427 (2012).
90 Lee, T. J. *et al.* Graphene enhances the cardiomyogenic differentiation of human embryonic stem cells. *Biochem. Biophys. Res. Commun.* **452**, 174-180 (2014).
91 Navaei, A. *et al.* PNIPAAm-based biohybrid injectable hydrogel for cardiac tissue engineering. *Acta Biomater.* **32**, 10-23 (2016).

92 Hutson, C. B. *et al.* Synthesis and characterization of tunable poly(ethylene glycol): gelatin methacrylate composite hydrogels. *Tissue Eng. Part A* **17**, 1713-1723 (2011).
93 Park, H., Radisic, M., Lim, J. O., Chang, B. H. & Vunjak-Novakovic, G. A novel composite scaffold for cardiac tissue engineering. *In Vitro Cell. Dev. Biol. Anim.* **41**, 188-196 (2005).
94 Paul, A. *et al.* Injectable graphene oxide/hydrogel-based angiogenic gene delivery system for vasculogenesis and cardiac repair. *ACS Nano* **8**, 8050-8062 (2014).
95 Shin, S. R. *et al.* Cell-laden microengineered and mechanically tunable hybrid hydrogels of gelatin and graphene oxide. *Adv. Mater.* **25**, 6385-6391 (2013).
96 Fan, H. *et al.* Fabrication, mechanical properties, and biocompatibility of graphene-reinforced chitosan composites. *Biomacromolecules* **11**, 2345-2351 (2010).
97 Shin, S. R. *et al.* Carbon-nanotube-embedded hydrogel sheets for engineering cardiac constructs and bioactuators. *ACS Nano* **7**, 2369-2380 (2013).
98 You, J. O., Rafat, M., Ye, G. J. C. & Auguste, D. T. Nanoengineering the heart: conductive scaffolds enhance connexin 43 expression. *Nano Lett.* **11**, 3643-3648 (2011).
99 Smith, A. S. T. *et al.* Micro- and nano-patterned conductive graphene-PEG hybrid scaffolds for cardiac tissue engineering. *Chem. Commun.* **53**, 7412-7415 (2017).
100 Zhao, X. *et al.* Active scaffolds for on-demand drug and cell delivery. *Proc. Natl. Acad. Sci. U. S. A.* **108**, 67-72 (2011).
101 Leach, J. B., Bivens, K. A., Collins, C. N. & Schmidt, C. E. Development of photocrosslinkable hyaluronic acid-polyethylene glycol-peptide composite hydrogels for soft tissue engineering. *J. Biomed. Mater. Res. A* **70**, 74-82 (2004).
102 Tsui, J. H. *et al.* Conductive silk–polypyrrole composite scaffolds with bioinspired nanotopographic cues for cardiac tissue engineering. *J. Mater. Chem. B* **6**, 7185-7196 (2018).
103 Liu, L. *et al.* Cyclic stiffness modulation of cell-laden protein–polymer hydrogels in response to user-specified stimuli including light. *Adv. Biosyst.* **2**, 1800240 (2018).
104 Wylie, R. G. & Shoichet, M. S. Three-dimensional spatial patterning of proteins in hydrogels. *Biomacromolecules* **12**, 3789-3796 (2011).
105 Ruskowitz, E. R., Comerford, M. P., Badeau, B. A. & DeForest, C. A. Logical stimuli-triggered delivery of small molecules from hydrogel biomaterials. *Biomater. Sci.* **7**, 542-546 (2019).
106 Bielawski, K. S., Leonard, A., Bhandari, S., Murry, C. E. & Sniadecki, N. J. Real-time force and frequency analysis of engineered human heart tissue derived from induced pluripotent stem cells using magnetic sensing. *Tissue Eng. Part C Methods* **22**, 932-940 (2016).
107 Skardal, A. *et al.* A hydrogel bioink toolkit for mimicking native tissue biochemical and mechanical properties in bioprinted tissue constructs. *Acta Biomater.* **25**, 24-34 (2015).
108 Choi, Y. J. *et al.* 3D cell printing of functional skeletal muscle constructs using skeletal muscle-derived bioink. *Adv. Healthc. Mater.* **5**, 2636-2645 (2016).

109 Kang, H. W. *et al.* A 3D bioprinting system to produce human-scale tissue constructs with structural integrity. *Nat. Biotechnol.* **34**, 312-319 (2016).
110 Hinton, T. J. *et al.* Three-dimensional printing of complex biological structures by freeform reversible embedding of suspended hydrogels. *Sci. Adv.* **1**, e1500758 (2015).
111 Kolesky, D. B., Homan, K. A., Skylar-Scott, M. A. & Lewis, J. A. Three-dimensional bioprinting of thick vascularized tissues. *Proc. Natl. Acad. Sci. U. S. A.* **113**, 3179-3184 (2016).
112 Grigoryan, B. *et al.* Multivascular networks and functional intravascular topologies within biocompatible hydrogels. *Science* **364**, 458-464 (2019).
113 Lind, J. U. *et al.* Instrumented cardiac microphysiological devices via multimaterial three-dimensional printing. *Nat. Mater.* **16**, 303-308 (2017).
114 Taylor, M. S., Daniels, A. U., Andriano, K. P. & Heller, J. Six bioabsorbable polymers: in vitro acute toxicity of accumulated degradation products. *J. Appl. Biomater.* **5**, 151-157 (1994).
115 Kawamura, M. *et al.* Feasibility, safety, and therapeutic efficacy of human induced pluripotent stem cell-derived cardiomyocyte sheets in a porcine ischemic cardiomyopathy model. *Circulation* **126**, S29-37 (2012).
116 Ott, H. C. *et al.* Perfusion-decellularized matrix: using nature's platform to engineer a bioartificial heart. *Nat. Med.* **14**, 213-221 (2008).

Chapter 2. Decellularized Extracellular Matrix - Reduced Graphene Oxide Hybrid Hydrogels with Tunable Electrical and Mechanical Properties

2.1 Abstract

A major hurdle in the field of tissue engineering is the difficulty in recapitulating the full spectrum of native tissue microenvironmental cues that direct cellular function and development. This is largely due to the limitations of the biomaterials that are utilized to serve as scaffolds. Naturally-derived materials, while generally more biocompatible and bioactive, often suffer from a modulus mismatch with the tissues that are to be modeled. Synthetic materials, on the other hand, although more readily synthesized and have properties that can be tailored for specific applications, do not inherently possess biochemical cues capable of supporting cellular development. In this work, a multiscale hybrid hydrogel was developed that is comprised of reduced graphene oxide (rGO) that is homogenously dispersed in decellularized extracellular matrix (dECM) derived from porcine left ventricular myocardium. The mechanical and electrical properties of the resulting hydrogel was characterized using compressive, rheological, and four-point probe testing. By modulating the rGO content and the degree of reduction of the incorporated rGO, these properties could be readily tuned to achieve the desired values to suit the application.

2.2 Introduction

In vivo, cardiomyocytes are surrounded in three dimensions by a extracellular matrix (ECM) that defines the architecture, signaling, and biomechanics of the cellular microenvironment[1,2]. This regulation of cell behavior by the ECM is known to be due to a precise combination of biochemical, mechanical, structural, and electrical cues. Advances in three-dimensional (3D) tissue engineering approaches have been able to better recapitulate this cell niche; however, overall cardiomyocyte and engineered cardiac tissue maturity is still at suboptimal levels due to limitations with the scaffolds and platforms that are currently available. Naturally-derived polymers typically used to engineer 3D tissues such as fibrin and collagen offer good biocompatibility and biochemical similarity to *in vivo* systems. In particular, decellularized extracellular matrices (dECM) are able to largely preserve the tissue-specific biochemical makeup of the tissues that they are derived from[3]. The poor mechanical and electrical properties of these polymers, however, often hampers their ability to replicate the tissue microenvironment. Synthetic materials on the other hand, offer better control over their physical and chemical characteristics, but their bioactivity is often non-existent without further modification. Perhaps the most interesting exception to this though are highly electroconductive materials, such as carbon nanotubes[4,5], graphene derivatives[6,7], and gold[8,9], that have been found to impart beneficial effects on the growth and maturation of a variety of cell types and have recently gained increasing prominence in the field of tissue engineering.

Here, we report on the development of hybrid hydrogels that are comprised of reduced graphene oxide (rGO) dispersed within decellularized myocardial extracellular

matrices (dECM). By leveraging the advantages offered by rGO with regards to controlling properties such as stiffness and electroconductivity while maintaining the bioactivity inherent with dECM, this new material can advance the capability to engineer 3D human cardiac tissues that are more physiologically-representative of the native myocardium.

2.3 Materials and Methods

2.3.1 Left Ventricular Myocardium Decellularization

Myocardial decellularized extracellular matrix (dECM) was obtained by an adaptation of well-established methods detailed in the literature[10,11]. In brief, left ventricular myocardium was isolated from fresh porcine hearts and sectioned into small slices approximately 1 mm in thickness. Slices underwent cell lysis and removal in a solution of 1% w/v sodium dodecyl sulfate (SDS; Fisher Scientific) for 36 h, with an additional wash in 1% w/v Triton-X100 (Sigma-Aldrich) for 1 hour to complete cellular material removal. This was followed by washes in phosphate buffered saline (PBS) over 3 days, with the wash solution changed every day to remove excess detergent and cell debris. dECM was sterilized with 0.1% w/v peracetic acid in 4% w/v ethanol, followed by an additional wash in PBS overnight. Afterwards, the dECM was lyophilized and stored at 4°C until used.

2.3.2 Assessment of dECM Biochemical Composition

Dry weights of lyophilized dECM were determined and the samples were digested at a concentration of 5 mg/mL in a solution containing 5 M urea, 2 M thiourea, 50 mM DTT and 0.1% SDS in PBS with constant stirring at 4°C for 48 h. Afterwards, the samples were sonicated on ice (Branson Digital Sonifier, 20 s pulses, 30% amplitude), and protein was precipitated with acetone and analyzed *via* liquid chromatography tandem mass spectrometry (LC-MS/MS). The 15 most abundant ECM components for each developmental age were identified from spectrum count data.

2.3.3 Graphene Oxide Reduction and Reaction Validation

Reduced graphene oxide (rGO) was chemically reduced from commercially-available graphene oxide solution (GO; Graphene Laboratories) using $NaBH_4$ (Sigma-Aldrich), as previously described[12]. Briefly, GO flakes with a lateral flake size of 90 nm – 200 nm in a 1 mg/mL stock solution were mixed with varying concentrations of $NaBH_4$ (50 mM – 300 mM) for 1 hour at room temperature. The resulting rGO was then vacuum filtered through mixed cellulose ester membranes (MilliporeSigma) with a 0.1 µm pore size. Filtered rGO was then removed and resuspended in dH_2O at 10 mg/mL using a sonication bath. Prior to resuspension of filtered rGO, samples were collected for reduction process validation and analysis with a confocal Raman microscope (Renishaw InVia). The relative intensity of the D (1350 cm^{-1}) and G (1600 cm^{-1}) peaks were then measured from the collected spectra of each sample.

2.3.4 Extracellular Matrix Solubilization and Hydrogel Formation

dECM-based pre-hydrogel solutions were generated by mixing lyophilized dECM and pepsin at a 10:1 mass ratio in 0.1 M HCl. rGO was also added at this stage for dECM-rGO hydrogels. A 2% w/v dECM solution was used for all experiments in this study while the final concentration of the rGO component was varied from 0.1% - 0.3% w/v. Mixtures were stirred constantly until the dECM was completely solubilized and had formed a homogenous solution, at which point the pH was then brought up to 7.4 with 10 M NaOH. Finally, 10% of the final volume of 10X PBS or 10X RPMI 1640 (Sigma-Aldrich) was added to restore isotonic balance. Hydrogel pre-gel solutions were stored at 4ºC until use. Hydrogels were then formed by incubating pre-gel solutions at 37ºC for at least 12 h. The same solubilization and gelation method was used to generate control hydrogels composed of bovine collagen type I (Advanced BioMatrix). For generating dECM-TG hydrogels for stiffness controls, a 5% w/v solution of transglutaminase (TG; Modernist Pantry) was added to the dECM solution immediately prior to incubation at 37ºC.

2.3.5 Microstructural Imaging with Scanning Electron Microscopy

dECM-rGO hydrogels and decellularized myocardial sheets underwent critical-point drying. Samples were then sputter-coated with a thin layer of Au/Pd alloy before imaging in a FEI Sirion XL30 scanning electron microscope at a 5 kV accelerating voltage.

2.3.6 Characterization of Hydrogel Mechanical and Electrical Properties

Hydrogel conductivity was quantified using a four-point probe (Four Dimensions Model 280SI). Thin films were deposited onto a glass coverslip and probe measurements were taken at 20 different points across the sample and averaged. Compressive moduli of crosslinked hydrogels were measured using an Instron compressive testing system, with the composite hydrogel samples compressed at a rate of 10 mm/min until failure. Rheological measurements were taken with a rheometer (TA Instruments Discovery HR-2,) using two different protocols. Viscosity values were obtained by conducting a shear rate sweep of 0.1 – 100, with pre-gel solution held at 25ºC. G' and G" values were obtained by conducting a frequency sweep of 0.1 – 100 rad/s at 1% strain, with crosslinked hydrogels held at 25ºC. For both protocols, tested samples first underwent a 10 s pre-shear at 0.1 rad/s.

2.3.7 Statistical Analyses

Unless otherwise noted, all quantitative data is presented as means ± standard error. One-way ANOVA with a Tukey's *post-hoc* test was used to analyze data sets that included more than two experimental groups, while a Student's *t*-test was used to compare data sets looking at only two variables. In all presented analyses, $p < 0.05$ was considered significant.

2.4 Results

2.4.1 Hybrid Hydrogel Synthesis and Component Validation

The two primary components of the dECM-rGO composite hydrogels used in this study were prepared *via* parallel processes (**Figure 2.1a**). Left ventricular myocardium from freshly-harvested porcine hearts were decellularized using an established method that has been previously demonstrated to produce dECM in which the majority of cellular components have been removed, while still preserving the collagens and glycosaminoglycans (GAGs) originally present in the tissue[10]. As one of the stated benefits of utilizing dECM as a scaffold material is its recapitulation of the native tissue microenvironment, further analysis of its biochemical makeup post-decellularization was conducted using liquid chromatography tandem mass spectrometry (LC-MS/MS). Several produced batches of dECM were analyzed for key matrix proteins: collagens I – IV, fibronectin, and laminin (**Figure 2.1b**). It was found that while batch-to-batch variation in the quantities of these proteins did exist, the overall content and relative ratios were well maintained (**Figure 2.1c**), with collagen I the most abundant protein type found in the myocardial dECM. The next most abundant proteins found were collagen III, fibronectin, and laminin. This ECM protein composition is similar those that found in adult rat hearts[13], indicating that the dECM produced does indeed maintain developmental stage-appropriate tissue-specificity in regards to biochemical signaling.

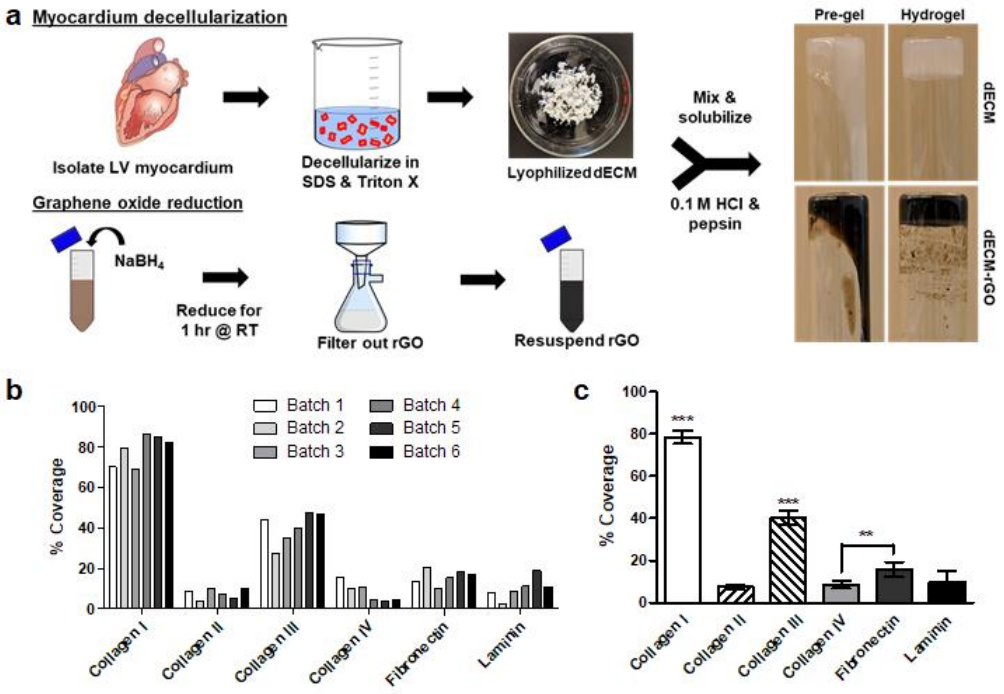

Figure 2.1. Materials synthesis and biochemical characterization. (a) Composite hydrogels are synthesized using a parallel process. dECM (top) is produced by first isolating and mincing left ventricular myocardium from freshly-harvested porcine hearts. Minced tissue is decellularized using a combination of detergents before being lyophilized. rGO (bottom) is produced by reducing GO with $NaBH_4$ for 1 hr before filtration and resuspension in dH_2O. The two components are combined with HCl and pepsin to form a pre-gel solution that can then be formed into hydrogels by incubation at 37ºC. (b) LC/MS analysis of dECM indicates that while some batch-to-batch variation occurs, (c) the overall protein composition is relatively well maintained across produced batches. **p < 0.01, ***p < 0.001 (One-way ANOVA with a Tukey's *post-hoc* test, n = 6).

Reduction of the graphene oxide (GO) was accomplished using a sodium borohydride ($NaBH_4$)-mediated chemical reduction process in which $NaBH_4$ removes oxygen groups from the GO lattice structure in a similar manner to hydrazine (N_2H_4), but without the use of a highly-toxic compound[12]. By adjusting the concentration of $NaBH_4$ used in the reduction process, the degree of reduction of GO to rGO could be varied, and this was confirmed with the use of Raman spectroscopy (**Figure 2.2**). As $NaBH_4$ concentration increased, the D:G peak intensity ratio increased, indicating a removal of lattice defects and a shift towards the restoration of a near-pristine graphene lattice structure.

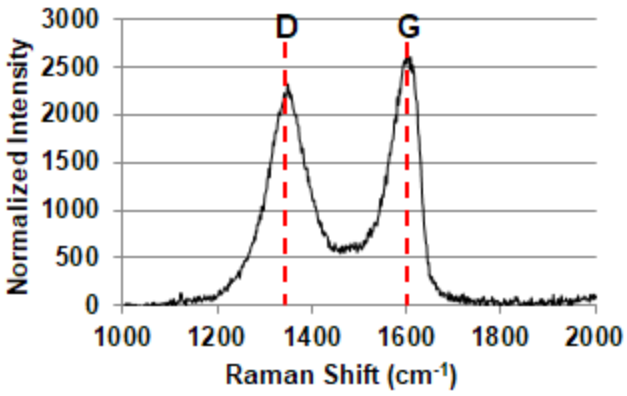

[$NaBH_4$] (mM)	I_D/I_G
0 (neat GO)	0.729 ± 0.031
50	0.817 ± 0.027
100	0.888 ± 0.019
150	0.867± 0.056
200	0.972 ± 0.035
250	1.082 ± 0.042
300	1.232 ± 0.061

Figure 2.2. Validation of graphene oxide reduction process. Representative Raman spectra of GO illustrating the presence of the D and G peaks. Increasing the degree of reduction *via* $NaBH_4$ concentration leads to a corresponding increase in D peak intensity (I_D) relative to G peak intensity (I_G).

2.4.2 Macroscopic Structural Characterization of dECM-rGO Hydrogels

Examination of the macroscopic structure of composite dECM-rGO hydrogels with scanning electron microscopy (SEM) showed that the hydrogels possessed a porous network strikingly similar to that of native porcine myocardium (**Figure 2.3**). Closer examination of dECM-rGO pore walls revealed that nanoscale flakes of rGO were deposited on the walls, indicating that encapsulated cells would be able to closely interact with the rGO. It is unclear, however, whether or not these rGO aggregates penetrated through the walls such that adjacent pores would be connected or bridged by the electroconductive material.

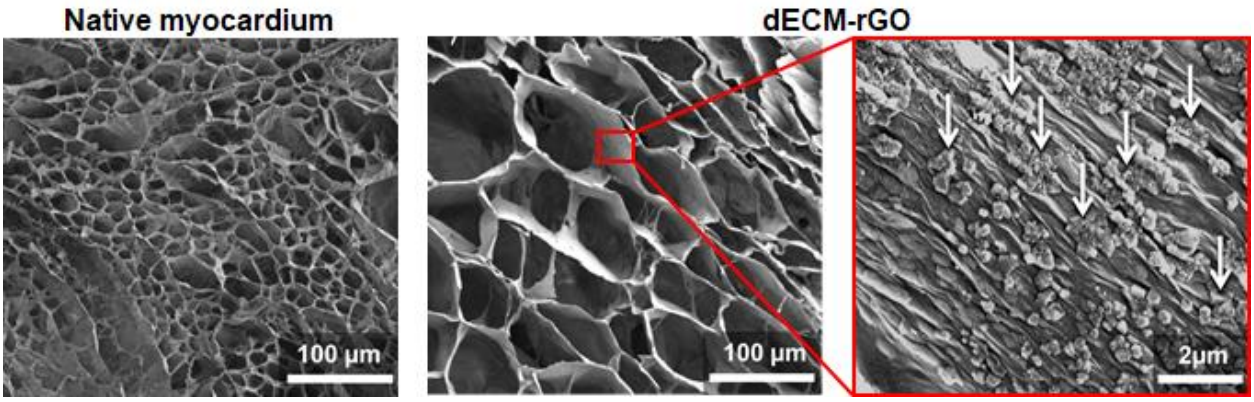

Figure 2.3. Macroscopic structure of dECM-rGO hydrogels. SEM imaging of dECM-rGO hydrogels reveals a porous structure similar to that of decellularized myocardium. Deposition of rGO flakes (white arrows) on the pore walls can be observed.

2.4.3 Characterization of the Mechanical Properties of dECM-rGO Hydrogels

The mechanical properties of dECM-rGO hydrogels were examined using compressive and rheological testing. Compressive modulus was found to increase as both a function of the degree of reduction of the rGO (**Figure 2.4a**) and as a function of rGO content within the hydrogels (**Figure 2.4b**), and the average moduli obtained with the hydrogels tested in this study ranged from 10.6 ± 0.3 kPa (dECM only) to 17.5 ± 0.5 kPa (dECM with 0.3% w/v 300 mM $NaBH_4$ rGO), which are comparable to that of native myocardium[14,15]. Hydrogel viscosity was also found to increase as rGO reduction (**Figure 2.4c**) and content increased (**Figure 2.4d**). Notably, all dECM-based hydrogel formulations exhibited shear-thinning properties, in which material viscosity decreased as shear rate increased.

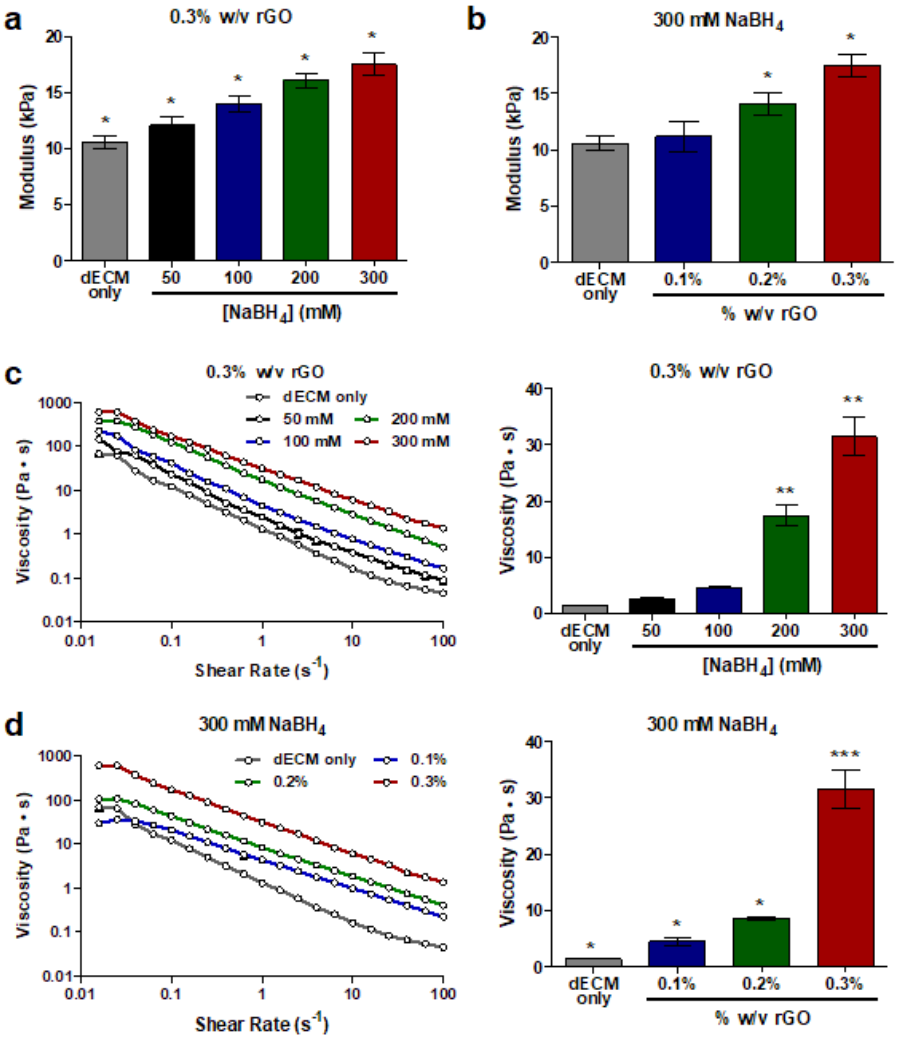

Figure 2.4. Compressive modulus and shear rate-dependent viscosity is tunable. Compressive modulus of composite hydrogels increases as a function of both (a) the degree of reduction of rGO, and (b) the rGO content within the composite hydrogels when degree of reduction is held constant. (c, d) Similar trends can be observed in the viscosity of dECM-rGO pre-gel solutions, and these solutions also exhibit shear-thinning properties. *$p < 0.05$, **$p < 0.01$, ***$p < 0.001$ (One-way ANOVA with a Tukey's post-hoc test, n = 6).

Storage (G') and loss (G") moduli were found to change in response to hydrogel composition in the same manner as before, with G' and G" values increasing as rGO reduction and content increased (**Figure 2.5**).

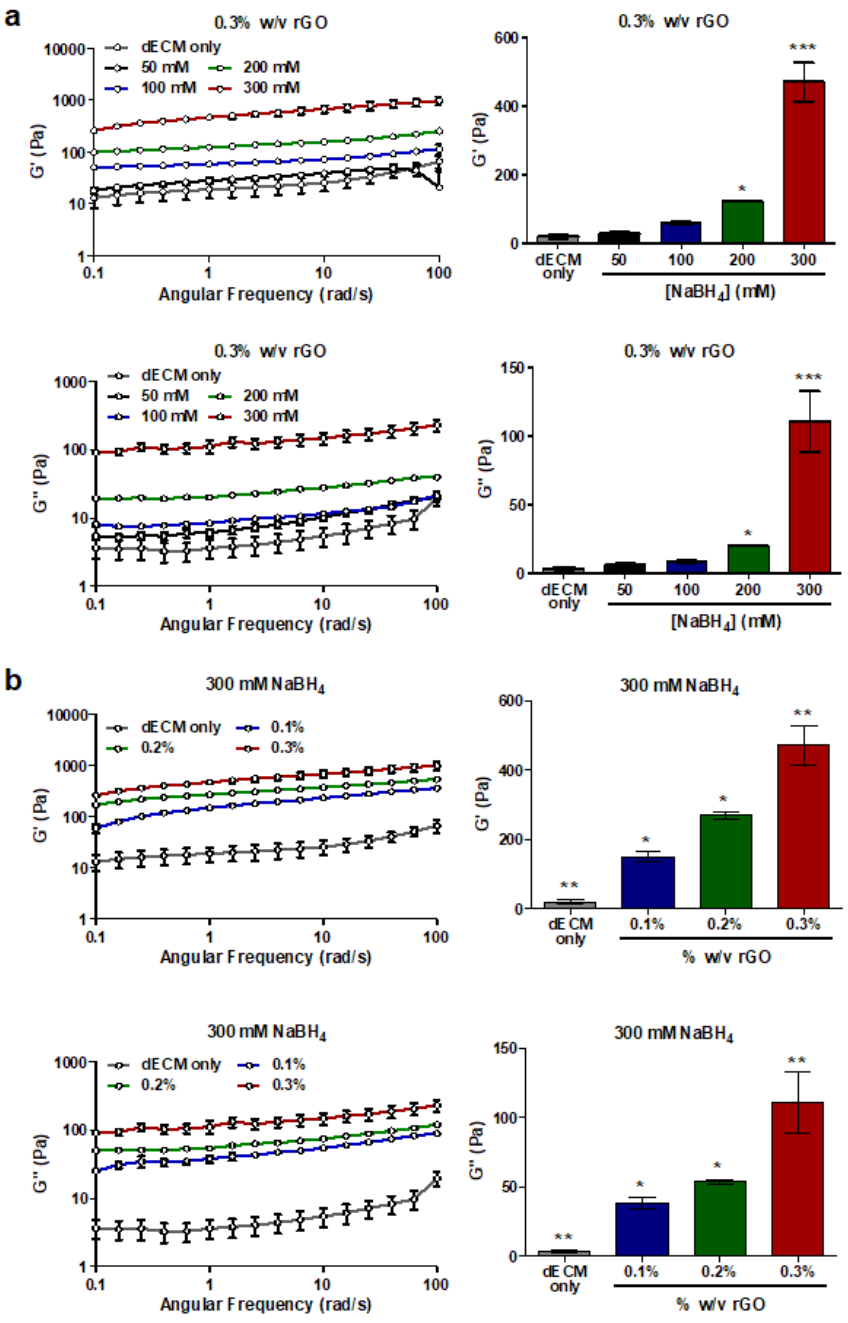

Figure 2.5. Tunable storage and loss modulus of dECM-rGO hydrogels. The storage (G') and loss (G") moduli of dECM-rGO hydrogels increase with corresponding increases in (a) degree of rGO reduction and (b) overall concentration of rGO present in the dECM matrix. *p < 0.05, **p < 0.01, ***p < 0.001 (One-way ANOVA with a Tukey's post-hoc test, n = 6).

2.4.4 Characterization of the Electrical Properties of dECM-rGO Hydrogels

Hydrogels were subjected to four-point probe measurements to determine the effect of rGO on material electroconductivity and it was found that dECM-only hydrogels were not highly conductive, with a measured average conductivity (0.0005 ± 0.0002 S/m) two orders of magnitude lower than that of the least conductive dECM-rGO hydrogels. Again, it was found that increasing rGO reduction and content led to corresponding increases in hydrogel electroconductivity (**Figure 2.6**), with average hydrogel conductivities ranging from 0.93 ± 0.12 S/m to 3.07 ± 0.12 S/m, which are approximately 3-10 times greater than reported values for native myocardium[16,17].

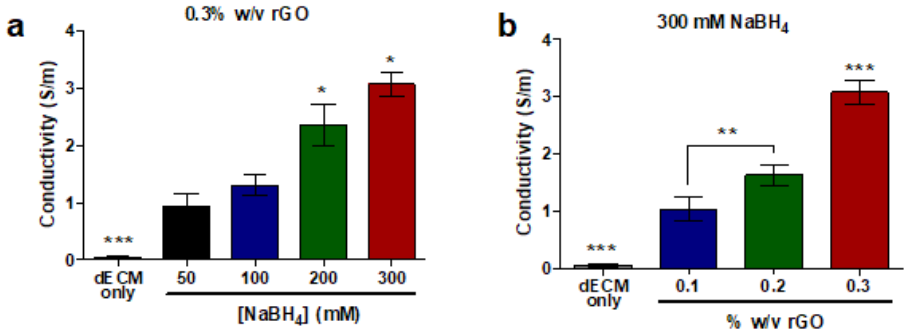

Figure 2.6. Global electroconductivity of dECM-rGO hydrogels is tunable. Hydrogel conductivity was found to increase as a function of (a) degree of rGO reduction and (b) rGO content. *p < 0.05, **p < 0.01, ***p < 0.001 (One-way ANOVA with a Tukey's post-hoc test, n = 6).

2.4.5 Transglutaminase-Mediated Crosslinking of dECM Hydrogels

It should be noted that the observed increases in stiffness due to rGO could not be decoupled from a corresponding increase in conductivity; therefore, in order to have a dECM-based hydrogel that could serve as a stiffness control in subsequent cell-based studies, dECM hydrogels crosslinked with transglutaminase (TG) were utilized[18]. These dECM-TG hydrogels featured compressive moduli similar to that of the stiffest

formulation of dECM-rGO (**Figure 2.7**), and thus fulfilled the requirement for a hydrogel that still possessed the biochemical cues of dECM, but without the enhanced electroconductivity imparted by rGO.

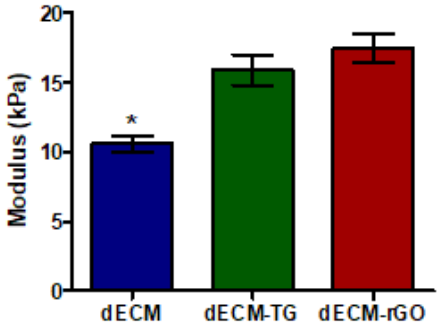

Figure 2.7. The compressive modulus of dECM can be increased with transglutaminase. dECM hydrogels that were further crosslinked with transglutaminase (dECM-TG) possessed compressive moduli comparable to that of the stiffest dECM-rGO hydrogels (0.3% rGO reduced with 300 mM $NaBH_4$). *$p < 0.05$ (One-way ANOVA with a Tukey's post-hoc test, n = 6).

2.5 Discussion

The electrical and mechanical properties of dECM-rGO hydrogels were modulated by the reduction of GO to a more graphene-like sp^2 hybridized lattice structure that imparts high conductivity and mechanical strength[19], and this phenomenon has been observed in other instances where the addition of graphene or rGO to polymer matrices also resulted in corresponding increases in modulus and conductivity[20-23]. While the use of pristine graphene would have likely resulted in hydrogels with even greater electroconductivities and stiffnesses, the relatively hydrophobic nature of graphene compared to rGO does not lend itself well to homogenous dispersion within aqueous matrices, risking tissue-wide inconsistencies in cellular response. Furthermore, residual oxygen-containing groups in rGO could induce the spontaneous adsorption of proteins and thereby act as depots for biomolecules that contribute to cell differentiation and

development[24]. Although transglutaminase-crosslinked dECM was only used as a stiffness control in this study, it is plausible that the modulus of dECM-rGO hydrogels could be further increased with the addition of transglutaminase, thereby providing yet another degree of tunability to the hybrid material. This could prove to be an immensely useful tool for certain applications, such as the modeling of fibrotic and hypertrophic ventricular myocardium, in which a stiffer cell microenvironment is desired[25].

2.6 References

1 Bissell, M. J., Hall, H. G. & Parry, G. How does the extracellular matrix direct gene expression? *J. Theor. Biol.* **99**, 31-68 (1982).

2 Hanson, K. P. *et al.* Spatial and temporal analysis of extracellular matrix proteins in the developing murine heart: a blueprint for regeneration. *Tissue Eng. Part A* **19**, 1132-1143 (2013).

3 Ott, H. C. *et al.* Perfusion-decellularized matrix: using nature's platform to engineer a bioartificial heart. *Nat. Med.* **14**, 213-221 (2008).

4 Martinelli, V. *et al.* Carbon nanotubes instruct physiological growth and functionally mature syncytia: nongenetic engineering of cardiac myocytes. *ACS Nano* **7**, 5746-5756 (2013).

5 Shin, S. R. *et al.* Carbon-nanotube-embedded hydrogel sheets for engineering cardiac constructs and bioactuators. *ACS Nano* **7**, 2369-2380 (2013).

6 Lee, T. J. *et al.* Graphene enhances the cardiomyogenic differentiation of human embryonic stem cells. *Biochem. Biophys. Res. Commun.* **452**, 174-180 (2014).

7 Crowder, S. W. *et al.* Three-dimensional graphene foams promote osteogenic differentiation of human mesenchymal stem cells. *Nanoscale* **5**, 4171-4176 (2013).

8 Yang, H. S. *et al.* Electroconductive nanopatterned substrates for enhanced myogenic differentiation and maturation. *Adv. Healthc. Mater.* **5**, 137-145 (2016).

9 Fleischer, S., Shevach, M., Feiner, R. & Dvir, T. Coiled fiber scaffolds embedded with gold nanoparticles improve the performance of engineered cardiac tissues. *Nanoscale* **6**, 9410-9414 (2014).

10 Pati, F. *et al.* Printing three-dimensional tissue analogues with decellularized extracellular matrix bioink. *Nat. Commun.* **5** (2014).

11 Singelyn, J. M. *et al.* Naturally derived myocardial matrix as an injectable scaffold for cardiac tissue engineering. *Biomaterials* **30**, 5409-5416 (2009).

12 Shin, H. J. *et al.* Efficient reduction of graphite oxide by sodium borohydride and its effect on electrical conductance. *Adv. Funct. Mater.* **19**, 1987-1992 (2009).

13 Williams, C., Quinn, K. P., Georgakoudi, I. & Black, L. D. Young developmental age cardiac extracellular matrix promotes the expansion of neonatal cardiomyocytes in vitro. *Acta Biomater.* **10**, 194-204 (2014).
14 Berry, M. F. *et al.* Mesenchymal stem cell injection after myocardial infarction improves myocardial compliance. *Am. J. Physiol. Heart Circ. Physiol.* **290**, H2196-2203 (2006).
15 Engler, A. J. *et al.* Embryonic cardiomyocytes beat best on a matrix with heart-like elasticity: scar-like rigidity inhibits beating. *J. Cell Sci.* **121**, 3794-3802 (2008).
16 Stinstra, J. G., Hopenfeld, B. & MacLeod, R. S. On the passive cardiac conductivity. *Ann. Biomed. Eng.* **33**, 1743-1751 (2005).
17 Raghavan, K. *et al.* Electrical conductivity and permittivity of murine myocardium. *IEEE Trans. Biomed. Eng.* **56**, 2044-2053 (2009).
18 Orban, J. M. *et al.* Crosslinking of collagen gels by transglutaminase. *J. Biomed. Mater. Res. A* **68a**, 756-762 (2004).
19 Castro Neto, A. H., Guinea, F., Peres, N. M. R., Novoselov, K. S. & Geim, A. K. The electronic properties of graphene. *Rev. Mod. Phys.* **81**, 109-162 (2009).
20 Shin, S. R. *et al.* Reduced graphene oxide-gelMA hybrid hydrogels as scaffolds for cardiac tissue engineering. *Small* **12**, 3677-3689 (2016).
21 Fan, H. L. *et al.* Fabrication, mechanical properties, and biocompatibility of graphene-reinforced chitosan composites. *Biomacromolecules* **11**, 2345-2351 (2010).
22 Zhao, X., Zhang, Q. H., Chen, D. J. & Lu, P. Enhanced mechanical properties of graphene-based poly(vinyl alcohol) composites. *Macromolecules* **43**, 2357-2363 (2010).
23 Rafiee, M. A. *et al.* Enhanced mechanical properties of nanocomposites at low graphene content. *ACS Nano* **3**, 3884-3890 (2009).
24 Lee, W. C. *et al.* Origin of enhanced stem cell growth and differentiation on graphene and graphene oxide. *ACS Nano* **5**, 7334-7341 (2011).
25 Gaasch, W. H., Bing, O. H. & Mirsky, I. Chamber compliance and myocardial stiffness in left ventricular hypertrophy. *Eur. Heart J.* **3 Suppl A**, 139-145 (1982).

Chapter 3. Advanced Functional Maturation of Human iPSC-based Cardiac Tissues Engineered with Electroconductive Decellularized Extracellular Matrices

3.1 Abstract

Human induced pluripotent stem cells (hiPSCs) offer tremendous potential for use in engineering human tissues for therapy and treatment development. However, differentiated cardiomyocytes are phenotypically immature, reducing assay reliability when translating *in vitro* results to clinical studies and precluding hiPSC-derived cardiac tissues from therapeutic use *in vivo*. To address this, we have developed hybrid hydrogels comprised of decellularized myocardial extracellular matrix (dECM) and reduced graphene oxide (rGO) to provide a more instructive microenvironment for proper cellular and tissue development. Engineered heart tissues (EHTs) generated using dECM-rGO hydrogel scaffolds and hiPSC-derived cardiomyocytes exhibited significantly increased twitch forces even after only 14 days of culture, and the expression of genes that regulate contractile function were also increased. Similar improvements various aspects of electrophysiological function, such as calcium-handling, action potential duration, and conduction velocity, were also induced by dECM-rGO. These results highlight the pro-maturation capabilities of this hybrid biomaterial and will be of significant value to researchers seeking to develop *in vitro* drug screening and disease modeling platforms requiring mature hiPSC-derived tissues.

3.2 Introduction

Cardiovascular disease (CVD) remains a leading cause of death for both men and women worldwide, with the economic costs of healthcare related to treatment or quality of life improvements forecasted to exceed $1 trillion per year in the United States alone by 2030[1,2]. With the healthcare burden of CVD increasing every year, considerable research is devoted to engineering cardiac tissues to better understand the underlying disease pathologies, to screen potential pharmacological treatments, and to serve as implantable therapies. The non-proliferative nature of terminally differentiated cardiomyocytes has served as a bottleneck for such work, as obtaining sufficient numbers of cells for studies is ethically and logistically difficult. The advent of human induced pluripotent stem cells (hiPSCs) has somewhat ameliorated this issue since not only are hiPSCs readily obtainable and scalable in culture, hiPSC lines can now be generated from patients with specific disease phenotypes[3,4]. However, cardiomyocytes differentiated from hiPSCs are phenotypically immature and behave more like cells at a neonatal, rather than adult, stage of development[5]. This unfortunately reduces reliability when translating *in vitro* assay results to clinical studies, as immature cells do not accurately reproduce the pharmacological responses and disease progression of the native myocardium.

In vivo, cardiomyocytes are surrounded in three dimensions by a extracellular matrix (ECM) that defines the architecture, signaling, and biomechanics of the cellular microenvironment[6,7]. This regulation of cell behavior by the ECM is known to be due to a precise combination of biochemical, mechanical, structural, and electrical cues. Advances in three-dimensional (3D) tissue engineering approaches have been able to

better recapitulate this cell niche; however, overall cardiomyocyte and engineered cardiac tissue maturity is still at suboptimal levels due to limitations with the scaffolds and platforms that are currently available.

Here, we report on the development of hybrid hydrogels that are comprised of reduced graphene oxide (rGO) dispersed within decellularized myocardial extracellular matrices (dECM). By leveraging the advantages offered by rGO with regards to controlling properties such as stiffness and electroconductivity while maintaining the bioactivity inherent with dECM, this new material can advance the capability to engineer 3D human cardiac tissues that are more physiologically-representative of the native myocardium.

3.3 Materials and Methods

3.3.1 Extracellular Matrix Solubilization and Hydrogel Formation

dECM-based pre-hydrogel solutions were generated by mixing lyophilized dECM and pepsin at a 10:1 mass ratio in 0.1 M HCl. rGO was also added at this stage for dECM-rGO hydrogels. A 2% w/v dECM solution was used for all experiments in this study while the final concentration of the rGO component was varied from 0.1% - 0.3% w/v. Mixtures were stirred constantly until the dECM was completely solubilized and had formed a homogenous solution, at which point the pH was then brought up to 7.4 with 10 M NaOH. Finally, 10% of the final volume of 10X PBS or 10X RPMI 1640 (Sigma-Aldrich) was added to restore isotonic balance. Hydrogel pre-gel solutions were stored at 4ºC until use. Hydrogels were then formed by incubating pre-gel solutions at 37ºC for

at least 12 h. The same solubilization and gelation method was used to generate control hydrogels composed of bovine collagen type I (Advanced BioMatrix). For generating dECM-TG hydrogels for stiffness controls, a 5% w/v solution of transglutaminase (TG; Modernist Pantry) was added to the dECM solution immediately prior to incubation at 37ºC.

3.3.2 Human Induced Pluripotent Stem Cell Culture and Cardiac Differentiation

UC 3-4 urine-derived human induced pluripotent stem cells (hiPSCs)[3,8] were cultured and differentiated using an adaptation of a previously published method of modulating Wnt/β-catenin signaling with small molecules[9]. In brief, hiPSCs were maintained on 1:60 diluted Matrigel-coated plates in mTeSR1 medium (STEMCELL Technologies) prior to induction. Induction is achieved by culturing the cells in RPMI 1640 medium (Invitrogen) supplemented with B-27 without insulin (Invitrogen) and 10 μM CHIR-99021 (Selleck Chemicals) for 18 hrs, after which the medium is replaced with fresh RPMI/B-27 without insulin for 48 hrs. The medium is then replaced with RPMI/B-27 without insulin supplemented with 5 μM IWP-4 (REPROCELL) and cells are cultured for 48 hrs, after which the medium is once again replaced with fresh RPMI/B-27 without insulin for 48 hrs. Finally, medium is replaced with RPMI/B-27 with insulin (Invitrogen), and cultures are fed with fresh medium every other day. Spontaneously beating cells are typically observed 10-12 days after induction. Differentiation runs that produced hiPSC-cardiomyocyte (hiPSC-CM) purity of >90% as measured by flow cytometry after staining for cardiac troponin T (cTnT) were used for all experiments (**Figure 3.1**).

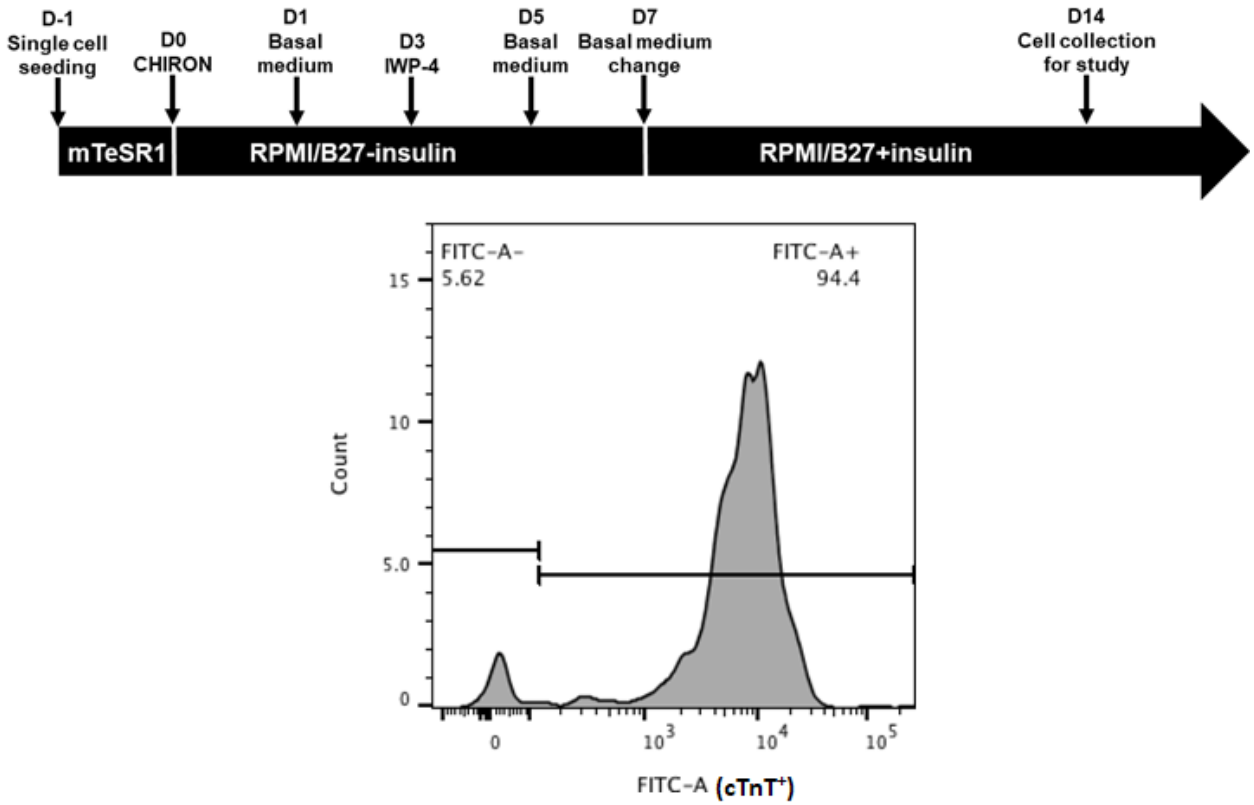

Figure 3.1. hiPSC cardiomyocyte differentiation scheme. UC 3-4 hiPSCs were differentiated into cardiomyocytes using small molecule-mediated Wnt/β-catenin signaling modulating. Beating cardiomyocytes were typically observed 10 – 12 days after induction with CHIR-99021. A representative dataset from flow cytometry of cells positive for cardiac troponin T (cTnT) illustrates the high population purity (94.4%) that is typically achieved using this differentiation method.

3.3.3 Human Stromal Cell Culture

HS-27A human bone marrow-derived stromal cells (ATCC) were cultured and maintained in high-glucose DMEM (Invitrogen) supplemented with 10% fetal bovine serum until used to generate tissues.

3.3.4 Assessment of Biocompatibility

dECM only and dECM-rGO scaffolds containing 0.3% w/v rGO of varying degrees of reduction were seeded with hiPSC-CMs and HS27A stromal cells and cultured for 35

days, after which samples were stained with a live/dead fluorescent assay (Invitrogen) following the protocol provided by the manufacturer and imaged using a widefield epi-fluorescence microscope (Nikon Instruments Eclipse Ti). Live cells appeared as green (calcein-AM excitation/emission λ: 488/515 nm), while dead cells appeared as red (ethidium homodimer-1 excitation/emission λ: 570/602 nm). Quantitative analysis of captured images was performed using ImageJ (National Institutes of Health).

3.3.5 Engineered Heart Tissue Platform Fabrication

The design and fabrication of the hardware utilized for both generating the engineered heart tissues (EHTs) and measuring forces *in situ* has been previously described[10,11]. In brief, post pair arrays were fabricated by pouring uncured polydimethylsiloxane (PDMS; Sylgard 184, Dow Chemical) at a 10:1 base to curing agent ratio into an acrylic mold. A glass capillary tube was inserted into one post of each pair to impart rigidity to that post. Molds were then allowed to de-gas prior to being placed into a 65°C oven overnight to cure the PDMS. Cured post pair arrays were then removed from the mold. Arrays were fabricated in sets of six pairs, with each post 13 mm long and 1.5 mm in diameter and featuring a cap structure 0.5 mm thick and 2 mm in diameter to assist with tissue attachment. Post-to-post spacing was 8 mm. Wells for tissue casting were fabricated by pouring approximately 1 mL of PDMS into the wells of a 24-well culture plate before inserting custom 3D printed molds that would form rectangular wells that were 12 mm x 4 mm x 4mm (length x width x depth). After curing the PDMS overnight, molds were removed. All fabricated hardware was sterilized with 70% v/v ethanol and UV light prior to use.

3.3.6 Generating Engineered Heart Tissue Constructs

hiPSC-CMs and HS-27A stromal cells were mixed in hydrogel pre-gel solutions at cell densities of 20 x 10^6 cells/mL and 5 x 10^6 cells/mL, respectively. 70 µL of this cell-hydrogel mixture was then pipetted into each casted PDMS well, after which PDMS post arrays were positioned upside-down into the wells, ensuring that each post tip was properly immersed in solution. The 24-well plate was then placed into an incubator at 37°C and 5% CO_2 for approximately 60 min, after which the hydrogels had crosslinked and 1 mL of RPMI/B-27 with insulin (supplemented with Y-27632 dihydrochloride ROCK inhibitor and 1% penicillin/streptomycin) was added to each well. After 24 hrs, the media was replaced with fresh RPMI/B-27 with insulin and media changes were conducted every other day until tissue collection for endpoint analyses. Approximately 1 week after casting, tissues typically would have compacted sufficiently that post arrays with attached tissues could be removed from PDMS wells transferred into standard 24-well plates, at which point 2 mL of media per well was used for each media change.

3.3.7 *In Situ* Tissue Contractile Function Measurements and Analysis

Prior to live-tissue imaging, tissues were transferred into a custom-built 24-well plate containing carbon electrodes with the wells filled with warmed Tyrode's buffer with 1.8 mM Ca^{2+}, and the tissues were allowed to stabilize for approximately 30 mins. The plate was then connected to a square-wave electrical stimulator (Grass Instruments S88X) and placed in a heated chamber mounted onto a widefield epi-fluorescence microscope. Videos of at least 5 contractions in duration were recorded using a monochrome CMOS camera (Mightex SMN-B050-U) at 66 frames per second (FPS), with the tissues paced

at 1.5 Hz and with a 5 V square wave amplitude. Image field of view (at 2X magnification) included the entire tissue and the flexible and rigid posts. Using a custom MATLAB script, flexible post deflection was tracked across the duration of each video, which allowed for the calculation of twitch force, time to peak force, time to 90% force decay, contraction velocity, and twitch power[12].

3.3.8 *In Situ* Tissue Electrophysiological Function Measurements and Analysis

Intracellular Ca^{2+} flux and cardiac tissue depolarization characteristics were assessed using fluo-4 AM (Invitrogen) calcium indicator and FluoVolt (Invitrogen) potentiometric dyes, respectively. Engineered heart tissues were washed with warm PBS before being incubated in medium containing either 5 μM of fluo-4 AM or a 1000X dilution of stock FluoVolt for 1 hr at 37°C, after which tissues were washed twice with warm Tyrode's buffer and placed in fresh Tyrode's. Tissues were then imaged using standard FITC settings on a widefield epi-fluorescence microscope with a high-speed color CMOS camera (Hamamatsu ORCA-Flash4.0), with videos taken at 66 FPS and 2X magnification. Tissues for calcium imaging were paced at 1.5 Hz, and fluorescence intensity over time was quantified using NIS Elements software (Nikon) and used to calculate $\Delta F/F_0$ values. For action potential imaging, tissues were not paced, but fluorescence intensity from the FluoVolt dye was again quantified using NIS Elements. APD_{90} and time to peak values were then calculated using a custom MATLAB script[11]. Longitudinal conduction velocity (CV_L) was calculated by measuring the time delay in the onset of depolarization at two regions of interest that were at opposite ends of the tissue's long axis and were a known distance apart.

3.3.9 Gene Expression Analysis

The relative expression levels of selected genes were obtained using reverse-transcription quantitative polymerase chain reaction (RT-qPCR) analyses. After 14 and 35 days of culture, tissues were gently removed from posts and each tissue was placed into an Eppendorf tube containing a 100 µL solution of 2 mg/mL proteinase K in PBS. Tubes were then heated at 56°C for 10 mins before 350 µL of lysis buffer was added. The mixture was vortexed until clear and 250 µL of ethanol was added to the tubes. RNA was then subsequently isolated from this solution by using the RNeasy Plus RNA extraction kit (QIAGEN) according to the manufacturer's protocol. cDNA was then synthesized from the isolated RNA with a reverse transcription kit (iScript Reverse Transcription Supermix, Bio-Rad). Quantity and purity of collected RNA and synthesized cDNA was determined by 260/280 nm absorbance. Synthesized cDNA was then analyzed with qPCR using SYBR green (Bio-Rad) as the reporter and primers used as provided from the manufacturer (Bio-Rad). Relative gene expression was calculated using the comparative Ct method, where *GAPDH* was designated as the housekeeping gene and age-matched hiPSC-derived cardiomyocytes cultured on tissue culture polystyrene (TCPS) were used as controls. Each sample was run in triplicate for each gene.

3.3.10 Immunofluorescent Imaging of Sarcomere Development

EHTs were cultured for 35 days and fixed in 4% paraformaldehyde in PBS overnight at 4°C while the tissues were still mounted on PDMS posts. Fixed tissues were then washed in fresh PBS and placed into a 20% sucrose solution overnight at 4°C. Tissues

were then gently removed from the posts and frozen in optimal cutting temperature (OCT, Tissue-Tek) compound and sectioned into 10 μm slices for storage. Sections were initially blocked with a solution of PBS with 5% goat serum and 0.2% Triton X-100 for 1 hour at room temperature. Afterwards, sections were incubated with primary antibodies for α-actinin (1:200 dilution; Sigma) overnight at 4°C. Sections were washed with PBS and incubated with secondary fluorescent antibodies (1:400 dilution; Invitrogen) for 3 hrs at room temperature, with another series of PBS washes afterwards. Mounting media containing DAPI (Vectashield, Vector Laboratories) was then applied along with a coverslip, and stained sections were then stored at 4°C in the dark until imaging. Tissue sections were imaged using a confocal microscope (Nikon Instruments A1R) at 60X magnification with oil immersion. Analysis of sarcomere lengths and Z-band widths was conducted using ImageJ software.

3.3.11 Statistical Analyses

Unless otherwise noted, all quantitative data is presented as means ± standard error. One-way ANOVA with a Tukey's *post-hoc* test was used to analyze data sets that included more than two experimental groups, while a Student's *t*-test was used to compare data sets looking at only two variables. In all presented analyses, $p < 0.05$ was considered significant.

3.4 Results

3.4.1 dECM-rGO Hydrogels Support Long-Term Biocompatibility

Cytotoxic effects from highly-conductive carbon lattice-based materials, such as graphene, graphene oxide, and carbon nanotubes, have been reported in literature[13,14]. An assessment of the biocompatibility of dECM-rGO hydrogels, however, demonstrated that the presence of rGO had no long-term negative effects on cardiomyocyte and stromal cell viability (> 90% viable), even at the highest concentrations used in this study (**Figure 3.2**).

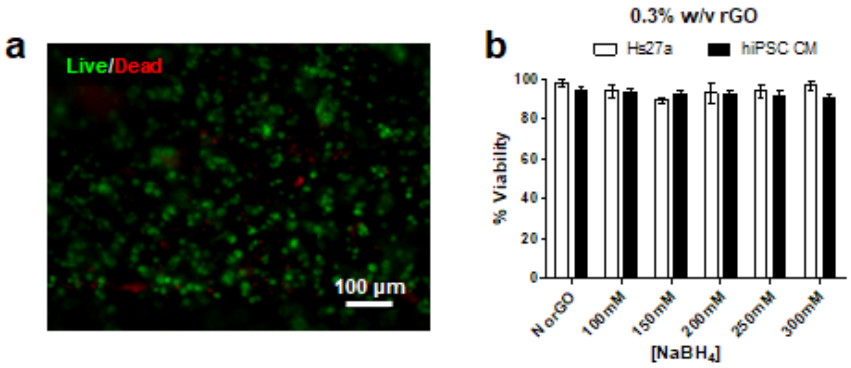

Figure 3.2. dECM-rGO hydrogel biocompatibility. (a) Representative live/dead fluorescent image of a cardiomyocyte and stromal cell mixture cultured on dECM-rGO after 35 days. Live cells are labeled green and dead cells are labeled red. (b) High viability of both cell types is maintained even on hydrogels with high rGO content and degree of reduction.

3.4.2 dECM-rGO Hydrogels Enhance Engineered Cardiac Tissue Contractile Function and Maturation

Three-dimensional engineered heart tissues (EHTs) were generated by casting a mixture of hiPSC-derived cardiomyocytes, human bone marrow-derived stromal cells, and pre-hydrogel solution around silicone posts that enabled *in situ* twitch force

measurements *via* post deflection imaging (**Figure 3.3a**, **Supplementary Videos 1 & 2**). In these studies, collagen I hydrogel was selected as a control scaffold material that was closest in approximation to the biochemical make-up of dECM and is commonly used to fabricate 3D cardiac tissues. Additionally, the stiffest and most electroconductive dECM-rGO composition (dECM with 0.3% w/v 300 mM $NaBH_4$ rGO) was used, and as mentioned previously, dECM-TG served as a stiffness control. EHTs were cultured over a 35-day period, with their contractile performance analyzed every 7 days. While no difference in twitch force was found in the first 7 days, a significant increase in force output was detected in dECM-rGO tissues on Day 14 (**Figure 3.3b**). Specifically, the dECM-rGO tissues produced twitch forces nearly twice that of the next closest group (23.61 ± 2.62 μN vs. 12.97 ± 3.00 μN, dECM-rGO vs. dECM-TG, respectively), and nearly five times that of the collagen tissues (23.61 ± 2.62 μN vs. 5.33 ± 2.36 μN). Noting this striking improvement in contractile function at Day 14, all subsequent experimental endpoints and data analyses were performed for Day 14 and Day 35 time points. dECM-rGO tissues continued to produce greater twitch forces compared to the other tissue groups over the entire culture period, with dECM-TG tissues consistently generating the next greatest force output, followed by dECM-only tissues, and lastly by collagen tissues. However, it was interesting to observe that at Day 28 and Day 35, it appeared that the advantage in force generation by dECM-rGO tissues was beginning to diminish, with dECM-TG and dECM tissues producing nearly identical twitch forces (approximately 45 μN). Meanwhile, force output of the collagen tissues had essentially plateaued by Day 28 to 28.99 ± 1.37 μN.

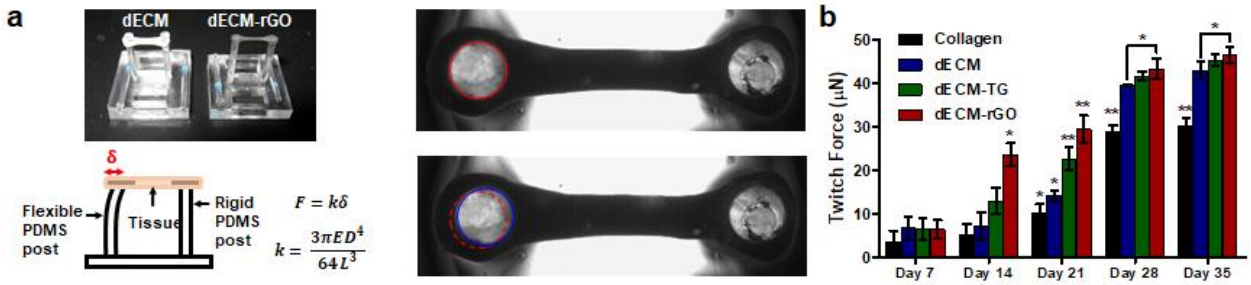

Figure 3.3. Measurement and analysis of EHT twitch force production. (a) Representative photographs of dECM and dECM-rGO tissues formed on the two-post EHT platform and schematic illustrating the beam theory that allows for quantitative analysis of contractile function using the EHT platform. Snapshots of twitching EHTs (right), in which post deflection is indicated by the relative position of the post cap at two different time points (red and blue circles). (b) Twitch forces generated by dECM-rGO tissues is significantly greater than controls across all time points after Day 7, with the greatest difference observed on Day 14. Twitch forces appear to plateau after Day 28. *p < 0.05, **p < 0.01 (One-way ANOVA with a Tukey's *post-hoc* test, n = 12).

Twitch power generated by EHTs followed a similar trend, with dECM-rGO tissues producing greater power at both Day 14 and Day 35 while no significant difference was found between dECM and dECM-TG tissues at the latter time point (**Figure 3.4**).

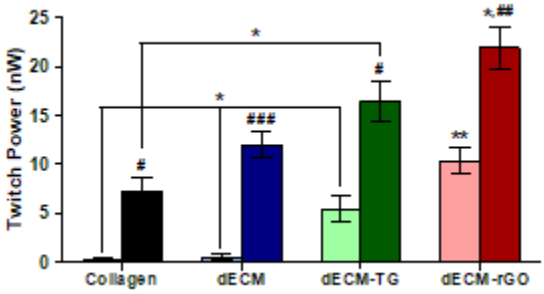

Figure 3.4. Twitch power generated by EHTs. Twitch power generated by dECM-rGO tissues is significantly greater than controls at both time points. No significant difference is observed between dECM and dECM-TG tissues at Day 35. *p < 0.05, **p < 0.01 (hydrogel material comparison; One-way ANOVA with a Tukey's *post-hoc* test, n = 6); $^{\#}$p < 0.05, $^{\#\#}$p < 0.01, $^{\#\#\#}$p < 0.001 (time point comparison; Student's *t*-test, n = 12).

Examining the contractile kinetics of the EHTs, it was found that not only did the dECM-rGO tissues outperform the rest in terms of twitch force generation, but were also able both to reach maximal force (**Figure 3.5a**) and relax to 90% force (**Figure 3.5b**) at a faster rate per contraction, thereby attaining significantly greater contraction velocities

(**Figure 3.5c**). Notably, there was no significant difference in times to peak and 90% relaxation between Days 14 and 35 for dECM-rGO tissues, while all other tissue groups displayed improvements in these metrics over time. Additionally, while the contraction kinetics of dECM and collagen tissues were comparable to each other at Day 14, by Day 35, dECM tissues were outperforming their collagen counterparts.

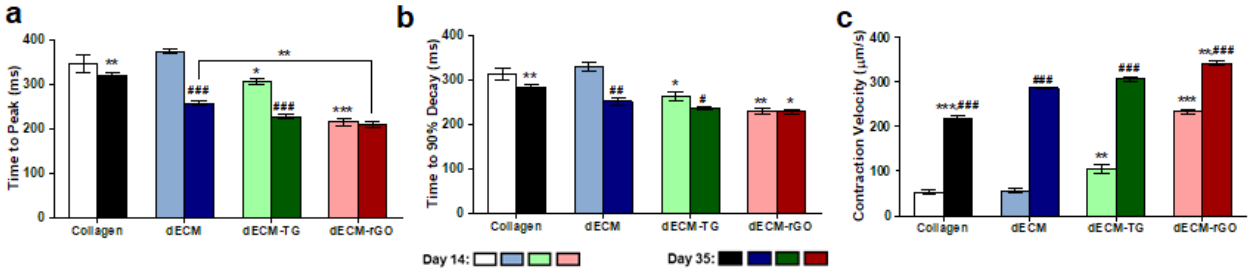

Figure 3.5. Analysis of scaffold-mediated EHT contractile kinetics. (a) dECM-rGO tissues generate maximal twitch forces quicker than other groups at both Day 14 and Day 35, and (b) reach 90% relaxation quicker than other groups at both time points as well. (c) As such, dECM-rGO tissues feature significantly greater contraction velocities than tissues formed with other hydrogels. *p < 0.05, **p < 0.01, ***p < 0.001 (hydrogel material comparison; One-way ANOVA with a Tukey's *post-hoc* test, n = 12); $^{\#}$p < 0.05, $^{\#\#}$p < 0.01, $^{\#\#\#}$p < 0.001 (time point comparison; Student's *t*-test, n = 12).

With the observed enhancement of EHT contractile performance due to dECM-rGO hydrogel scaffolds, the expression of several genes that code for cardiomyocyte contraction-mediating proteins was analyzed and compared to tissue culture polystyrene (TCPS) cell monolayer controls. Expression of *MYH7*, which codes for β-myosin heavy chain (β-MHC), was significantly more elevated in dECM-rGO tissues on Day 14 (**Figure 3.6a**). MYH7 expression was significantly increased for all groups at Day 35, but relative levels were still lower than seen in the dECM-rGO group. Similar trends were observed for *TNNT2*, or cardiac troponin T (cTnT), although in this case both dECM-TG and dECM-rGO tissues had greater expression levels at both time points compared to the others (**Figure 3.6b**). Upregulation of these genes corresponded well with the collected twitch force data, as cTnT and β-MHC regulate the force

generation capacity of cardiomyocytes and are considered late-stage markers of cardiac development[15-17]. Troponin I is another critical component of the myocyte contractile machinery, and a comparison of troponin I isoforms can also shed light on the maturation state of cardiomyocytes, as cells with a fetal or neonatal phenotype will largely express *TNNI1* (skeletal slow TnI/ssTnI), while adult cardiomyocytes will exclusively express *TNNI3* (cardiac TnI/cTnI)[5,18,19]. Thus, the significantly higher ratio of expression of *TNNI3* to *TNNI1* in dECM-rGO tissues at both time points indicates that this hydrogel composition enhances the maturation of these tissues and is an important driver of improved contractile function (**Figure 3.6c**). Additionally, although there is no significant difference in TNNI3:TNNI1 between dECM and dECM-TG tissues, both possess a greater amount of the cardiac isoform than the collagen and TCPS controls. At both time points, the expression levels of titin (*TTN*), the protein responsible for muscle elasticity, were comparable between dECM-TG and dECM-rGO, which were in turn greater than that in dECM and collagen (**Figure 3.6d**). Furthermore, the ratio of the *N2B* to *N2BA* isoforms of titin was drastically higher in dECM-rGO tissues at both Day 14 and Day 35, another indication that the maturation state of these cardiomyocytes was significantly improved by the composite hydrogel (**Figure 3.6e**). Indeed, the increased presence of the N2B isoform in adult myocardium and resulting increase in passive stiffness is what allows for rapid ventricular recoil[20], which correlates well with the observed decrease in relaxation time in dECM-rGO tissues.

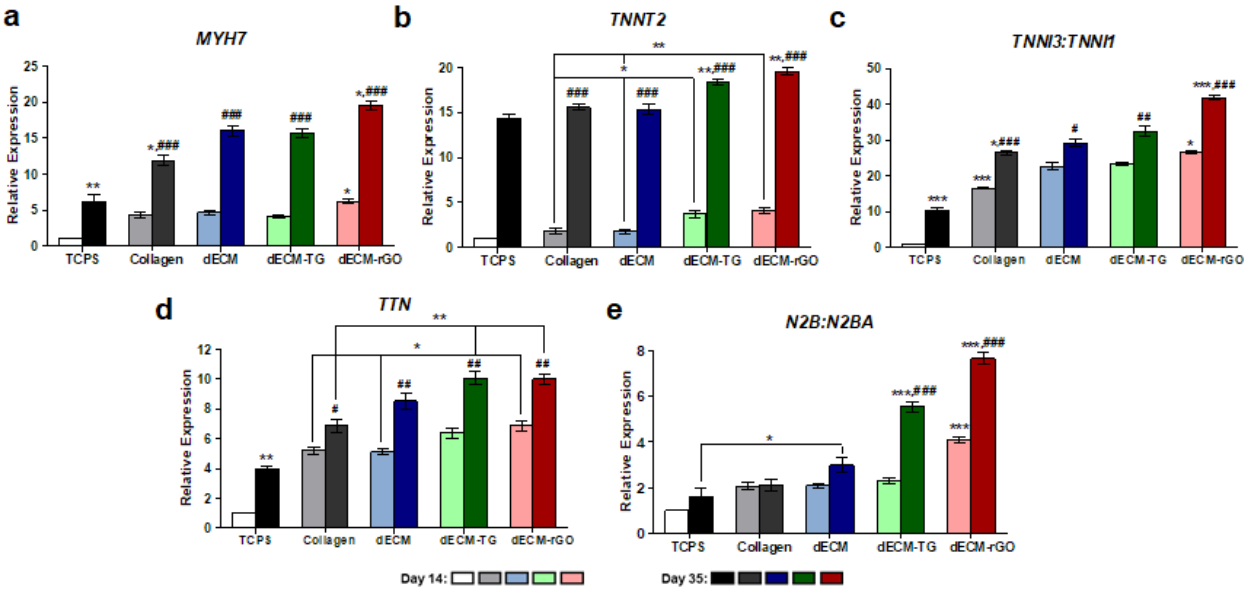

Figure 3.6. Relative expression analysis of genes encoding cardiomyocyte structural and contractile proteins. (a) RT-qPCR analysis of *MYH7* shows that expression levels in dECM-rGO tissues is greater than controls that show no significant difference between them at Day 14, and is still greater at Day 35. (b) Expression of *TNNT2* in dECM-TG and dECM-rGO tissues is greater at both time points, with no significant difference observed between collagen and dECM tissues. (c) Relative expression ratios of cardiac (*TNNI3*) and skeletal (*TNNI1*) isoforms of troponin I show a greater induced expression of the cardiac-specific gene in dECM-rGO tissues. (d) Overall expression of titin (*TTN*) is increased in dECM-rGO tissues on Day 14, but this increase is not statistically-significant from that of dECM-TG. On Day 35, both dECM-TG and dECM-rGO have increased expression of *TTN* relative to collagen, but this difference is not significant compared to dECM. (e) However, when looking at the expression ratios of *N2B* to *N2BA*, dECM-rGO tissues show a significant increase at Day 14, while both dECM-rGO and dECM-TG tissues have vastly larger expression levels relative to others at Day 35. *p < 0.05, **p < 0.01, ***p < 0.001 (hydrogel material comparison; One-way ANOVA with a Tukey's *post-hoc* test, n = 12); #p < 0.05, ##p < 0.01, ###p < 0.001 (time point comparison; Student's *t*-test, n = 12).

3.4.3 Sarcomere Development is Enhanced in dECM-rGO EHTs

Sarcomeres are the basic contractile unit of striated muscle and their structural properties directly impact force production[21]. As such, EHTs were sectioned and immunostained for sarcomeric α-actinin to assess how sarcomere development was influenced by scaffold material composition (**Figure 3.7a**). Sarcomeres were shortest in collagen tissues (1.78 ± 0.01 μm) and progressively lengthened as the hydrogel scaffolds were more biochemically diverse, stiffer, and electroconductive, with the longest sarcomeres (2.11 ± 0.02 μm) found in dECM-rGO tissues (**Figure 3.7b**). For

comparison, sarcomeres in adult human cardiomyocytes are reported to be approximately 2.2 μm in length[22], while immature cardiomyocytes typically have sarcomeres that are only about 1.5 – 1.65 μm long[23]. In addition to sarcomere length, the lateral alignment of adjacent sarcomeres plays an important role in contraction synchronicity and overall force output. Sarcomere register is typically assessed as a function of Z-band width, where cardiomyocytes capable of generating more twitch power feature wider Z-bands[24]. Similar to the trend observed with sarcomere length, Z-bands were shortest in collagen tissues (3.12 ± 0.12 μm) and widest in dECM-rGO tissues (3.92 ± 0.13 μm), although statistical difference was only found for the dECM-rGO group (**Figure 3.7c**).

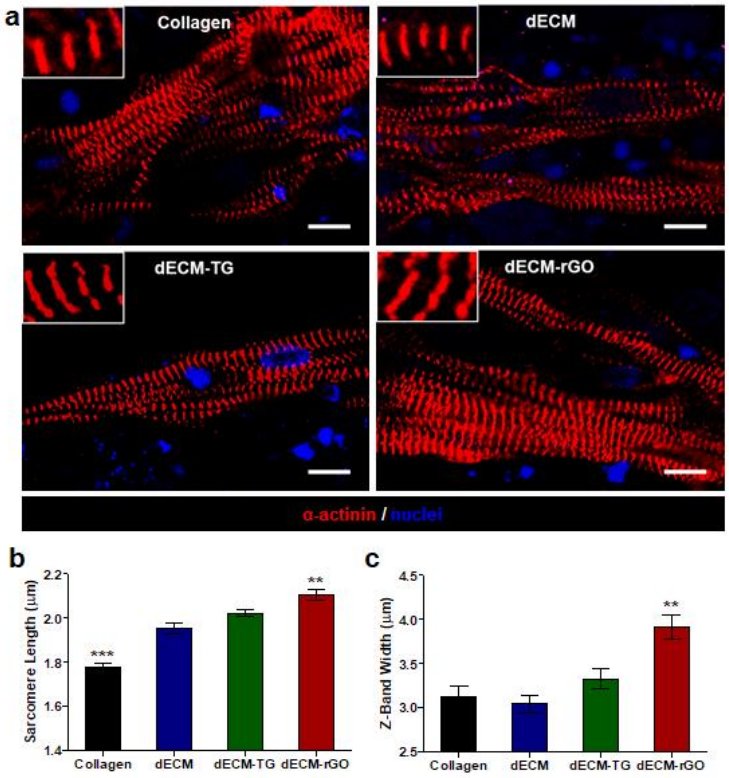

Figure 3.7. Sarcomere development in engineered heart tissues. (a) Representative fluorescent images of tissues generated with the different hydrogels stained for sarcomeric α-actinin (red) and nuclei (blue). Scale bar = 10 μm. (b) Sarcomere length and (c) Z-band widths are increased in dECM-rGO tissues relative to other tissues, with sarcomere lengths approaching those observed in adult human cardiomyocytes.**p < 0.01, ***p < 0.001 (One-way ANOVA with a Tukey's *post-hoc* test, n = 6).

3.4.4 Enhanced EHT Electrophysiological Function Mediated by dECM-rGO

Calcium plays an important role in regulating the excitation-contraction coupling processes that are required for proper cardiac function. To determine the impact of scaffold material on the Ca^{2+}-handling capabilities of EHTs, a Ca^{2+}-sensing fluorescent dye was used to monitor changes in intracellular Ca^{2+} levels during contractions (**Figure 3.8a**). At both Day 14 and Day 35, the normalized average change in fluorescence intensity was found to be significantly greater in dECM-rGO tissues versus its dECM counterparts, an indication of increased Ca^{2+} influx and thus a greater concentration of calcium present in these tissues each contraction cycle (**Figure 3.8b**). Additionally, while Ca^{2+} transients increased over time for dECM-rGO tissues, transient levels remained relatively unchanged for dECM tissues. An examination of expression levels for ion channels involved in maintaining cytosolic calcium homeostasis, *CACNA1C* (L-type Ca^{2+} channel $Ca_V1.2$) and *ATP2A2* (Ca^{2+}-ATPase; SERCA2), shows significantly elevated expression of both genes in dECM-rGO tissues compared to all other tissue types, with *ATP2A2* expression further increased on Day 35 (**Figure 3.8c, d**).

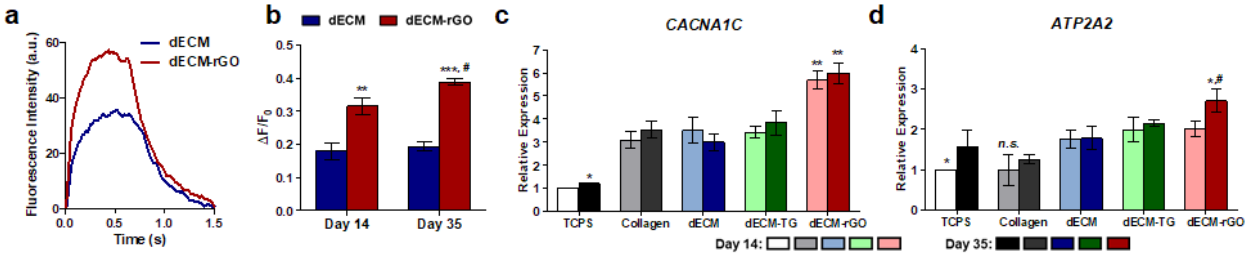

Figure 3.8. Calcium-handling improvements in dECM-rGO EHTs. (a) Representative trace of fluorescence intensity obtained from live-tissue imaging of Fluo-4 AM. (b) Change in fluorescence is significantly greater in dECM-rGO tissues at both Day 14 and Day 35, indicating greater Ca^{2+} flux across cardiomyocyte membranes. (c) RT-qPCR analysis of *CACNA1C* and (d) *ATP2A2* indicates that expression of these Ca^{2+} channel components is greater in dECM-rGO tissues, suggesting that calcium-handling capabilities are improved by the composite hydrogel scaffold. *$p < 0.05$, **$p < 0.01$, ***$p < 0.001$ (hydrogel material comparison; One-way ANOVA with a Tukey's *post-hoc* test, n = 12); $^{\#}p < 0.05$ (time point comparison; Student's *t*-test, n = 12).

To further characterize the electrophysiological function of these EHTs, a voltage-sensing fluorescent dye was used to investigate action potential behavior (**Figure 3.9a**). Action potential duration at 90% repolarization (APD_{90}), commonly used as an analog for QT interval, was observed to be significantly longer in dECM-rGO tissues (487.87 ± 20.58 ms) than in dECM tissues (343.30 ± 10.64 ms) at Day 14. At Day 35, however, both tissues had similar APD_{90} values at 476.81 ± 25.23 ms and 504.20 ± 12.27 ms, for dECM and dECM-rGO, respectively (**Figure 3.9b**). For comparison, QT intervals in adult humans are generally reported to be in the 350 – 460 ms range[25]. In examining the expression of several K^+ channels that contribute to the plateau phase of cardiomyocyte action potentials, it was found that *KCNH2* (human ether-a-go-go-related-gene; hERG) (**Figure 3.9c**) and *KCNE1* (**Figure 3.9d**) were upregulated in dECM-rGO tissues by a massive margin at both Day 14 and Day 35, with no significant change in expression between the two time points. Meanwhile, expression of *KCNJ2* ($K_{IR}2.1$) (**Figure 3.9e**) and *KCNQ1* (**Figure 3.9f**) was not significantly different between tissues generated with dECM-based hydrogels; however, expression levels were much greater than that of the collagen and TCPS controls. Moreover, expression of these two genes was found to increase significantly over time for all three of the dECM-based hydrogel groups. The variations in the expression levels of these particular K^+ channels could explain the observed trends in APD_{90}. The significant upregulation of *KCNH2* and *KCNE1* in dECM-rGO tissues could account for its longer APD_{90} at Day 14. Then, as additional K^+ channels such as *KCNJ2* and *KCNQ1* become more numerous in dECM tissues over time, APD_{90} values begin to equalize, as seen with the Day 35 analysis. In addition to an increase in APD_{90} mediated by dECM-rGO, the time to peak

depolarization was significantly reduced at Day 14 in these tissues (**Figure 3.9g**). Similar to the trend observed for APD_{90}, there was no significant difference in time to peak depolarization between dECM and dECM-rGO tissues at Day 35. Expression of *SCN5A*, which codes for the voltage-gated Na^+ channel $Na_V1.5$ that is responsible for mediating membrane depolarization in cardiomyocytes, was found to be much higher in dECM-rGO tissues at Day 14, although no difference in expression was found amongst the three dECM-based tissues at Day 35 despite an overall upregulation across these groups (**Figure 3.9h**). Like with the K^+ channel expression patterns, this result likely explains the comparable depolarization rates between dECM and dECM-rGO tissues that were seen at the later time point.

Data collected from the voltage-sensing dye was also used to calculate the longitudinal conduction velocity (CV_L) in EHTs. At both time points, conduction velocity was significantly greater in dECM-rGO tissues than in their dECM counterparts, with a peak CV_L of 35.36 ± 2.32 cm/s recorded at Day 35 (**Figure 3.9i**), which is strikingly similar to the reported mean conduction velocity of isolated human left ventricular myocardium (49.8 ± 3.8 cm/s)[26]. Since electrical signal transmission between cardiomyocytes has been shown to be closely associated with connexin 43 (Cx43) gap junction formation[27], the expression of the gene that codes for this protein was examined. Indeed, *GJA1* expression was found to be significantly greater in dECM-rGO tissues, although no difference in expression levels was seen between the early and late time points in all tissues (**Figure 3.9j**).

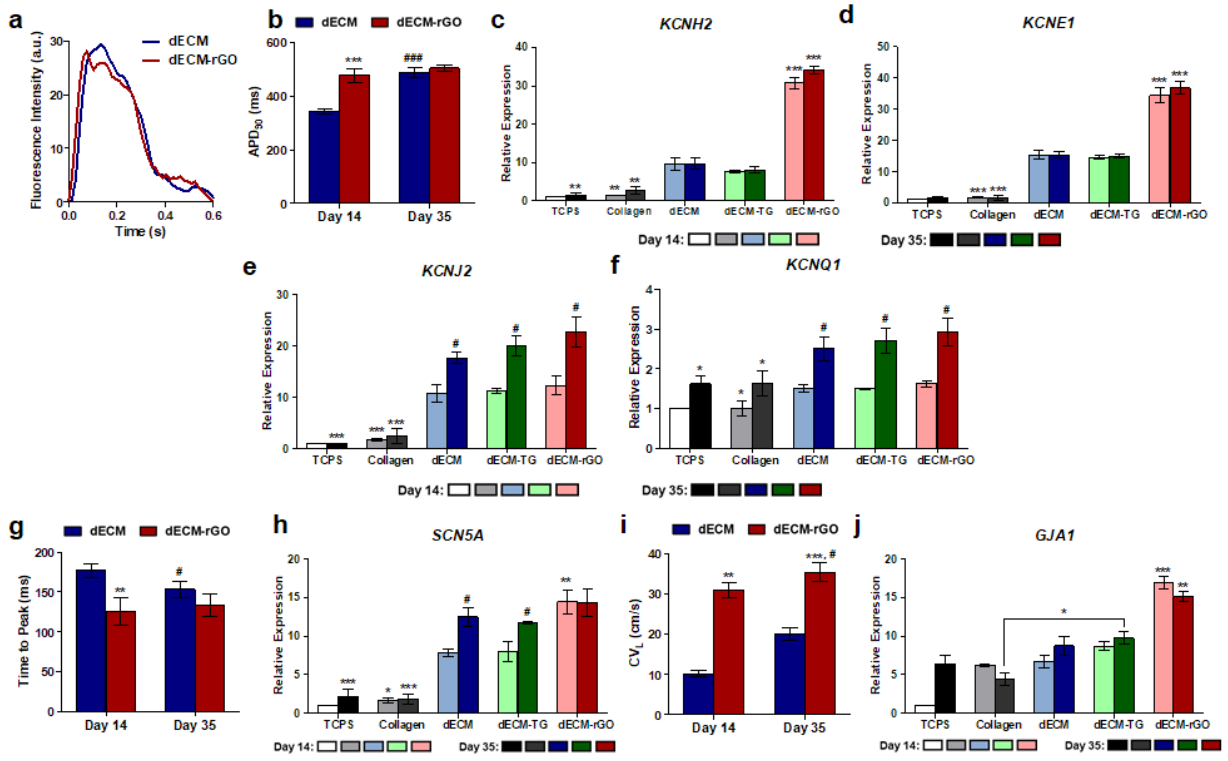

Figure 3.9. Improved ion channel development and action potential characteristics of dECM-rGO tissues. (a) Representative trace of fluorescence intensity obtained from live-tissue imaging of FluoVolt. (b) Quantitative analysis of voltage dye traces shows that APD_{90}, an analog for QT interval, is lengthened in dECM-rGO tissues at Day 14. By Day 35, there is no significant difference in APD_{90} values between both groups. (c) RT-qPCR analysis of *KCNH2* (hERG channel) expression and (d) *KCNE1* (voltage-gated K^+ channel subunit MiRP1) expression show a dramatic increase in dECM-rGO tissues across both time points. (e) Expression of *KCNJ2* and (f) *KCNQ1*, on the other hand, was comparable across all tissues engineered with dECM-based scaffolds although expression increased over time. (g) Time to peak depolarization is significantly reduced in dECM-rGO tissues compared to dECM counterparts. (h) Expression of *SCN5A* is significantly greater in dECM-rGO tissues at Day 14, but not on Day 35. (i) Longitudinal conduction velocity is greater in dECM-rGO tissues at both Day 14 and Day 35, and this corresponds with (j) a marked increase in *GJA1* (Cx43) expression in these tissues. *p < 0.05, **p < 0.01, ***p < 0.001 (hydrogel material comparison; One-way ANOVA with a Tukey's *post-hoc* test, n = 12); #p < 0.05 (time point comparison; Student's *t*-test, n = 12).

3.4.5 Regulation of Transcription Factor Expression by Hydrogel Composition

Transcriptional factors are known to play an important role in determining cell fate and tissue morphogenesis. In developing cardiac tissues, Nkx2.5 and GATA4 are highly expressed in the pre-cardiac mesoderm and in cardiac progenitor cells and numerous gain/loss of function studies have shown that these two factors work in concert to drive

the cardiomyocyte differentiation process[28-30]. RT-qPCR analysis of *NKX2.5* and *GATA4* expression in EHTs at Day 14 show a that although all four of the tested hydrogel scaffolds induced higher expression levels than what were seen in 2D cultured cells, only dECM-rGO tissues had a significantly greater expression level than collagen controls (**Figure 3.10**). However, as EHTs became more mature over time, the expression of both genes saw a significant decrease. A clear spectrum of expression reduction magnitude was found to be closely tied to the type of scaffold material used; as the microenvironmental cues became more complex, the decrease in expression became greater. In fact, TCPS actually elicited an increase in expression in cardiomyocytes. These results serve to illustrate the impact on maturation rate that is elicited by 3D dECM-based hydrogels, and by dECM-rGO in particular.

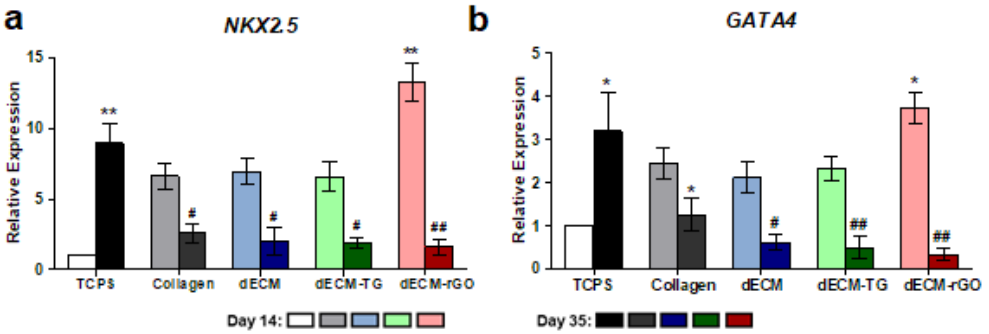

Figure 3.10. Hydrogel-mediated transcription factor expression over time. (a) dECM-rGO elicited a significant increase in expression of *NKX2.5* at Day 14, and all other 3D tissues had higher expression levels than TCPS controls. By Day 35, expression was comparable between all tissues. (b) Similar trends in relative expression over time were observed for *GATA4*, where dECM-rGO tissues had high levels of expression at Day 14 but had reduced expression by Day 35. *p < 0.05, **p < 0.01 (hydrogel material comparison; One-way ANOVA with a Tukey's *post-hoc* test, n = 12); #p < 0.05, ##p < 0.01 (time point comparison; Student's *t*-test, n = 12).

3.5 Discussion

The results of this study demonstrate the capability of dECM-rGO hybrid hydrogels to improve the functional phenotype of engineered cardiac tissues such that they can produce physiological responses to external stimuli.

In terms of twitch force production and contraction kinetics, the performance of dECM-only and collagen tissues were comparable at the early time point, and this was also reflected in the expression profiles of the selected genes. However, as time went on, the dECM appeared to confer a distinct advantage on inducing maturation, with notable gains in functional output and the expression of genes encoding titin and cTnI. dECM-mediated improvements in electrophysiological function were observed to occur even sooner in culture, with the greatest effect seen on K^+ and Na^+ channel gene expression. These effects can be attributed to the fact that although dECM hydrogels are a homogenization of many intra-tissue niches and the decellularization process slightly alters native tissue protein composition, compared to single component biomaterials like collagen, dECM-based materials are unique in that they are still capable of presenting a cell microenvironment with a wider spectrum of tissue-specific biochemical cues that are essential for supporting proper development. Indeed, similar findings have been reported in which dECM scaffolds have been found to exert enhanced differentiation and development on a variety of tissue types *in vitro*[31-34], as well as pro-regenerative effects on skeletal muscle[35-37] and myocardium[38,39] *in vivo*.

Like most other naturally-derived scaffold hydrogels, however, there is a modulus mismatch between dECM and native tissue. The proper tuning of matrix stiffness has proven to be a critical factor in successfully engineering cardiac tissues, as prior studies

have found that the development of cardiomyocyte contractile function and striation is significantly improved in microenvironments that closely approximate myocardial stiffnesses[24,40,41]. This is somewhat unsurprising, as there is a large body of evidence that implicates the role of integrins in translating biomechanical signals to determine cell fate and that myofibril assembly starts at these integrin adhesion sites[42-44]. The results presented here are consistent with those findings, as the stiffer dECM-TG and dECM-rGO hydrogels generated tissues that produced greater twitch forces and velocities, and an increased expression of *TNNT2*, *TNNI3*, *TTN*, and *N2B*. Sarcomere formation was also improved by a corresponding increase in matrix stiffness. Surprisingly, the relative expressions of the various ion channels and *GJA1* in dECM and dECM-TG tissues were statistically comparable, which suggests that matrix stiffness appears to have a limited effect on regulating this subset of electrophysiological development. Further examination of integrin-mediated signaling pathways is clearly needed; however, a study conducted with neonatal rat ventricular cardiomyocytes showed that even though substrates with biomimetic stiffnesses induced increased action potential duration and calcium flux, L-type Ca^{2+} channel expression in these cells was unchanged[45].

Based on the stark improvement of EHT contractile and electrophysiological function and increased expression of associated developmental markers within these tissues, it is evident that rGO exerts a profound effect on multiple aspects of hiPSC-derived cardiomyocyte maturation. While there is an abundance of examples in which electroconductive scaffolds have been shown to enhance the maturation and function of cardiomyocytes[46-51], the mechanisms and signaling pathways mediated by these types of materials have yet to be fully elucidated. In almost all reported cases, however, the

most significant improvements in performance were in parameters related to electrical coupling, such as conduction velocity and Cx43/*GJA1* expression. This implies that although electroconductivity still plays a role in upregulating other cardiac-specific proteins and transcription factors, it appears that the largest impact is on promoting electrophysiological development of these cells. The recent discovery that cells cultured on graphene exhibited an enrichment of the cholesterol content in their membranes raises interesting questions on what downstream effects this would potentially regulate[52]. For example, since membrane cholesterol has been shown to regulate G protein-coupled receptor (GPCR) activity[53], an increase in cholesterol could result in a corresponding increase in the activity of GPCRs, such as sphingosine 1-phosphate receptor-1, that contribute to normal cardiac development[54]. It has also been found that gap junctions like Cx43 and K_V channels like hERG localize to cholesterol-rich membrane domains, and that alteration of this membrane lipid environment can modulate the function of these proteins[55-57]. Furthermore, an increase in plasma membrane cholesterol content has been shown to increased Ca^{2+} flux through membrane calcium channels in a number of different cell types, including cardiomyocytes[58-60]. Culturing cells in an electrically conductive environment could also induce hyperpolarization of the resting membrane potential, which has been demonstrated to have a strong correlation with cardiomyocyte differentiation and maturation *via* calcineurin-mediated processes[61].

Thus, with the synergistically beneficial combination of biochemical, mechanical, and electroconductive cues offered by dECM-rGO hydrogels, a more pronounced maturation response was observed than in other 3D human stem cell-based cardiac

tissue engineering approaches where single-component hydrogel scaffolds (specifically collagen or fibrin) were used[62-64]. Notably, the expression of some genes associated with the cardiomyocyte contractile apparatus, namely *MYH7* and *TNNT2*, was found to be relatively lower than those in which engineered tissues underwent cyclic physical conditioning[65,66], suggesting that if dECM-rGO scaffolds were to be utilized in similar bioreactor systems, further gains in contractile phenotype maturation could be achieved.

3.6 References

1 Celermajer, D. S., Chow, C. K., Marijon, E., Anstey, N. M. & Woo, K. S. Cardiovascular disease in the developing world: prevalences, patterns, and the potential of early disease detection. *J. Am. Coll. Cardiol.* **60**, 1207-1216 (2012).

2 Heidenreich, P. A. *et al.* Forecasting the future of cardiovascular disease in the United States: a policy statement from the American Heart Association. *Circulation* **123**, 933-944 (2011).

3 Guan, X. *et al.* Dystrophin-deficient cardiomyocytes derived from human urine: New biologic reagents for drug discovery. *Stem Cell Res.* **12**, 467-480 (2014).

4 Young, C. S. *et al.* A single CRISPR-Cas9 deletion strategy that targets the majority of DMD patients restores dystrophin function in hiPSC-derived muscle cells. *Cell Stem Cell* **18**, 533-540 (2016).

5 Yang, X., Pabon, L. & Murry, C. E. Engineering adolescence: maturation of human pluripotent stem cell-derived cardiomyocytes. *Circ. Res.* **114**, 511-523 (2014).

6 Bissell, M. J., Hall, H. G. & Parry, G. How does the extracellular matrix direct gene expression? *J. Theor. Biol.* **99**, 31-68 (1982).

7 Hanson, K. P. *et al.* Spatial and temporal analysis of extracellular matrix proteins in the developing murine heart: a blueprint for regeneration. *Tissue Eng. Part A* **19**, 1132-1143 (2013).

8 Macadangdang, J. *et al.* Nanopatterned human iPSC-based model of a dystrophin-null cardiomyopathic phenotype. *Cell. Mol. Bioeng.* **8**, 320-332 (2015).

9 Lian, X. J. *et al.* Directed cardiomyocyte differentiation from human pluripotent stem cells by modulating Wnt/beta-catenin signaling under fully defined conditions. *Nat. Protoc.* **8**, 162-175 (2013).

10 Bielawski, K. S., Leonard, A., Bhandari, S., Murry, C. E. & Sniadecki, N. J. Real-time force and frequency analysis of engineered human heart tissue derived from induced pluripotent stem cells using magnetic sensing. *Tissue Eng. Part C Methods* **22**, 932-940 (2016).

11 Leonard, A. *et al.* Afterload promotes maturation of human induced pluripotent stem cell derived cardiomyocytes in engineered heart tissues. *J. Mol. Cell. Cardiol.* **118**, 147-158 (2018).
12 Sniadecki, N. J. & Chen, C. S. Microfabricated silicone elastomeric post arrays for measuring traction forces of adherent cells. *Methods Cell. Biol.* **83**, 313-+ (2007).
13 Liao, K. H., Lin, Y. S., Macosko, C. W. & Haynes, C. L. Cytotoxicity of graphene oxide and graphene in human erythrocytes and skin fibroblasts. *ACS Appl. Mater. Interfaces* **3**, 2607-2615 (2011).
14 Zhang, Y. B. *et al.* Cytotoxicity effects of graphene and single-wall carbon nanotubes in neural phaeochromocytoma-derived PC12 cells. *ACS Nano* **4**, 3181-3186 (2010).
15 Sehnert, A. J. *et al.* Cardiac troponin T is essential in sarcomere assembly and cardiac contractility. *Nat. Genet.* **31**, 106-110 (2002).
16 Witjas-Paalberends, E. R. *et al.* Mutations in MYH7 reduce the force generating capacity of sarcomeres in human familial hypertrophic cardiomyopathy. *Cardiovasc. Res.* **99**, 432-441 (2013).
17 Anderson, P. A. W. *et al.* Molecular-basis of human cardiac troponin-T isoforms expressed in the developing, adult, and failing heart. *Circ. Res.* **76**, 681-686 (1995).
18 Hunkeler, N. M., Kullman, J. & Murphy, A. M. Troponin-I isoform expression in human heart. *Circ. Res.* **69**, 1409-1414 (1991).
19 Westfall, M. V., Samuelson, L. C. & Metzger, J. M. Troponin I isoform expression is developmentally regulated in differentiating embryonic stem cell-derived cardiac myocytes. *Dev. Dyn.* **206**, 24-38 (1996).
20 Lahmers, S., Wu, Y., Call, D. R., Labeit, S. & Granzier, H. Developmental control of titin isoform expression and passive stiffness in fetal and neonatal myocardium. *Circ. Res.* **94**, 505-513 (2004).
21 Hibberd, M. G. & Jewell, B. R. Calcium- and length-dependent force production in rat ventricular muscle. *J. Physiol.* **329**, 527-540 (1982).
22 Bird, S. D. *et al.* The human adult cardiomyocyte phenotype. *Cardiovasc. Res.* **58**, 423-434 (2003).
23 Lundy, S. D., Zhu, W. Z., Regnier, M. & Laflamme, M. A. Structural and functional maturation of cardiomyocytes derived from human pluripotent stem cells. *Stem Cells Dev.* **22**, 1991-2002 (2013).
24 Rodriguez, A. G., Han, S. J., Regnier, M. & Sniadecki, N. J. Substrate stiffness increases twitch power of neonatal cardiomyocytes in correlation with changes in myofibril structure and intracellular calcium. *Biophys. J.* **101**, 2455-2464 (2011).
25 Viskin, S. The QT interval: too long, too short or just right. *Heart Rhythm* **6**, 711-715 (2009).
26 McIntyre, H. & Fry, C. H. Abnormal action potential conduction in isolated human hypertrophied left ventricular myocardium. *J. Cardiovasc. Electrophysiol.* **8**, 887-894 (1997).
27 Pijnappels, D. A. *et al.* Progressive increase in conduction velocity across human mesenchymal stem cells is mediated by enhanced electrical coupling. *Cardiovasc. Res.* **72**, 282-291 (2006).

28 Lints, T. J., Parsons, L. M., Hartley, L., Lyons, I. & Harvey, R. P. Nkx-2.5: a novel murine homeobox gene expressed in early heart progenitor cells and their myogenic descendants. *Development* **119**, 419-431 (1993).
29 Zhang, H., Toyofuku, T., Kamei, J. & Hori, M. GATA-4 regulates cardiac morphogenesis through transactivation of the N-cadherin gene. *Biochem. Biophys. Res. Commun.* **312**, 1033-1038 (2003).
30 Boheler, K. R. *et al.* Differentiation of pluripotent embryonic stem cells into cardiomyocytes. *Circ. Res.* **91**, 189-201 (2002).
31 Pati, F. *et al.* Printing three-dimensional tissue analogues with decellularized extracellular matrix bioink. *Nat. Commun.* **5** (2014).
32 Stern, M. M. *et al.* The influence of extracellular matrix derived from skeletal muscle tissue on the proliferation and differentiation of myogenic progenitor cells ex vivo. *Biomaterials* **30**, 2393-2399 (2009).
33 Lin, P., Chan, W. C., Badylak, S. F. & Bhatia, S. N. Assessing porcine liver-derived biomatrix for hepatic tissue engineering. *Tissue Eng.* **10**, 1046-1053 (2004).
34 Oberwallner, B. *et al.* Human cardiac extracellular matrix supports myocardial lineage commitment of pluripotent stem cells. *Eur. J. Cardiothorac. Surg.* **47**, 416-425; discussion 425 (2015).
35 Zhao, J. Y. & Bass, K. D. Skeletal muscle regeneration by extracellular matrix biological scaffold: a case report. *J. Wound Care* **27**, S11-S14 (2018).
36 Wolf, M. T., Daly, K. A., Reing, J. E. & Badylak, S. F. Biologic scaffold composed of skeletal muscle extracellular matrix. *Biomaterials* **33**, 2916-2925 (2012).
37 Turner, N. J. *et al.* Xenogeneic extracellular matrix as an inductive scaffold for regeneration of a functioning musculotendinous junction. *Tissue Eng. Part A* **16**, 3309-3317 (2010).
38 Singelyn, J. M. *et al.* Catheter-deliverable hydrogel derived from decellularized ventricular extracellular matrix increases endogenous cardiomyocytes and preserves cardiac function post-myocardial infarction. *J. Am. Coll. Cardiol.* **59**, 751-763 (2012).
39 Seif-Naraghi, S. B. *et al.* Safety and efficacy of an injectable extracellular matrix hydrogel for treating myocardial infarction. *Sci. Transl. Med.* **5**, 173ra125 (2013).
40 Bhana, B. *et al.* Influence of substrate stiffness on the phenotype of heart cells. *Biotechnol. Bioeng.* **105**, 1148-1160 (2010).
41 Engler, A. J. *et al.* Embryonic cardiomyocytes beat best on a matrix with heart-like elasticity: scar-like rigidity inhibits beating. *J. Cell Sci.* **121**, 3794-3802 (2008).
42 Huebsch, N. *et al.* Harnessing traction-mediated manipulation of the cell/matrix interface to control stem-cell fate. *Nat. Mater.* **9**, 518-526 (2010).
43 Serena, E. *et al.* Soft substrates drive optimal differentiation of human healthy and dystrophic myotubes. *Integr. Biol.* **2**, 193-201 (2010).
44 Vogel, V. & Sheetz, M. Local force and geometry sensing regulate cell functions. *Nat. Rev. Mol. Cell Biol.* **7**, 265-275 (2006).
45 Boothe, S. D. *et al.* The effect of substrate stiffness on cardiomyocyte action potentials. *Cell Biochem. Biophys.* **74**, 527-535 (2016).

46 Kai, D., Prabhakaran, M. P., Jin, G. R. & Ramakrishna, S. Polypyrrole-contained electrospun conductive nanofibrous membranes for cardiac tissue engineering. *J Biomed. Mater. Res. A* **99a**, 376-385 (2011).
47 Shin, S. R. *et al.* Reduced graphene oxide-gelMA hybrid hydrogels as scaffolds for cardiac tissue engineering. *Small* **12**, 3677-3689 (2016).
48 Shin, S. R. *et al.* Carbon-nanotube-embedded hydrogel sheets for engineering cardiac constructs and bioactuators. *ACS Nano* **7**, 2369-2380 (2013).
49 Dvir, T. *et al.* Nanowired three-dimensional cardiac patches. *Nat. Nanotechnol.* **6**, 720-725 (2011).
50 Mihic, A. *et al.* A conductive polymer hydrogel supports cell electrical signaling and improves cardiac function after implantation into myocardial infarct. *Circulation* **132**, 772-784 (2015).
51 Tsui, J. H. *et al.* Conductive silk–polypyrrole composite scaffolds with bioinspired nanotopographic cues for cardiac tissue engineering. *J. Mater. Chem. B* **6**, 7185-7196 (2018).
52 Kitko, K. E. *et al.* Membrane cholesterol mediates the cellular effects of monolayer graphene substrates. *Nat. Commun.* **9**, 796 (2018).
53 Cherezov, V. *et al.* High-resolution crystal structure of an engineered human beta2-adrenergic G protein-coupled receptor. *Science* **318**, 1258-1265 (2007).
54 Clay, H. *et al.* Sphingosine 1-phosphate receptor-1 in cardiomyocytes is required for normal cardiac development. *Dev. Biol.* **418**, 157-165 (2016).
55 Balijepalli, R. C. *et al.* Kv11.1 (ERG1) K+ channels localize in cholesterol and sphingolipid enriched membranes and are modulated by membrane cholesterol. *Channels* **1**, 263-272 (2007).
56 Bastiaanse, E. M. L., Jongsma, H. J., van der Laarse, A. & Takens-Kwak, B. R. Heptanol-induced decrease in cardiac gap junctional conductance is mediated by a decrease in the fluidity of membranous cholesterol-rich domains. *J. Membr. Biol.* **136**, 135-145 (1993).
57 Bastiaanse, E. M., Hold, K. M. & Van der Laarse, A. The effect of membrane cholesterol content on ion transport processes in plasma membranes. *Cardiovasc. Res.* **33**, 272-283 (1997).
58 Broderick, R., Bialecki, R. & Tulenko, T. N. Cholesterol-induced changes in rabbit arterial smooth muscle sensitivity to adrenergic stimulation. *Am. J. Physiol.* **257**, H170-178 (1989).
59 Bialecki, R. A. & Tulenko, T. N. Excess membrane cholesterol alters calcium channels in arterial smooth muscle. *Am. J. Physiol.* **257**, C306-314 (1989).
60 Bastiaanse, E. M., Atsma, D. E., Kuijpers, M. M. & Van der Laarse, A. The effect of sarcolemmal cholesterol content on intracellular calcium ion concentration in cultured cardiomyocytes. *Arch. Biochem. Biophys.* **313**, 58-63 (1994).
61 van Vliet, P. *et al.* Hyperpolarization Induces Differentiation in human cardiomyocyte progenitor cells. *Stem Cell Rev. Rep.* **6**, 178-185 (2010).
62 Sun, X. & Nunes, S. S. Biowire platform for maturation of human pluripotent stem cell-derived cardiomyocytes. *Methods* **101**, 21-26 (2016).
63 Tiburcy, M. *et al.* Defined engineered human myocardium with advanced maturation for applications in heart failure modeling and repair. *Circulation* **135**, 1832-1847 (2017).

64 Zhang, D. *et al.* Tissue-engineered cardiac patch for advanced functional maturation of human ESC-derived cardiomyocytes. *Biomaterials* **34**, 5813-5820 (2013).
65 Ronaldson-Bouchard, K. *et al.* Advanced maturation of human cardiac tissue grown from pluripotent stem cells. *Nature* **556**, 239-243 (2018).
66 Tulloch, N. L. *et al.* Growth of engineered human myocardium with mechanical loading and vascular coculture. *Circ. Res.* **109**, 47-59 (2011).

Chapter 4. Bioprinted Human iPSC-derived Cardiac Tissues for Drug-Induced Cardiotoxicity Screening

4.1 Abstract

Human induced pluripotent stem cells (hiPSCs) offer tremendous potential for use in engineering human tissues for therapy and treatment development. However, differentiated cardiomyocytes are phenotypically immature, reducing assay reliability when translating *in vitro* results to clinical studies and precluding hiPSC-derived cardiac tissues from therapeutic use *in vivo*. To address this, we have developed hybrid hydrogels comprised of decellularized myocardial extracellular matrix (dECM) and reduced graphene oxide (rGO) to provide a more instructive microenvironment for proper cellular and tissue development. dECM-rGO hydrogels were utilized as bioinks to bioprint cardiac tissues in a high-throughput manner, and these tissues were utilized to assess the proarrhythmic potential of cisapride. The onset of action potential duration prolongation and beat interval irregularities was observed in dECM-rGO tissues at clinical doses, indicating that the enhanced maturation of these tissues due to the hybrid hydrogel bioink corresponded well with a capability to produce physiologically-relevant drug responses.

4.2 Introduction

The lack of physiologically-representative tissue models has hampered drug discovery and screening. Historically, drugs have been screened using non-cardiac single-cell assays or animal models that do not adequately recapitulate the biology of functional adult cardiomyocytes nor that of the human myocardium. Recent efforts have developed tissue engineering-based approaches in which cells are combined with scaffolds to create 3D tissue models for drug-screening that recapitulate the native tissue environment more accurately[1,2]. Despite the improved efficacy of these platforms, they present significant difficulties with translation to higher throughput (48, 96 well) modalities, and there is often considerable variability in tissue production from one culture to the next. Thus, bioprinting has emerged as a promising technology for micro-organogenesis, as it allows for the reproducible creation of structurally-defined tissue constructs in a high-throughput manner that is not readily achievable using other methods of 3D tissue engineering[3-5]. Therefore, the utilization of dECM-rGO hydrogel bioinks to bioprint functionally mature hiPSC-derived 3D cardiac tissues has the potential to improve assay reliability and better mimic the pharmacological responses of the native human myocardium.

4.3 Materials and Methods

4.3.1 Extracellular Matrix Solubilization and Hydrogel Formation

dECM-based pre-hydrogel solutions were generated by mixing lyophilized dECM and pepsin at a 10:1 mass ratio in 0.1 M HCl. rGO was also added at this stage for

dECM-rGO hydrogels. A 2% w/v dECM solution was used for all experiments in this study while the final concentration of the rGO component was varied from 0.1% - 0.3% w/v. Mixtures were stirred constantly until the dECM was completely solubilized and had formed a homogenous solution, at which point the pH was then brought up to 7.4 with 10 M NaOH. Finally, 10% of the final volume of 10X PBS or 10X RPMI 1640 (Sigma-Aldrich) was added to restore isotonic balance. Hydrogel pre-gel solutions were stored at 4ºC until use. Hydrogels were then formed by incubating pre-gel solutions at 37ºC for at least 12 h. The same solubilization and gelation method was used to generate control hydrogels composed of bovine collagen type I (Advanced BioMatrix). For generating dECM-TG hydrogels for stiffness controls, a 5% w/v solution of transglutaminase (TG; Modernist Pantry) was added to the dECM solution immediately prior to incubation at 37ºC.

4.3.2 Human Induced Pluripotent Stem Cell Culture and Cardiac Differentiation

UC 3-4 urine-derived human induced pluripotent stem cells (hiPSCs)[6,7] were cultured and differentiated using an adaptation of a previously published method of modulating Wnt/β-catenin signaling with small molecules[8]. In brief, hiPSCs were maintained on 1:60 diluted Matrigel-coated plates in mTeSR1 medium (STEMCELL Technologies) prior to induction. Induction is achieved by culturing the cells in RPMI 1640 medium (Invitrogen) supplemented with B-27 without insulin (Invitrogen) and 10 μM CHIR-99021 (Selleck Chemicals) for 18 hrs, after which the medium is replaced with fresh RPMI/B-27 without insulin for 48 hrs. The medium is then replaced with RPMI/B-27 without insulin supplemented with 5 μM IWP-4 (REPROCELL) and cells are cultured

for 48 hrs, after which the medium is once again replaced with fresh RPMI/B-27 without insulin for 48 hrs. Finally, medium is replaced with RPMI/B-27 with insulin (Invitrogen), and cultures are fed with fresh medium every other day. Spontaneously beating cells are typically observed 10-12 days after induction. Differentiation runs that produced hiPSC-cardiomyocyte (hiPSC-CM) purity of >92% as measured by flow cytometry after staining for cardiac troponin T (cTnT) were used for all experiments.

4.3.3 Human Stromal Cell Culture

HS-27A human bone marrow-derived stromal cells (ATCC) were cultured and maintained in high-glucose DMEM (Invitrogen) supplemented with 10% fetal bovine serum until used to generate tissues.

4.3.4 Cardiac Tissue Bioprinting

Tissues and support structures were bioprinted using a commercially-available dual-extruder pneumatic bioprinter (Allevi BioBot 1). Five pairs of polycaprolactone (PCL) posts 1 mm in diameter, 5 mm tall, and 10 mm apart were printed in each well of a standard 6-well plate. An approximately 2 mm thick layer of NOA 83H resin (Norland Optical Adhesives) was then deposited onto the bottom of each well and cured by a 30 min exposure to UV light. Plates containing anchored posts were then sterilized by immersion in 70% v/v ethanol and subsequent UV light exposure. Sacrificial wells 12 mm x 5 mm x 1 mm (length x width x depth) were then printed around each post pair using 40% w/w Pluronic F-127, followed by approximately 50 µL of cell-laden hydrogel bioinks with the same cell densities as used in the EHT platform. Completed plates

were then incubated at 37°C and 5% CO_2 for approximately 60 min, after which 5 mL of RPMI/B-27 with insulin (supplemented with Y-27632 dihydrochloride ROCK inhibitor and 1% penicillin/streptomycin) was added to each well. After 24 hrs, the media was replaced with fresh RPMI/B-27 with insulin and media changes were conducted every other day until tissues were used for drug screening. Optimized printing parameters for each component of the design is provided in **Table 4.1**.

Table 4.1. Printing parameters optimized for bioprinting microphysiological systems using dECM-based bioinks and a two-post passive tension design with a sacrificial support well.

Material	Pressure (psi)	Temp. (°C)	Needle Gauge
PCL	100	100	30
Pluronic F-127	75-85	25	30
Bioink	3-5	25	25
NOA 83H	1-3	25	25

4.3.5 *In Situ* Tissue Electrophysiological Function Measurements and Analysis

Bioprinted cardiac tissue depolarization characteristics were assessed using the FluoVolt (Invitrogen) fluorescent potentiometric dye. Tissues were washed with warm PBS before being incubated in medium containing a 1000X dilution of stock FluoVolt for 1 hr at 37°C, after which tissues were washed twice with warm Tyrode's buffer and placed in fresh Tyrode's. Tissues were then imaged using standard FITC settings on a widefield epi-fluorescence microscope with a high-speed color CMOS camera (Hamamatsu ORCA-Flash4.0), with videos taken at 66 FPS and 2X magnification. Tissues were not paced and fluorescence intensity from the FluoVolt dye was quantified using NIS Elements. APD_{90} and values were then calculated using a custom MATLAB script[9].

4.3.6 Assessment of Predictive Cardiotoxicity with Cisapride

Cardiac tissues were bioprinted using dECM and dECM-rGO bioinks and cultured for 14 and 35 days. At these time points, tissues were washed with warm PBS before being incubated in medium containing a 1000X dilution of stock FluoVolt for 1 hr at 37°C, after which tissues were washed twice with warm Tyrode's buffer and incubated in Tyrode's containing 0.01, 0.1, 1, 5, 10, 50, 100, and 1000 nM cisapride (Sigma-Aldrich) dissolved in dimethyl sulfoxide (DMSO) for 45 mins. A group of tissues were also incubated in Tyrode's containing no cisapride, but an equivalent volume of DMSO (1 µL DMSO/mL Tyrode's). Functional response of these tissues to administered drug was assessed using FluoVolt dye in conjunction with live-tissue imaging as described above. Change in beat interval (ΔBI) was determined by measuring that duration of elapsed time between individual beats (the beat interval) and calculating the difference in this interval from one beat to the next. APD_{90} values were calculated as described above. Best-fit dose response curves were calculated using GraphPad Prism software. Drug concentration values were first transformed to a log scale and APD_{90} or ΔBI values were normalized such that the lowest value was set at 0% and the largest value at 100%. Finally, the normalized data was fit to a non-linear dose response curve using a least squares fit.

4.3.7 Statistical Analyses

Unless otherwise noted, all quantitative data is presented as means ± standard error. A Student's *t*-test was used to compare data sets looking at only two variables. In all presented analyses, $p < 0.05$ was considered significant.

4.4 Results

4.4.1 Bioprinting Cardiac Microphysiological Tissues Using dECM-rGO Bioinks

As noted previously, dECM and dECM-rGO hydrogels exhibited shear-thinning behavior in response to increases in strain rate. This type of viscoelastic property makes these hydrogels well-suited to applications such as bioprinting where it is desirable to have a material that can be easily extruded, while maintaining the capacity to quickly reform and hold a structure post-extrusion. Using a dual-extruder bioprinter, a multi-material design was developed in which hydrogels could be utilized as a bioink for generating 3D cardiac tissues in a high-throughput manner while taking advantage of the beneficial effects on tissue maturation that dECM-rGO could offer (**Figure 4.1**). In this design, post pairs comprised of polycaprolactone (PCL) were printed to serve as anchor points for tissues and to induce anisotropic cellular alignment, while Pluronic F-127 was used to print temporary wells around these posts to aid in tissue formation during the first 24 hrs.

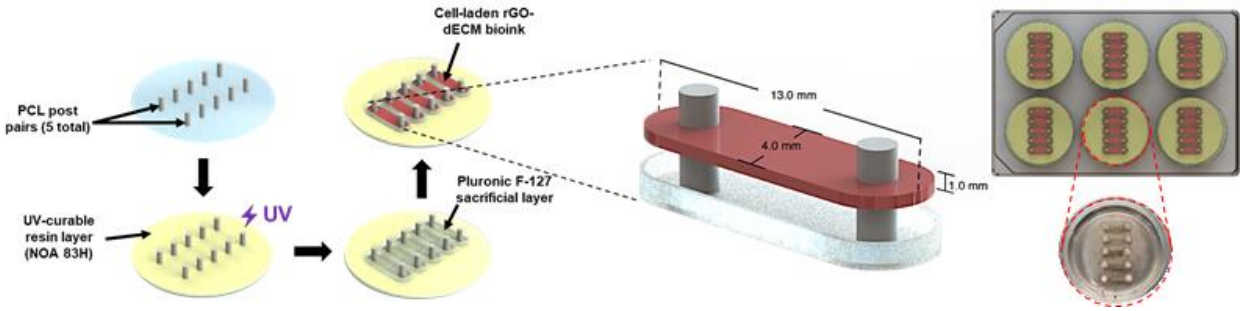

Figure 4.1. A modular bioprinted platform for the high-throughput generation of human cardiac tissues. Schematic representation of the developed bioprinted platform. Post pairs comprised of PCL are printed and anchored into place with a thin layer of photocured NOA 83H. A temporary well of Pluronic F-127 is printed around each post pair before cell-laden dECM or dECM-rGO bioink is printed into each well. As an example, a 5 tissue-per-well in a 6 well plate setup is demonstrated.

4.4.2 Tissues Printed with dECM-rGO Bioinks Generated Physiologically Accurate Responses to Cisapride

Using our designed platform, cardiac tissues were printed with dECM and dECM-rGO bioinks and cultured for 14 and 35 days before being subjected to a dose response study with cisapride. Cisapride, a potent hERG channel blocker that induces QT interval prolongation, was selected for this proof of concept demonstration due to the fact that its ability to cause potentially lethal Torsade de Pointes (TdP) in humans at clinical doses was not detected using conventional preclinical screening assays and was then subsequently withdrawn from market[10-12]. Fluorescent imaging of FluoVolt dye was once again used to assess cisapride's impact on tissue APD_{90} length and beat interval regularity across a large range of concentrations. At Day 14, it was found that dECM and dECM-rGO tissues responded significantly differently to increasing cisapride concentrations (**Figure 4.2a**). While both tissue types exhibited APD_{90} prolongation and an increase in ΔBI, the IC_{50} values differed by an order of magnitude (**Figure 4.2b**). dECM-rGO tissues responded physiologically to cisapride, with IC_{50} values (APD_{90}: 2.51 ± 1.32 nM; ΔBI: 8.63 ± 1.17 nM) very similar to cisapride's effective therapeutic plasma concentration (ETPC) of 2.6 – 4.9 nM[13]. dECM tissues, on the other hand, had IC_{50} values that were much higher at 61.77 ± 1.36 nM and 73.43 ± 1.37 nM for APD_{90} and ΔBI, respectively. Surprisingly, there was no significant difference in drug response between the dECM and dECM-rGO tissues at Day 35, with best-fit dose response curves for percent change in APD_{90} and ΔBI identical between the two tissue types (**Figure 4.2c**). However, IC_{50} values for both dECM (APD_{90}: 1.96 ± 1.33 nM; ΔBI: 7.33 ± 1.16 nM) and dECM-rGO tissues (APD_{90}: 1.78 ± 1.40 nM; ΔBI: 3.14 ± 1.27 nM) were

representative of native cardiac tissue response when exposed to cisapride (**Figure 4.2d**).

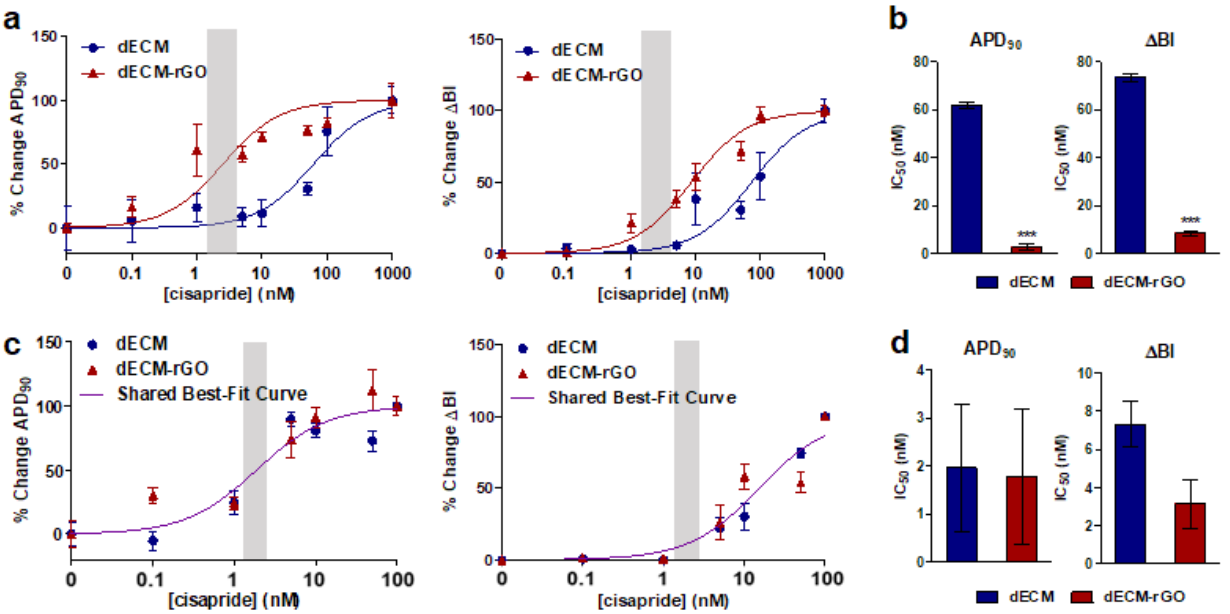

Figure 4.2. Response of bioprinted hiPSC-derived cardiac tissues to cisapride. (a) Dose-response curves for percent change in APD_{90} and ΔBI in response to varying concentrations of cisapride in tissues cultured for 14 days. (b) Quantification of IC_{50} values derived from both metrics show that dECM-rGO tissues respond in a physiologically-representative manner compared to dECM tissues at this time point. Gray boxes indicate reported ETPC for cisapride. ***$p < 0.001$ (Student's *t*-test, n = 10). (c) Bioprinted tissues cultured for 35 days showed no significant difference in their dose-response curves for percent change in APD_{90} and ΔBI, and (d) this is reflected in the comparable IC_{50} values for both metrics. Gray boxes indicate reported ETPC range for cisapride.

4.5 Discussion

A significant limitation of current preclinical screening techniques for drug-induced cardiotoxicity is their inability to provide accurate predictability, leading to incidences of false positives or negatives, increases in drug development costs, and unnecessary risk to patients. The reliance on animal models and non-human cell lines has contributed to this problem due to mismatches in pharmacokinetics and physiology between species[14], so a shift towards the utilization of 3D humanized *in vitro* tissue models is a promising

first step. However, not only do these approaches suffer from the aforementioned issues with phenotypic immaturity, but they are also hampered by low throughput and fabrication variability. The emergence of bioprinting and additive manufacturing as tissue fabrication methods offers a potential solution to these drawbacks as these techniques allow for the precise deposition and patterning of multiple biomaterials in a reproducible and automated fashion[3]. In the design developed in this study each post pair and well was a single defined unit, and this imparted increased modularity and versatility compared to more conventional grid designs[15,16] as it could be adapted for a variety of layouts to increase or decrease desired experimental throughput. For example, while a 5 tissue per well of a 6-well plate format was used, the same design could be used to print a single tissue per well in a 24-well or 48-well plate. When used with dECM-rGO bioinks, bioprinting was therefore able to produce larger numbers of more mature cardiac tissues in less time and in a format that still allowed for conventional image-based analysis of changes in electrophysiological function. While current hardware limitations do not allow for a level of throughput commensurate with existing systems such as microelectrode arrays (MEAs)[17], the ability to utilize 3D tissues instead of 2D monolayers is still an advantageous aspect of this approach.

Based on the vast difference in expression of the hERG channel coding gene *KCNH2* between dECM and dECM-rGO tissues that was observed in the work presented in Chapter 3, it is perhaps unsurprising that even after only 14 days of culture, cisapride induced abnormal APD_{90} prolongation and beat intervals in dECM-rGO tissues at physiological concentrations. In comparison to previously reported drug screening platforms based on hiPSC-derived cardiomyocytes[17,18], whole animal

models[19], and *in silico* simulations[20], our platform was able to produce IC_{50} values for cisapride or similar hERG channel blockers that were within the same order of magnitude as ETPC. What was surprising, however, was the indistinguishable difference in response of the dECM and dECM-rGO tissues to cisapride after 35 days of culture despite there still being a significant gap in *KCNH2* expression at this time point. This result could indicate that as time progressed, dECM scaffolds were able to induce further development of other ion channels that were not examined in this study and that these channels contributed to an overall maturation state that allowed these tissues to behave physiologically to this particular drug. In fact, other studies have suggested that the onset of TdP cannot be solely explained by the blockade of a single current[21]. However, when combined with the collected twitch force data, the results of this cisapride assay could also serve as further evidence of the role dECM-rGO hydrogels play in accelerating the maturation of engineered cardiac tissues to the point that even though the developmental stage has not yet reached a fully adult-like phenotype, these tissues are still mature enough to produce useful data in drug screening and disease modeling applications. To the end user, this could potentially provide significant advantages to cost and throughput, as tissues would only need to be maintained for a shorter duration of time before use.

4.6 References

1 Hansen, A. *et al.* Development of a drug screening platform based on engineered heart tissue. *Circ. Res.* **107**, 35-44 (2010).

2 Nunes, S. S. *et al.* Biowire: a platform for maturation of human pluripotent stem cell-derived cardiomyocytes. *Nat. Methods* **10**, 781-787 (2013).

3 Duan, B. State-of-the-Art Review of 3D bioprinting for cardiovascular tissue engineering. *Ann. Biomed. Eng.* **45**, 195-209 (2017).

4 Lee, J. S. *et al.* 3D printing of composite tissue with complex shape applied to ear regeneration. *Biofabrication* **6**, 024103 (2014).

5 Duan, B., Kapetanovic, E., Hockaday, L. A. & Butcher, J. T. Three-dimensional printed trileaflet valve conduits using biological hydrogels and human valve interstitial cells. *Acta Biomater.* **10**, 1836-1846 (2014).

6 Macadangdang, J. *et al.* Nanopatterned human iPSC-based model of a dystrophin-null cardiomyopathic phenotype. *Cell. Mol. Bioeng.* **8**, 320-332 (2015).

7 Guan, X. *et al.* Dystrophin-deficient cardiomyocytes derived from human urine: New biologic reagents for drug discovery. *Stem Cell Res.* **12**, 467-480 (2014).

8 Lian, X. J. *et al.* Directed cardiomyocyte differentiation from human pluripotent stem cells by modulating Wnt/beta-catenin signaling under fully defined conditions. *Nat. Protoc.* **8**, 162-175 (2013).

9 Leonard, A. *et al.* Afterload promotes maturation of human induced pluripotent stem cell derived cardiomyocytes in engineered heart tissues. *J. Mol. Cell. Cardiol.* **118**, 147-158 (2018).

10 Darpö, B. Spectrum of drugs prolonging QT interval and the incidence of torsades de pointes. *Eur. Heart J. Suppl.* **3**, K70-K80 (2001).

11 Zipes, D. P., Barbey, J. T. & Lazzara, R. Review of spontaneous adverse event reports of serious ventricular arrhythmias, QT prolongation, syncope, and sudden death in patients treated with cisapride. *Circulation* **100**, 308-308 (1999).

12 Enger, C., Cali, C. & Walker, A. M. Serious ventricular arrhythmias among users of cisapride and other QT-prolonging agents in the United States. *Pharmacoepidemiol. Drug Saf.* **11**, 477-486 (2002).

13 Redfern, W. S. *et al.* Relationships between preclinical cardiac electrophysiology, clinical QT interval prolongation and torsade de pointes for a broad range of drugs: evidence for a provisional safety margin in drug development. *Cardiovasc. Res.* **58**, 32-45 (2003).

14 Fine, B. & Vunjak-Novakovic, G. Shortcomings of animal models and the rise of engineered human cardiac tissue. *ACS Biomater. Sci. Eng.* **3**, 1884-1897 (2017).

15 Pati, F. *et al.* Printing three-dimensional tissue analogues with decellularized extracellular matrix bioink. *Nat. Commun.* **5** (2014).

16 Zhu, K. *et al.* Gold nanocomposite bioink for printing 3D cardiac constructs. *Adv. Funct. Mater.* **27** (2017).

17 Mathur, A. *et al.* Human iPSC-based cardiac microphysiological system for drug screening applications. *Sci. Rep.* **5**, 8883 (2015).

18 Gilchrist, K. H., Lewis, G. F., Gay, E. A., Sellgren, K. L. & Grego, S. High-throughput cardiac safety evaluation and multi-parameter arrhythmia profiling of

cardiomyocytes using microelectrode arrays. *Toxicol. Appl. Pharmacol.* **288**, 249-257 (2015).

19 Hauser, D. S., Stade, M., Schmidt, A. & Hanauer, G. Cardiovascular parameters in anaesthetized guinea pigs: a safety pharmacology screening model. *J. Pharmacol. Toxicol. Methods* **52**, 106-114 (2005).

20 Okada, J. *et al.* Screening system for drug-induced arrhythmogenic risk combining a patch clamp and heart simulator. *Sci. Adv.* **1**, e1400142 (2015).

21 Champeroux, P. *et al.* Prediction of the risk of Torsade de Pointes using the model of isolated canine Purkinje fibres. *Br. J. Pharmacol.* **144**, 376-385 (2005).

Chapter 5. Conclusions and Future Directions

The research presented in this dissertation illustrate the synergistic impact that the microenvironmental cues present in dECM-rGO hydrogels had on promoting the functional maturation of engineered cardiac microphysiological systems. Not only did this biomaterial induce significant improvements in several metrics of cardiac contractile and electrophysiological function, these developmental gains were translated into clinically-relevant physiological responses suitable for downstream applications. Furthermore, the tunability of these hybrid hydrogel's properties and demonstrated applicability as a bioink for 3D bioprinting enable it to be a versatile tool for answering multiple biological questions. The ease in which two materials with largely disparate characteristics could be combined into a single composite demonstrates the potential for other adjuncts that could be incorporated into these hydrogels, such as soluble or tethered factors or other synthetic nanomaterials[1], that could be used to further enhance overall material functionality.

Work is currently underway to utilize dECM-rGO hybrid hydrogels as a scaffold for engineering human cardiac tissue models to study the effects of microgravity on cardiac function and genomic profile. With current plans for manned missions beyond Earth orbit, the need to better understand the effects of long duration spaceflight on various bodily systems, as well as how to prevent and treat them, is becoming increasingly important. For example, microgravity has been shown to upregulate the expression of mitochondrial metabolism genes, such as malate dehydrogenase, in rat cardiac muscle[2]. Another study in a rat model demonstrated that simulated microgravity

promoted the expression of a unique isoform of cTnI[3]. Simulated microgravity has also been shown in rat cardiomyocytes to alter nuclear localization of NFκB, a protein implicated in the cellular responses to oxidative stress[4]. However, the majority of studies to date on cardiomyocyte responses to microgravity have been carried out with rodents or chick embryos, and as highlighted previously, this is problematic since animal-based models may not be adequately representative of human cardiac tissues due to interspecies differences in cardiac function and gene expression. The so-called "Twins Study", in which the impact of prolonged spaceflight was investigated by comparing an astronaut's physiology with his Earth-bound twin's, offers one of the first comprehensive investigations on microgravity's effect on human health[5]. Unfortunately, these types of studies are logistically difficult, expensive, and are limited by small sample size. By harnessing the ability to generate more adult-like phenotypes with the technology developed in this dissertation, this study will be the first to employ an hiPSC-based 3D microphysiological platform to investigate the effects of microgravity on human heart tissue structure, function, and gene expression.

Another promising potential application of the functionally mature hiPSC-derived cardiac tissues described in this dissertation is the modeling of inherited cardiomyopathies such as Duchenne muscular dystrophy (DMD). DMD is a X-linked neuromuscular disorder that affects 1 in every 3500 males and is caused by frameshift mutations in the dystrophin gene that result in the expression of a truncated, nonfunctional dystrophin protein. With technological advances improving palliative and respiratory care for DMD patients, dilated cardiomyopathy caused by dystrophin deficiencies has now become the leading cause of death[6,7]. This fact, coupled with the

finding that dilated cardiomyopathies manifest even in female carriers that do not exhibit signs of skeletal muscle degeneration[8,9], has led to an urgent need for the development of novel therapies and treatment modalities to help improve patient quality of life and overall lifespan. While the *mdx* mouse model of DMD has provided valuable insights into the disease, it is an imperfect model for studying dystrophy-induced cardiac dysfunction due to slow development of cardiac dysfunction and presentation of a less severe phenotype than that observed in humans[10]. A prime example of this discrepancy in physiological response is the withdrawal of sildenafil from clinical trials due to its exacerbation of symptoms in humans despite achieving beneficial results in *mdx* mice[11]. In response to this, efforts have been made to develop "disease-in-a-dish" models that utilize cardiomyocytes derived from DMD patient-isolated or dystrophin knock-out hiPSCs[12-14]. While initial results with these platforms have been promising, many still fall short of truly replicating the disease phenotype seen in patients. In one study, although distinct morphological differences were seen between healthy and dystrophic cardiomyocytes, functional characteristics between cell types were either not significantly different or did not reflect known clinical observations[15]. This suggests that improved methods of enhancing overall cardiomyocyte maturation and functional phenotype are required to better generate adequate disease models *in vitro*.

5.1 References

1 Tomas, H., Alves, C. S. & Rodrigues, J. Laponite(R): A key nanoplatform for biomedical applications? *Nanomedicine* **14**, 2407-2420 (2018).

2 Connor, M. K. & Hood, D. A. Effect of microgravity on the expression of mitochondrial enzymes in rat cardiac and skeletal muscles. *J. Appl. Physiol.* **84**, 593-598 (1998).

3 Yu, Z. B., Zhang, L. F. & Jin, J. P. A proteolytic NH2-terminal truncation of cardiac troponin I that is up-regulated in simulated microgravity. *J. Biol. Chem.* **276**, 15753-15760 (2001).

4 Kwon, O., Tranter, M., Jones, W. K., Sankovic, J. M. & Banerjee, R. K. Differential translocation of nuclear factor-kappaB in a cardiac muscle cell line under gravitational changes. *J. Biomech. Eng.* **131** (2009).

5 Garrett-Bakelman, F. E. *et al.* The NASA Twins Study: a multidimensional analysis of a year-long human spaceflight. *Science* **364** (2019).

6 Kaspar, R. W., Allen, H. D. & Montanaro, F. Current understanding and management of dilated cardiomyopathy in Duchenne and Becker muscular dystrophy. *J. Am. Acad. Nurse Pract.* **21**, 241-249 (2009).

7 Judge, D. P., Kass, D. A., Thompson, W. R. & Wagner, K. R. Pathophysiology and therapy of cardiac dysfunction in Duchenne muscular dystrophy. *Am. J. Cardiovasc. Drugs* **11**, 287-294 (2011).

8 Politano, L. *et al.* Development of cardiomyopathy in female carriers of Duchenne and Becker muscular dystrophies. *JAMA* **275**, 1335-1338 (1996).

9 Kinoshita, H. *et al.* A carrier of Duchenne muscular dystrophy with dilated cardiomyopathy but no skeletal muscle symptom. *Brain Dev.* **17**, 202-205 (1995).

10 Mourkioti, F. *et al.* Role of telomere dysfunction in cardiac failure in Duchenne muscular dystrophy. *Nat. Cell Biol.* **15**, 895-904 (2013).

11 Leung, D. G. *et al.* Sildenafil does not improve cardiomyopathy in Duchenne/Becker muscular dystrophy. *Ann. Neurol.* **76**, 541-549 (2014).

12 Guan, X. *et al.* Dystrophin-deficient cardiomyocytes derived from human urine: New biologic reagents for drug discovery. *Stem Cell Res.* **12**, 467-480 (2014).

13 Lin, B. *et al.* Modeling and study of the mechanism of dilated cardiomyopathy using induced pluripotent stem cells derived from individuals with Duchenne muscular dystrophy. *Dis. Model. Mech.* **8**, 457-466 (2015).

14 Young, C. S. *et al.* A single CRISPR-Cas9 deletion strategy that targets the majority of DMD patients restores dystrophin function in hiPSC-derived muscle cells. *Cell Stem Cell* **18**, 533-540 (2016).

15 Macadangdang, J. *et al.* Nanopatterned human iPSC-based model of a dystrophin-null cardiomyopathic phenotype. *Cell. Mol. Bioeng.* **8**, 320-332 (2015).

Appendix A. Description of Supplementary Video Files

Supplementary Video 1. Representative bright-field video of a beating hiPSC-derived EHT generated with dECM.

Supplementary Video 2. Representative bright-field video of a beating hiPSC-derived EHT generated with dECM-rGO.

Appendix B. Conductive Silk-Polypyrrole Composite Scaffolds with Bioinspired Nanotopographic Cues for Cardiac Tissue Engineering

This appendix has been published in the following first-authored manuscript:

J.H. Tsui, N.A. Ostrovsky-Snider, D.M.P. Yama, J. Donohue, J.S. Choi, R. Chavanachat, J.D. Larson, A.R. Murphy, D.H. Kim. Conductive silk-polypyrrole composite scaffolds with bioinspired nanotopographic cues for cardiac tissue engineering. *J. Mater. Chem. B.* **6**, 7185-7196 (2018).

B.1 Abstract

We report on the development of bioinspired cardiac scaffolds made from electroconductive acid-modified silk fibroin-poly(pyrrole) (AMSF+PPy) substrates patterned with nanoscale ridges and grooves reminiscent of native myocardial extracellular matrix (ECM) topography to enhance the structural and functional properties of cultured human pluripotent stem cells (hPSC)-derived cardiomyocytes. Nanopattern fidelity was maintained throughout the fabrication and functionalization processes, and no loss in conductive behavior occurred due to the presence of the nanotopographical features. AMSF+PPy substrates were biocompatible and stable, maintaining high cell viability over a 21-day culture period while displaying no signs of PPy delamination. The presence of anisotropic topographical cues led to increased cellular organization and sarcomere development, and electroconductive cues promoted a significant improvement in the expression and polarization of connexin 43 (Cx43), a critical regulator of cell-cell electrical coupling. The combination of biomimetic topography and electroconductivity also increased the expression of genes that encode

key proteins involved in regulating the contractile and electrophysiological function of mature human cardiac tissue.

B.2 Introduction

In recent years there has been an increasing number of studies in which conductive materials are applied as scaffolds for engineering a variety of tissue types[1]. Specifically, materials such as graphene[2,3], carbon nanotubes[4-6], gold[7-9], and polyaniline (PANi)[10-12], have all been utilized as promising candidates for cardiac tissue engineering. Polypyrrole (PPy) in particular has been studied extensively due to its ease of synthesis, relatively high conductivity under physiological conditions, ability to be chemically modified to adjust its electrical and biological activity, and well-characterized biocompatibility *in vitro* and *in vivo*[13-16]. While the brittleness of PPy typically precludes its use as a cell-culture substrate, it can be incorporated within a more pliable polymer to form a composite material better suited for biomedical applications[17-19]. For example, previous work has demonstrated the ability to integrate PPy with silk fibroin[20-22], prized for its biocompatibility, robust mechanical properties, low cost, versatility, and biodegradability[23,24].

It has been established that cell behavior within tissues is partially regulated by their surrounding extracellular matrix (ECM) *via* both biochemical factors and physical interactions with ECM architecture[25-27]. Ultrastructural analyses of myocardial ECM indicate that it is comprised of highly-aligned collagen fiber bundles that range in size from a few hundred nanometers to a couple microns in diameter, and that this distinct feature plays a significant role in driving the organization and function of

cardiomyocytes, and the organ as a whole[28-31]. Specifically, the structural definition of the heart on multiple scales induces the directional propagation of forces and action potentials that then enable synchronous and efficient contractions[32]. Inspired by these findings, substrates with anisotropic topography have been utilized to promote not only the polarity and structural development of cardiomyocytes, but their overall maturation as well[28,33,34].

Human pluripotent stem cell-derived cardiomyocytes (hPSC-CMs) offer tremendous potential for the generation of human cardiac tissues for *in vitro* drug-screening and disease modeling applications, as well as for *in vivo* therapies such as those for myocardial infarcts[35-38]. However, one of the greatest limitations in using these cells is that they are often phenotypically deficient post-differentiation, resulting in tissues that are not sufficiently representative of the adult human myocardium[39,40]. A primary cause of this observed shortcoming in cultured hPSC-CMs is that conventional cell culture platforms do not fully recapitulate the variety of cues cardiomyocytes are exposed to in their native tissue niche, and the development of new methods that incorporate multiple tissue-specific stimuli remains challenging.

In this study, we developed a facile approach for enhancing the development of hPSC-derived cardiac tissues, in which silk fibroin substrates were first patterned with anisotropic nanotopography that mimicked myocardial ECM. These corrugated silk substrates were subsequently functionalized sulfonic acid groups to facilitate integration of PPy, which imparted electroconductive properties. Nanopattern fidelity was maintained throughout the substrate fabrication process, and the presence of topographical features had no impact on substrate conductivity. It was also found that

the nanotopographical and electroconductive cues acted synergistically to promote both tissue organization and the maturation of the contractile and electrical signal conduction capabilities of cultured cardiomyocytes. These results further highlight the benefits of recapitulating the myocardial cell niche *in vitro* such that physiologically representative cardiac tissues for downstream applications can be feasibly generated.

B.3 Materials and Methods

B.3.1 Preparation of Aqueous Silk Fibroin Solutions

Bombyx mori silkworm cocoons were purchased from Oregon Silkworms in Bend, OR. Cocoons were shredded then degummed by boiling in Na_2CO_3 (20 mM, 4 L per 10 g of shredded cocoons) solution for 60 min, then washed in boiling DI water for 15 min followed by three 15-min washes in room temperature DI water. The fibroin fibers were then allowed to dry overnight in a fume hood. The dry fibers were placed in a beaker and sufficient LiBr (9.3 M) solution was added to make a 20% w/v solution, which was placed in a 60°C oven until fibers were fully dissolved. This solution was placed in dialysis tubing (Fisherbrand, 3.5 kDa MWCO) and dialyzed for 24 h against nanopure water that was changed 4 times. This solution was then dialyzed against dilute HCl (1 mM) until it reached pH 7. The solution was concentrated by laying the dialysis bag on dry polyethylene glycol (10k MW) until it reached the desired concentration (6-8% w/v) at which point it was passed through a syringe filter (Millex-CV 5.00 µm), and then stored at 4°C.

B.3.2 Silk Fibroin Substrate Fabrication

Master molds used to generate nanopatterned silk fibroin films were fabricated using a modification of capillary force lithography (CFL) techniques that have been previously described[28,33,41,42]. Briefly, a nanopatterned silicon wafer was coated in polyurethane acrylate (PUA; Minuta Technology, Korea), and a 75 μm thick sheet of polyethylene terephthalate (PET; SKC Inc., Korea) was then pressed down onto the silicon wafer. Ultraviolet (UV) light (λ = 250-400 nm) was then applied for 30 s (dose = 100 mJ/cm^2) to give an initial curing. This nanopatterned PUA master mold was then peeled from the silicon wafer and placed under UV overnight to fully cure. A polydimethylsiloxane (PDMS; Sylgard 184, Dow Corning, MI, USA) mold was then produced by pouring PDMS over the PUA master mold and left to cure over a period of 48 h at room temperature before the PUA master and PDMS were subsequently peeled apart.

B.3.3 Acid Modification of Silk Substrates

Ethanol-cured silk fibroin films were adhered to a Petri dish by applying polyimide tape to their perimeter, taking care to place the corrugated side facing upward. The film was then immersed in borate buffer (20 mL, 100 mM sodium borate, 123 mM sodium chloride, pH 9.5) and placed on ice. Sulfanilic acid (85 mg) and *p*-toluene sulfonic acid (*p*-TSA, 380 mg) were dissolved in nanopure water (5 mL) and placed on ice for 10 min. Sodium nitrite (4 M, 160 μL) solution was added to the acid mixture and returned to the ice for 15 min to allow the diazonium salt to form. The solution containing the diazonium salt was then pipetted into the silk solution, mixed and allowed to react on ice for 40 min. The reaction solution was discarded and the silk film was rinsed 3 times with

nanopure water. Films with this treatment are referred to as acid-modified silk films (AMSF). Prepared silk fibroin solution was then poured into the PDMS mold and left to dry overnight at room temperature before the resulting nanopatterned silk film was peeled from the PDMS mold and soaked in 70% ethanol overnight. Flat silk fibroin substrates were fabricated using an identical process, but with the use of an unpatterned PDMS mold instead.

B.3.4 Deposition of Poly(pyrrole) onto Acid-Modified Silk Substrates

Acid modified films that were still adhered to the Petri dishes were immersed in *p*-TSA (5 mM) and pyrrole (50 mM) solution. Immediately after the addition of pyrrole, $FeCl_3$ was added to a final concentration of 15 mM and was allowed to polymerize at room temperature for 2 h. Following polymerization, the solution was decanted and the films were rinsed thoroughly with nanopure water. The films were sonicated in nanopure water for 30 s, and then cut away from the Petri dish and stored in ethanol (70% v/v) to ensure sterility. These films are referred to as AMSF+PPy in the remaining text.

B.3.5 Scanning Electron Microscopy

Substrates were sputter-coated with Au-Pd for 60 s. High resolution imaging of substrate surfaces was achieved using a scanning electron microscope (Sirion XL30, FEI, OR, USA) and an acceleration voltage of 5 kV.

B.3.6 Atomic Force Microscopy

Topographical profiles of fabricated substrates were obtained using an atomic force microscope (Dimension ICON, Bruker, MA, USA). Tapping mode was used with 1 kHz of scan rate and a 512 x 512 scanning resolution over a 10 μm x 10 μm area of each sample. Measurement of RMS surface roughness was completed using Gwyddion (Czech Metrology Institute, CZ) data analysis software.

B.3.7 I-V Curve Measurements

I-V curves were recorded using a parameter analyzer (Keithley 4200-SCS, Tektronix, OR, USA) under the conditions of a direct current (DC) voltage sweep ranging from -5 V to 5 V.

B.3.8 Measurement of Substrate Resistivity

Sheet resistivity of substrates was measured with a four-point resistivity probe (S-304-2, Lucas Labs, CA, USA) mounted with a Signatone SP4-40045TBY tip and powered by a Keithley 2400 Sourcemeter. Values were calculated using the equation $R_S = 4.532(\frac{V}{I})$, where V (volts) is the voltage measured across the two inner probe electrodes, I (amperes) is the current passed between the two outer probe electrodes, and R_S (Ω/sq) is the sheet resistivity.

B.3.9 Differentiation of hESC-Derived Cardiomyocytes

Cardiomyocyte differentiation from human embryonic stem cells (hESCs) was accomplished using a previously described and established serum-free directed differentiation protocol[43]. Undifferentiated RUES-2 hESCs (Rockefeller University, NY, USA) were maintained and expanded on Matrigel-coated culture plates in feeder-free mouse embryonic fibroblast-conditioned media supplemented with 4 ng/mL basic fibroblast growth factor (bFGF; R&D Systems, MN, USA). To induce differentiation of RUES-2 monolayers, the conditioned media was supplemented with 1 μM of the Wnt agonist Chiron 99021 (Tocris Bioscience, MN, USA) for 1 d. This was followed by a change in medium to RPMI 1640/B27 (minus insulin) (Invitrogen, MA, USA) supplemented with 100 ng/mL activin A (R&D Systems). After 18 h of culture, the cells were fed with RPMI/B27 (minus insulin) supplemented with 5 ng/mL bone morphogenetic protein-4 (BMP-4; R&D Systems) and 1 μM Chiron 99021 for 48 h. Cells were then provided with fresh RPMI/B27 (minus insulin) supplemented with 1 μM XAV 939 (Tocris Bioscience), a Wnt antagonist, for 48 h. Seven days after induction, cells were maintained in RPMI/B27 (plus insulin) medium for an additional 7 d before dissociation for flow cytometry analysis. Only differentiation runs that produced a population of cells that were at least 90% cardiac troponin T (cTnT)-positive were used for the experiments described in this study.

B.3.10 Cell Culture

Prior to cell seeding, fabricated AMSF substrates were incubated at 37 ºC in a 60 µg/mL solution of human fibronectin (Invitrogen) for 12 h. For the formation of confluent monolayers, stem cell-derived cardiomyocytes were seeded onto substrates at a density of 2.5 x 10^5 cells/cm^2, while a seeding density of 2.5 x 10^4 cells/cm^2 was used for single-cell imaging experiments. Cultures were maintained in RPMI/B27 (plus insulin) medium that was replaced every other day for a total of 21 d.

B.3.11 Assessment of Biocompatibility

Stem cell-derived cardiomyocytes were cultured on flat and patterned AMSF and AMSF+PPy substrates, as well as on a standard tissue culture polystyrene (TCPS) control for 21 d. Cells were seeded onto substrates at a density of 2.5 x 10^5 cells/cm^2. Cell viability was then determined using a MTS colorimetric assay (CellTiter96, Promega, WI, USA) according to the manufacturer's guidelines. Briefly, 20 µL of assay solution reagent was pipetted into a clear-bottom 96-well plate containing the samples and 100 µL of culture medium. The plate was then incubated at 37 °C for 4 h before recording absorbance values at λ = 490 nm with a plate reader.

B.3.12 Immunostaining and Confocal Fluorescence Microscopy

Cultured cells were fixed with 4% w/v paraformaldehyde in PBS for 10 min at room temperature and were then permeabilized with 0.1% w/v Triton-X 100 (Sigma-Aldrich, MO, USA) in PBS for 5 min at room temperature. For analysis of sarcomeric

development, cells were stained for α-actinin (1:200 dilution; Sigma-Aldrich). For analysis of gap junction formation, cells were stained for connexin-43 (1:300 dilution; Sigma-Aldrich) and α-actinin. Mounting medium that included a DAPI counterstain for nuclei was used. Immunostained cells were imaged using confocal microscopy (A1R, Nikon Instruments, NY, USA) at 60x magnification with oil immersion. Analysis of sarcomere lengths, z-band widths, and connexin expression and spatial distribution was conducted using ImageJ software (National Institutes of Health, MD, USA). Analysis of cell orientation was conducted using a MATLAB script that was developed in-house.

B.3.13 Analysis of Gene Expression

RNA was isolated from cardiomyocytes after 21 d of culture by using the E.Z.N.A. Total RNA Kit I (Omega Bio-Tek, GA, USA) according to the manufacturer's protocol. Quantity and purity of RNA was determined by 260/280 nm absorbance. The relative expression levels of selected genes were obtained using quantitative reverse-transcription polymerase chain reaction (qRT-PCR) analyses. cDNA of cultured cells in different condition (10 ng) was prepared using the Maxima SYBR Green/ROX qPCR master mix (Thermo Scientific, MA, USA). Reactions were processed by the ABI 7900HT PCR system with the following parameters: 50°C/2 min and 95°C/10 min, followed by 40 cycles of 95°C/15 s and 60°C/1 min. Results were analyzed using SDS 2.3 software, and relative expression was calculated using the comparative Ct method, where *GAPDH* was designated as the housekeeping gene and cardiomyocytes cultured on TCPS were used as controls. Each sample was run in triplicate reactions for each gene. To examine the maturation of cardiomyocyte contractile machinery, *hMYH7* and

TNNT2 were used as markers, while *GJA1* and *SCN5A* were used as markers for gap junction and voltage-gated ion channel development, respectively. Primers for all assayed genes were purchased from Bio-Rad Laboratories (CA, USA), and used as provided. Amplicon context sequences for these primers have been listed in **Table B.1**.

Table B.1. Amplicon context sequences and lengths for the primers used for qRT-PCR analyses.

Gene	Amplicon Context Sequence	Amplicon Length (bp)
hMYH7	14:23891477-23892840	113
TNNT2	1:201330439-201331128	117
GJA1	6:121756921-121768079	130
SCN5A	3:38614052-38620958	100

B.3.14 Statistical Analyses

All quantitative data is provided as means ± standard error of the mean (SEM). One-way ANOVA with a Tukey's *post-hoc* test was used to analyze data sets that include more than two experimental groups, while a Student's *t*-test was used to compare data sets looking at only two variables. In all analyses, a p-value less than 0.05 was considered significant.

B.4 Results

B.4.1 Fabrication and characterization of conductive nanopatterned silk fibroin-PPy substrates

To better mimic the nanotopographical features of native tissue ECM and thereby provide a more physiologically-relevant microenvironment for cultured cardiomyocytes, capillary force lithography (CFL) was used to pattern silk fibroin substrates (**Figure B.1A**). CFL techniques allow for the generation of nanoscale features with a greater

fidelity and reproducibility than is achievable using methods such as electrospinning[44,45] or directional freezing[46], and can be performed under ambient conditions without the need for a cleanroom. In this study, nanopatterns consisting of aligned grooves and ridges measuring 800 nm × 800 nm × 600 nm (groove width × ridge width × ridge height) were used as these dimensions not only best approximated those of the fiber bundles observed in the ECM, but were also found in a previous study to induce the greatest degree of cellular alignment, hypertrophy, and sarcomere development in cardiomyocytes[33].

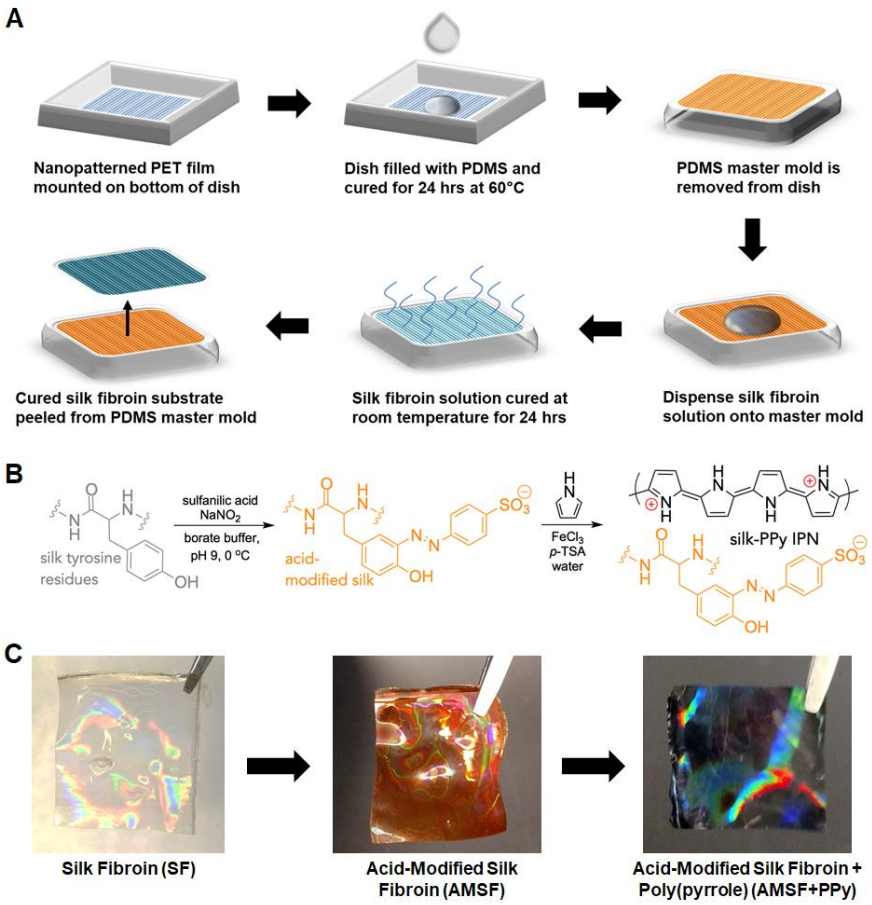

Figure B.1. Fabrication of nanopatterned acid-modified silk fibroin and polypyrrole deposition. (A) Scheme of the process utilized to generate the master mold and subsequent casting of silk fibroin solution to generate nanopatterned substrates. (B) Description of chemical moieties and reactions that occur during the acid modification and PPy deposition stages. (C) Representative photographs of the nanopatterned silk substrates at each stage. The substrates take on an orange hue after acid modification and turn black after PPy deposition. An iridescent sheen is present throughout. Dimensions of the pictured films are 1 cm x 1 cm.

Fabricated silk films were then acid-modified through a diazonium coupling reaction that introduces sulfonic acid groups covalently bound to the silk protein backbone *via* the tyrosine residues (**Figure B.1B**). This acid modification of silk fibroin improves the absorption and intercalation of positively-charged PPy into the now negatively-charged silk network, resulting in a significantly more robust interpenetrating-network composite material that resists delamination and maintains stable electroconductive properties in aqueous environments[20]. PPy was then deposited onto the AMSF films by simply submerging the films in an aqueous solution of pyrrole, p-TSA and $FeCl_3$ for 2 h. The fabrication, modification, and deposition process, progress could be visually monitored, as the silk substrates changed from colorless to orange in the acid modification step (indicative of azo bond formation between the tyrosine and diazonium salt), and from orange to black in the PPy deposition step (**Figure B.1C**). Further details and chemical characterization of the resulting silk-PPy films are given in previous publications[20,47].

Throughout the reaction steps, it was observed that nanopatterned films maintained the iridescent sheen that is characteristic of patterned materials, indicating at a macroscopic scale that the fidelity of the molded pattern was maintained. This finding was confirmed through SEM and AFM imaging of these substrates, where not only were the patterned grooves and ridges well-defined both after acid modification and PPy deposition (**Figure B.2A**), but the measured dimensions of these features were comparable to the initial design as well (**Figure B.2B**). PPy deposition on AMSF had minimal impact on surface roughness and topographical feature size, with the average RMS roughness value of 8.97 ± 0.21 nm practically negligible compared to the patterned ridges that were 600 nm tall (**Figure B.3**). The nanopatterns did not

significantly affect the tensile strength and elastic modulus of the silk-PPy films, as measured values were in the same range as those previously reported for flat films (~7 MPa and ~200 MPa, respectively)[20,47].

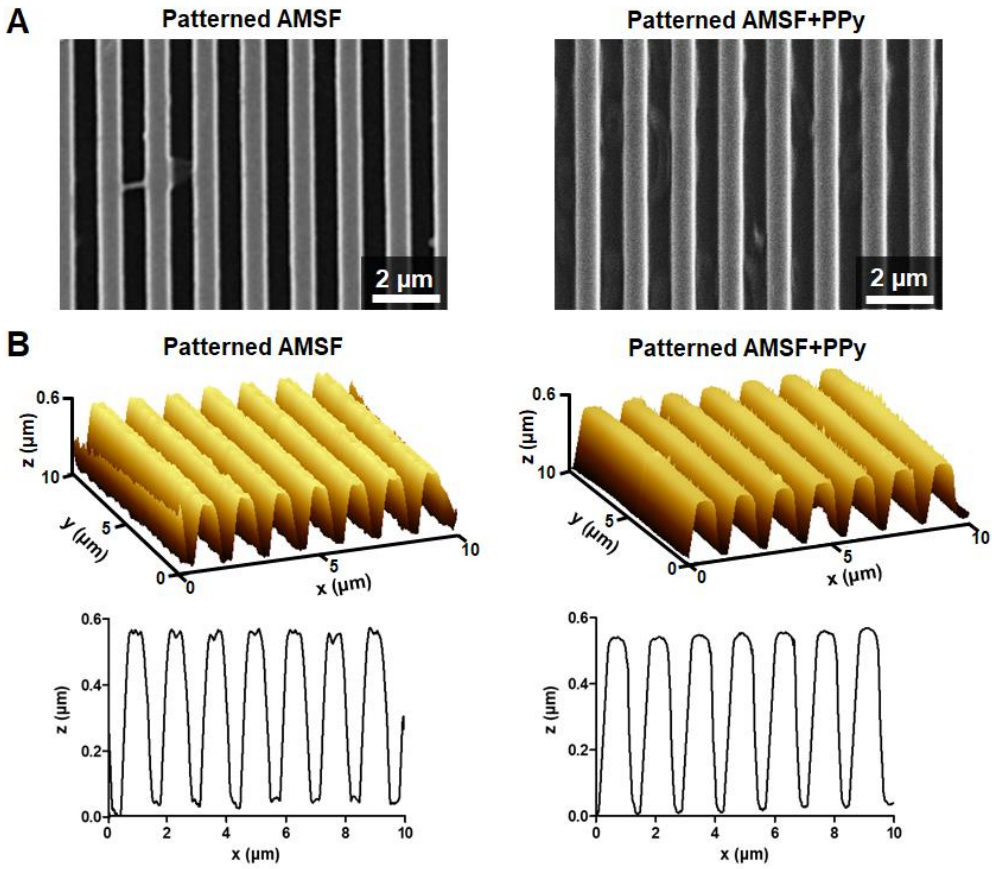

Figure B.2. Characterization of substrate topography. (A) Representative SEM images of nanopatterned substrates with and without PPy. (B) 3D and cross-section AFM profiles illustrate that the fidelity of the nanotopography is well-maintained even after PPy deposition.

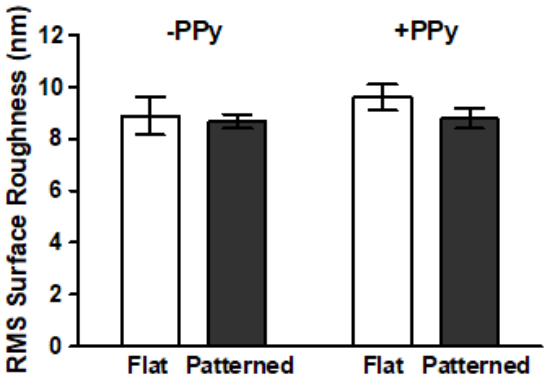

Figure B.3. Surface roughness of fabricated substrates are unaffected by PPy deposition. RMS surface roughness values obtained using AFM show no significant difference across all substrate types.

Four-point probe measurements of the sheet resistivity of AMSF substrates with and without PPy indicate that, as expected, the addition of PPy significantly increases substrate conductivity. The sheet resistivity of the unmodified AMSF was greater than 10^6 Ω/sq, while that of AMSF+PPy was typically in the range of 200-500 Ω/sq (which corresponds to a conductivity of ~1 S/cm). This is further illustrated by current-voltage (I-V) curve measurements in which AMSF+PPy substrates responded to applied voltages and exhibited a non-linear resistive behavior while AMSF-only substrates displayed no response (**Figure B.4**). Additionally, differences in nanotopography had no impact on the overall electrical properties of the silk-PPy composites, as the I-V curves of flat and patterned substrates were virtually identical. Resistivity of the films typically increased by ~3-10 times over 21 days when soaked in aqueous solutions with or without proteins and enzymes[20,47], but even after degradation the conductivities are still higher than that of the native myocardial tissue (0.0002 to 0.0062 S/cm)[48].

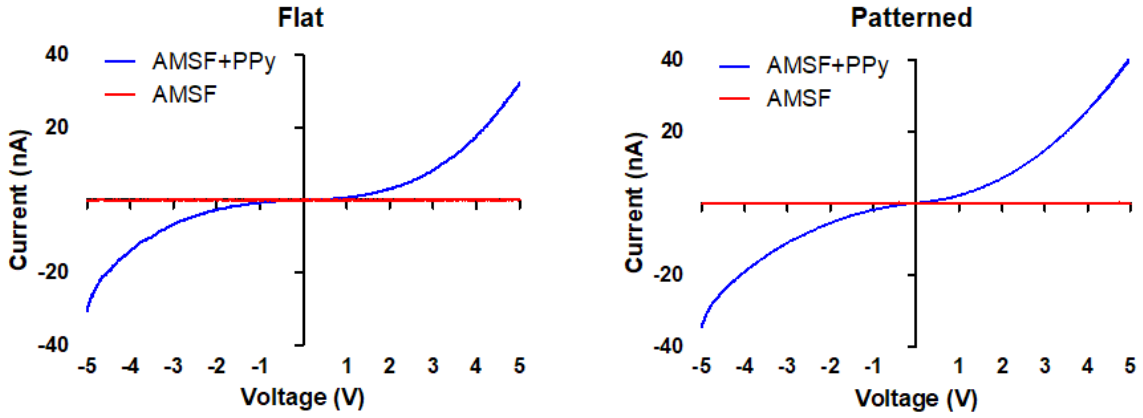

Figure B.4. AMSF+PPy substrates are electrically responsive. I-V curves of flat and patterned substrates indicate that the electroconductive property of the substrates is unaffected by topographical changes.

B.4.2 Enhanced structural organization and sarcomere development by electroconductive and nanotopographical cues

Cardiomyocytes differentiated from human embryonic stem cells were then cultured on flat and patterned AMSF and AMSF+PPy substrates for 21 d before they were fixed and stained for α-actinin to analyze cellular morphology and sarcomeric development. High cell viability was maintained on all substrate types for the entirety of the culture period (**Figure B.5**).

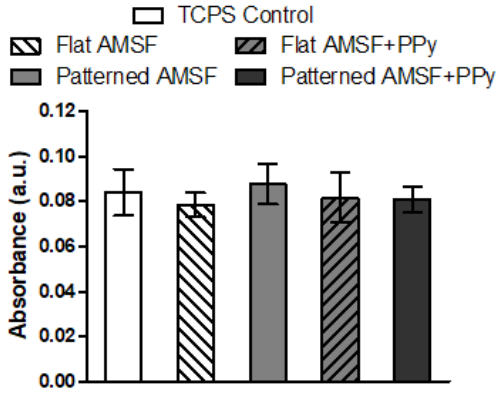

Figure B.5. AMSF and AMSF+PPy substrates are biocompatible. Colorimetric MTS assays of cardiomyocytes cultured for 21 days show that acid-modification and the presence of PPy have no negative impact on cell viability. Viability is presented as normalized absorbance values.

Cells cultured on flat substrates were more disorganized than those on patterned substrates which featured elongated cell bodies that appeared to be aligned to the same axis as the underlying nanotopography (**Figure B.6A**). Quantitative analysis of cell orientation revealed that patterned substrates did indeed induce greater anisotropic orientation compared to flat substrates, although overall alignment is slightly reduced on AMSF+PPy substrates (**Figure B.6B**). However, this did not appear to have a negative impact on sarcomeric development, as cardiomyocytes on patterned substrates possessed longer sarcomeres than those cultured on flat substrates (**Figure B.6C**).

Furthermore, the conductivity imparted by PPy also induced a significant increase in sarcomere length in cells on both patterned and flat substrates. Cellular alignment due to topographical cues increased z-band width, and although there was a statistically significant increase in z-band width in cells on AMSF+PPy substrates, the impact of electroconductivity on this aspect of muscle development appears to be limited (**Figure B.6D**).

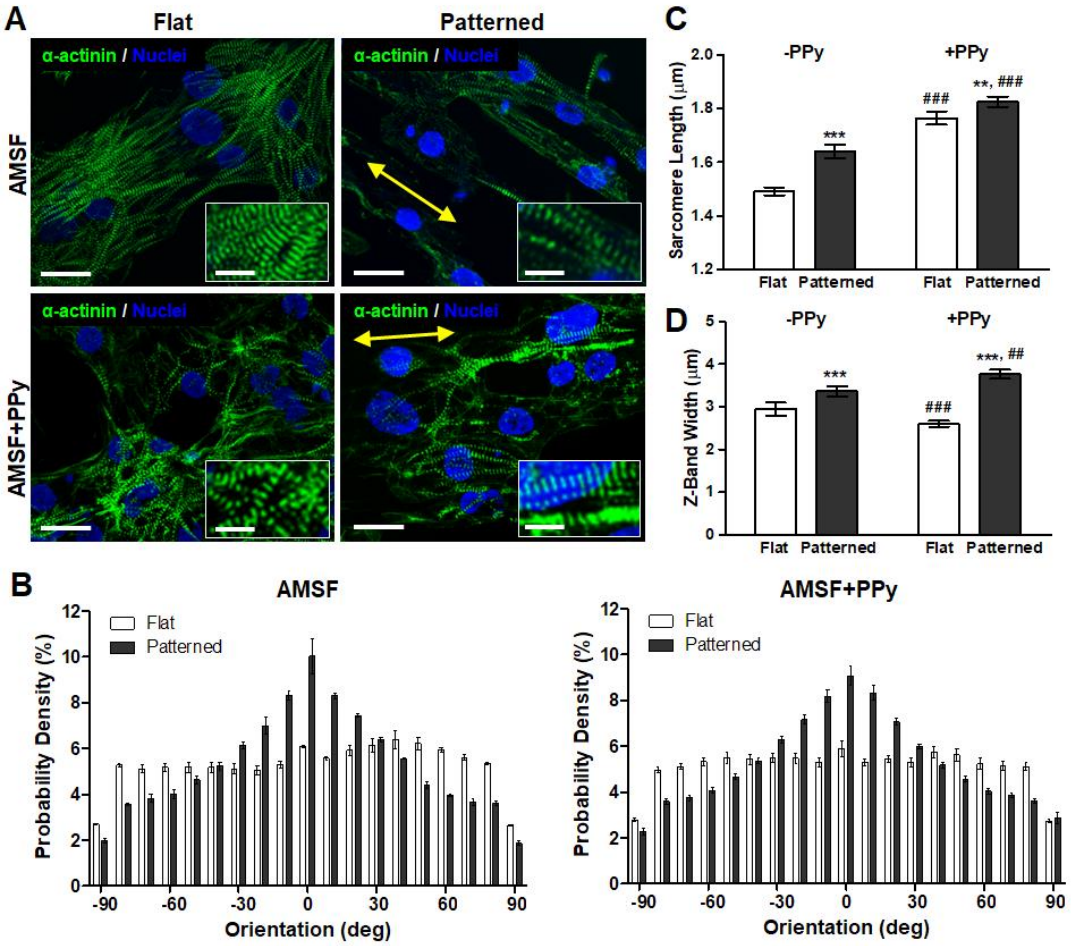

Figure B.6. Nanotopographical and electroconductive cues enhance structural organization and contractile apparatus development. (A) Representative images of cardiomyocytes fluorescently stained for α-actinin (green) and nuclei (blue). Cells on nanopatterned substrates exhibit elongated and aligned morphologies. Yellow arrows indicate the direction of the nanopattern. Scale bars: 25 μm; inset scale bars: 10 μm. (B) Anisotropic nanopatterns induce cell orientation along the axis of the pattern, indicated here by 0°, whereas cells are randomly oriented on flat substrates. (C) Sarcomere length is significantly increased due to nanopatterning and PPy. (D) Z-band width is greatly influenced by topography but is only slightly increased on nanopatterned substrates due to PPy. All quantitative data are presented as means ± SEM, n≥10 different cultures. **p < 0.01, ***p < 0.001 (flat vs. patterned; Student's *t*-test); $^{\#\#}$p < 0.01, $^{\#\#\#}$p < 0.001 (-PPy vs. +PPy; Student's *t*-test).

B.4.3 Modulation of gap junction formation and localization by electroconductive and nanotopographical cues.

Cardiomyocytes were also stained for connexin 43 (Cx43), a gap junction protein critical for regulating the electrical coupling of cardiomyocytes within the mammalian myocardium (**Figure B.7A**). Quantitative analysis of Cx43 expression based on immunostaining revealed that while overall expression on a per cell basis was not significantly different between cells cultured on flat and patterned AMSF+PPy substrates, their expression of Cx43 was significantly greater than that of cells cultured on patterned AMSF, which were in turn was greater than that of cells cultured on flat AMSF (**Figure B.7B**). Localization of Cx43 was then determined by quantifying the amount of Cx43 in the polar regions of each cell as a percentage of total expression.[49] It was found that while nanotopographical cues induced a greater degree of Cx43 polarization, electroconductive cues had no impact on protein distribution (**Figure B.7C**).

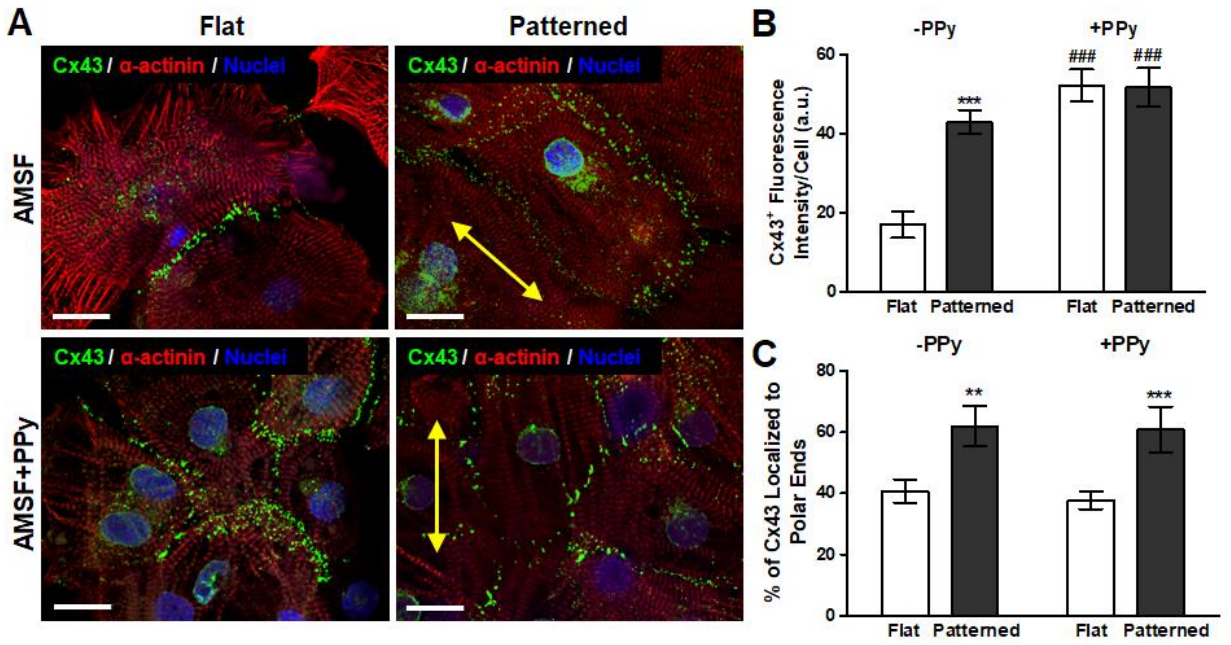

Figure B.7. Modulation of gap junction protein expression and localization due to electroconductivity and anisotropic nanotopography. (A) Representative images of cardiomyocytes fluorescently stained for α-actinin (red), Cx43 (green), and nuclei (blue). Yellow arrows indicate the direction of the nanopattern. Scale bars: 25 μm. (B) While bioinspired nanotopography significantly increased Cx43 expression, the advantage of topographical cues is nearly nullified in the presence of electroconductive cues as PPy elicited a similar degree of Cx43 expression on both flat and patterned substrates. (C) Cx43 polarization is not significantly affected by electroconductive cues as topography dictated protein localization patterns. All quantitative data are presented as means ± SEM, n≥10 different cultures. **p < 0.01, ***p < 0.001 (flat vs. patterned; Student's *t*-test); ###p < 0.001 (-PPy vs. +PPy; Student's *t*-test).

B.4.4 Synergistic effects of nanotopography and electroconductivity on expression of genetic markers for cardiac maturation

After the 21-day culture period, RNA was collected from cultured hPSC-CMs and the expression levels of representative markers for cardiomyocyte development were quantitatively analyzed with qRT-PCR. Genes were selected such that the impact of substrate properties on both contractile and electrical function could be examined at the tissue level. Cardiomyocytes on patterned substrates saw a significantly increased expression of *hMYH7*, which codes for β-myosin heavy chain (β-MHC), the predominant isoform of MHC in the adult human ventricular myocardium[50]. *hMYH7* expression was

further increased in cells cultured on AMSF+PPy substrates compared to their counterparts on non-conductive substrates (**Figure B.8A**). On the other hand, expression of cardiac troponin T2 (*TNNT2*), a key regulator of myocyte contraction, was unaffected by substrate topography and only showed increases in expression when cells were exposed to PPy (**Figure B.8B**). In agreement with the aforementioned observations from the immunohistochemical analysis of gap junction development *via* Cx43, electroconductivity appears to be a more significant driving factor compared to nanotopography when it comes to regulating the expression of (*GJA1*) (**Figure B.8C**). Similar to the trends noted for *hMYH7* expression, topographical and electroconductive cues both promoted the upregulation of the voltage-gated sodium channel $Na_V1.5$ (*SCN5A*), with the greatest expression levels seen in cells that were cultured on AMSF+PPy substrates (**Figure B.8D**). $Na_V1.5$ generates the fast sodium current which regulates the cardiac action potential; therefore, the degree of its expression has a significant effect on cardiac conduction velocity[51].

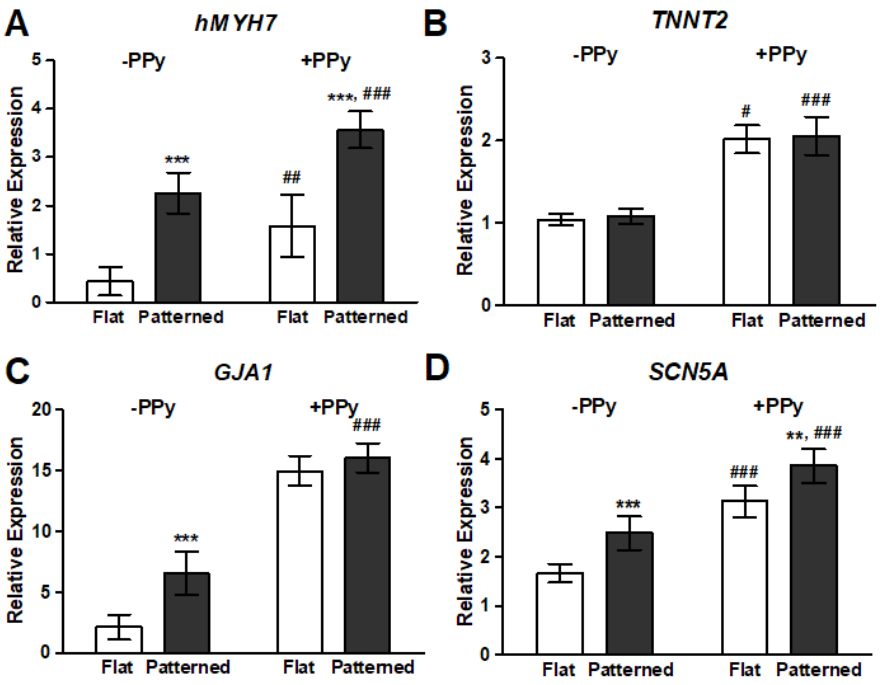

Figure B.8. Nanotopography and electroconductivity synergistically induced the largest increases in genetic markers for cardiac maturation. qRT-PCR analysis of the relative expression levels of: (A) β-myosin heavy chain (*hMYH7*), (B) cardiac troponin T2 (*TNNT2*), (C) connexin 43 (*GJA1*), and (D) $Na_V1.5$ (*SCN5A*). Presence of biomimetic nanotopography significantly increased gene expression, with the exception of *TNNT2*. Cardiomyocytes cultured on electroconductive silk substrates exhibited an increased expression of all assayed genes when compared to cells on non-conductive substrates. All data are presented as means ± SEM, n≥6 different cultures, **p < 0.01, ***p < 0.001 (flat vs. patterned; Student's *t*-test); $^{\#}p < 0.05$, $^{\#\#}p < 0.01$, $^{\#\#\#}p < 0.001$ (-PPy vs. +PPy; Student's *t*-test).

B.5 Discussion

The method presented here of fabricating biodegradable substrates possessing both electrical conductivity and biomimetic nanotopography offers some significant advantages over other previously reported techniques. Since electroconductive functionality is achieved by absorbing PPy into the existing silk network in a uniform manner, nanoscale features that are present on the surface are maintained without risk of changes in dimension or shape. This contrasts with other methods, such as chemical vapor deposition (CVD), where the conductive materials are deposited onto patterned surfaces and the resulting coating can be inhomogenous[52-54]. Since the PPy itself is not

biodegradable, the ability to incorporate it only in the surface of the silk substrate minimizes the amount of PPy necessary to make the composites conductive[18,19]. Furthermore, the relative simplicity of the acid modification, CFL patterning, and PPy conjugation processes obviate the need for complex training and expensive equipment. This drives down cost while improving reproducibility, thereby increasing the translatability of the fabrication method and likelihood of adoption by a variety of end-users.

Given the importance of tissue structure on the functional capabilities of the myocardium *in vivo*, it is critical that this cellular organization is recapitulated within engineered myocardial tissues. Our results confirm the benefits of using bioinspired nanotopographies to achieve this goal, as not only was the overall anisotropic alignment of cultured cardiomyocytes enhanced by topography-mediated contact guidance cues, but this alignment also led to significant improvements in sarcomere organization and development. The sarcomere is the fundamental unit for cardiomyocyte contraction, and cells that possess longer sarcomeres are generally capable of producing greater contractile forces[55]. In relaxed adult human cardiomyocytes, sarcomere lengths are typically approximately 2.2 μm[56], whereas sarcomere lengths in immature hPSC-CMs have been reported to be approximately 33% shorter at 1.65 μm[57], In this study, by simply inducing an elongated morphology in cells, average sarcomere lengths could be increased by 10%. For cells cultured on the electroconductive AMSF+PPy substrates, a 23% increase was observed, with average sarcomere length at a near physiological value of 1.83 μm. The lateral alignment of multiple myofibrils is also important, as this allows for synchronous contractions of sarcomeres over larger length-scales, thereby

enabling cardiac tissue to produce strong twitch forces[58]. Correspondingly, more mature cardiomyocytes possess larger z-band widths. The maturation benefits of promoting of cellular alignment is once again evident as these morphological changes led to a greater number of sarcomeres to be in register, thus leading to significantly increased z-band widths in anisotropically organized cells.

These results also provide interesting insights into the impact of electroconductivity on gap junction formation. Culturing of cardiomyocytes on electroconductive substrates leads to an overall increase in the amount of Cx43 expressed per cell, and this result confirms previous observations reported in literature[7,54]. At the same time, it is apparent that while anisotropic cellular organization as a result of nanotopography also increases expression in cells, it plays an even more significant role in concentrating Cx43 at the polar junctions of adjacent cells. This finding highlights the critical importance of organizing cardiomyocytes in a physiological manner, as it is this polarization of Cx43 that enables the rapid and efficient propagation of action potentials in a uniaxial manner that subsequently leads to the contraction in a concerted direction that is required for the proper function of myocardial tissue[59,60]. Indeed, abundant expression of Cx43 and its polar localization is one of the hallmarks of fully differentiated ventricular myocytes *in vivo*[61].

It has become increasingly clear that mechanical and topographical cues play a crucial role in the modulation of cellular epigenetics and function. These cell-matrix interactions are largely mediated by integrins, which are cell surface receptors that regulate a variety of downstream signaling cascades that affect cell morphology, proliferation, differentiation, migration, and gene expression[62]. Integrins typically cluster

together to form focal adhesion complexes, and the frequency, shape, and distribution of this clustering is greatly influenced by topographical features at the sub-micron level[63]. Focal adhesion kinase (FAK) localizes at these complexes and acts in conjunction with integrins to transduce extracellular mechanical signals to dictate cellular processes. FAK and FAK-associated signaling has been implicated in regulating cardiogenesis *via* adhesive and topographical cues *in vitro*[34,64,65], and the role of both integrins and FAK in cardiac organogenesis and maturation is so critical, that ablation or disruption of their function has been shown to result in embryonic mortality *in vivo*[66-68]. Thus, by mimicking native ECM topography with the substrates developed in this study, we were able to leverage these mechanotransductive processes to impart beneficial maturation effects on cultured hPSC-CMs.

It is also evident that electroconductive cues have a profound effect on almost all major aspects of cardiomyocyte development. While there is an abundance of evidence that conductive materials drive the maturation of myocytes, the exact mechanisms and pathways involved have yet to be fully elucidated. One hypothesis suggests that close proximity of cell membranes to conductive surfaces induces a hyperpolarization of the membrane resting potential, which has been demonstrated to be an important factor in promoting the cardiomyocyte maturation process[69]. It has also been suggested that the ability for conducting materials to not only improve the adsorption of proteins, but also induce a more bioactive conformation of these proteins, allows for a greater presentation of maturation-promoting biochemical cues[70,71]. The myocardium is an electrically active tissue with an inherent conductivity reported to range from 0.02 to 0.62 S/m and is permeated with conductive Purkinje fibers that assist with action

potential propagation[48]. Thus, the presence of an electrically-responsive material in the cell culture microenvironment could serve to reproduce the extracellular voltage gradients and electrical fields that are present *in vivo* and are known to significantly influence developmental processes[72].

By using nanopatterned AMSF+PPy substrates for culturing hPSC-CMs, we have demonstrated the ability to harness the combined benefits of electroconductivity and bioinspired nanotopography for enhancing cardiomyocyte development. In addition to adopting an anisotropic morphology, cultured cardiomyocytes exhibited markedly improved sarcomere and gap junction development and organization. The pro-maturation effects of the substrates were also reflected in the increased expression levels of genes associated with proteins that are critical for proper cardiac tissue excitation-contraction function. Corresponding improvements in functional capability, such as force generation and action potential conduction velocity, remain to be investigated in future studies. The results presented here add to a growing body of evidence that the overall maturation of a variety of cell types, especially cardiac and skeletal myocytes, can be drastically improved when biomimetic nanotopography and electrical cues are both present in the culture microenvironment[53,54,73-76]. In addition to the beneficial effects of the substrates on cell maturation, the ability to obtain defined nanoscale features and electroconductive properties in a pliable, biodegradable, and biocompatible platform also greatly expands the potential for this composite material to be used in a variety of *in vivo* applications, such as for engineering tissue patches and implantable devices[77-79].

B.6 References

1 Guo, B. L., Glavas, L. & Albertsson, A. C. Biodegradable and electrically conducting polymers for biomedical applications. *Prog. Polym. Sci.* **38**, 1263-1286 (2013).

2 Lee, T. J. *et al.* Graphene enhances the cardiomyogenic differentiation of human embryonic stem cells. *Biochem. Biophys. Res. Commun.* **452**, 174-180 (2014).

3 Shin, S. R. *et al.* Reduced graphene oxide-gelMA hybrid hydrogels as scaffolds for cardiac tissue engineering. *Small* **12**, 3677-3689 (2016).

4 Martinelli, V. *et al.* Carbon nanotubes instruct physiological growth and functionally mature syncytia: nongenetic engineering of cardiac myocytes. *ACS Nano* **7**, 5746-5756 (2013).

5 Shin, S. R. *et al.* Carbon-nanotube-embedded hydrogel sheets for engineering cardiac constructs and bioactuators. *ACS Nano* **7**, 2369-2380 (2013).

6 Wu, Y., Wang, L., Guo, B. & Ma, P. X. Interwoven aligned conductive nanofiber yarn/hydrogel composite scaffolds for engineered 3D cardiac anisotropy. *ACS Nano* **11**, 5646-5659 (2017).

7 You, J. O., Rafat, M., Ye, G. J. C. & Auguste, D. T. Nanoengineering the heart: conductive scaffolds enhance connexin 43 expression. *Nano Lett.* **11**, 3643-3648 (2011).

8 Fleischer, S., Shevach, M., Feiner, R. & Dvir, T. Coiled fiber scaffolds embedded with gold nanoparticles improve the performance of engineered cardiac tissues. *Nanoscale* **6**, 9410-9414 (2014).

9 Shevach, M., Maoz, B. M., Feiner, R., Shapira, A. & Dvir, T. Nanoengineering gold particle composite fibers for cardiac tissue engineering. *J. Mater. Chem. B* **1**, 5210-5217 (2013).

10 Borriello, A., Guarino, V., Schiavo, L., Alvarez-Perez, M. A. & Ambrosio, L. Optimizing PANi doped electroactive substrates as patches for the regeneration of cardiac muscle. *J. Mater. Sci. Mater. Med.* **22**, 1053-1062 (2011).

11 Wang, L., Wu, Y., Hu, T., Guo, B. & Ma, P. X. Electrospun conductive nanofibrous scaffolds for engineering cardiac tissue and 3D bioactuators. *Acta Biomater.* **59**, 68-81 (2017).

12 Dong, R. N., Zhao, X., Guo, B. L. & Ma, P. X. Self-healing conductive injectable hydrogels with antibacterial activity as cell delivery carrier for cardiac cell therapy. *ACS Appl. Mater. Interfaces* **8**, 17138-17150 (2016).

13 Guimard, N. K., Gomez, N. & Schmidt, C. E. Conducting polymers in biomedical engineering. *Prog. Polym. Sci.* **32**, 876-921 (2007).

14 Wang, X. D. *et al.* Evaluation of biocompatibility of polypyrrole in vitro and in vivo. *J. Biomed. Mater. Res. A* **68a**, 411-422 (2004).

15 Balint, R., Cassidy, N. J. & Cartmell, S. H. Conductive polymers: towards a smart biomaterial for tissue engineering. *Acta Biomater.* **10**, 2341-2353 (2014).

16 Kai, D., Prabhakaran, M. P., Jin, G. R. & Ramakrishna, S. Polypyrrole-contained electrospun conductive nanofibrous membranes for cardiac tissue engineering. *J. Biomed. Mater. Res. A* **99a**, 376-385 (2011).

17 Spearman, B. S. *et al.* Conductive interpenetrating networks of polypyrrole and polycaprolactone encourage electrophysiological development of cardiac cells. *Acta Biomater.* **28**, 109-120 (2015).
18 Kaur, G., Adhikari, R., Cass, P., Bown, M. & Gunatillake, P. Electrically conductive polymers and composites for biomedical applications. *RSC Adv.* **5**, 37553-37567 (2015).
19 Hardy, J. G., Lee, J. Y. & Schmidt, C. E. Biomimetic conducting polymer-based tissue scaffolds. *Curr. Opin. Biotechnol.* **24**, 847-854 (2013).
20 Romero, I. S., Schurr, M. L., Lally, J. V., Kotlik, M. Z. & Murphy, A. R. Enhancing the interface in silk-polypyrrole composites through chemical modification of silk fibroin. *ACS Appl. Mater. Interfaces* **5**, 553-564 (2013).
21 Aznar-Cervantes, S. *et al.* Fabrication of conductive electrospun silk fibroin scaffolds by coating with polypyrrole for biomedical applications. *Bioelectrochemistry* **85**, 36-43 (2012).
22 Hardy, J. G. *et al.* Into the groove: instructive silk-polypyrrole films with topographical guidance cues direct DRG neurite outgrowth. *J. Biomater. Sci. Polym. Ed.* **26**, 1327-1342 (2015).
23 Wang, Y. Z., Kim, H. J., Vunjak-Novakovic, G. & Kaplan, D. L. Stem cell-based tissue engineering with silk biomaterials. *Biomaterials* **27**, 6064-6082 (2006).
24 Omenetto, F. G. & KapLan, D. L. A new route for silk. *Nat. Photonics* **2**, 641-643 (2008).
25 Bissell, M. J., Hall, H. G. & Parry, G. How does the extracellular matrix direct gene expression? *J. Theor. Biol.* **99**, 31-68 (1982).
26 LaNasa, S. M. & Bryant, S. J. Influence of ECM proteins and their analogs on cells cultured on 2-D hydrogels for cardiac muscle tissue engineering. *Acta Biomater.* **5**, 2929-2938 (2009).
27 Kim, D. H., Provenzano, P. P., Smith, C. L. & Levchenko, A. Matrix nanotopography as a regulator of cell function. *J. Cell Biol.* **197**, 351-360 (2012).
28 Kim, D. H. *et al.* Nanoscale cues regulate the structure and function of macroscopic cardiac tissue constructs. *Proc. Natl. Acad. Sci. U. S. A.* **107**, 565-570 (2010).
29 Genet, M. *et al.* Distribution of normal human left ventricular myofiber stress at end diastole and end systole: a target for in silico design of heart failure treatments. *J. Appl. Physiol. (1985)* **117**, 142-152 (2014).
30 Sosnovik, D. E., Wang, R., Dai, G., Reese, T. G. & Wedeen, V. J. Diffusion MR tractography of the heart. *J. Cardiovasc. Magn. Reson.* **11**, 47 (2009).
31 Streeter, D. D. & Bassett, D. L. An engineering analysis of myocardial fiber orientation in pigs left ventricle in systole. *Anat. Rec.* **155**, 503-& (1966).
32 Thavandiran, N., Nunes, S. S., Xiao, Y. & Radisic, M. Topological and electrical control of cardiac differentiation and assembly. *Stem Cell Res. Ther.* **4** (2013).
33 Carson, D. *et al.* Nanotopography-induced structural anisotropy and aarcomere development in human cardiomyocytes derived from induced pluripotent stem cells. *ACS Appl. Mater. Interfaces* **8**, 21923-21932 (2016).
34 Kim, D. H. *et al.* Nanopatterned cardiac cell patches promote stem cell niche formation and myocardial regeneration. *Integr. Biol.* **4**, 1019-1033 (2012).

35 Liu, W. H. *et al.* Human induced pluripotent stem cell and nanotechnology-based therapeutics. *Cell Transplant.* **24**, 2185-2195 (2015).
36 Acimovic, I. *et al.* Human pluripotent stem cell-derived cardiomyocytes as research and therapeutic tools. *BioMed Res. Int.* (2014).
37 Lancaster, M. A. & Knoblich, J. A. Organogenesis in a dish: modeling development and disease using organoid technologies. *Science* **345** (2014).
38 Smith, A. S. T., Macadangdang, J., Leung, W., Laflamme, M. A. & Kim, D. H. Human iPSC-derived cardiomyocytes and tissue engineering strategies for disease modeling and drug screening. *Biotechnol. Adv.* **35**, 77-94 (2017).
39 Laflamme, M. A. & Murry, C. E. Heart regeneration. *Nature* **473**, 326-335 (2011).
40 Gherghiceanu, M. *et al.* Cardiomyocytes derived from human embryonic and induced pluripotent stem cells: comparative ultrastructure. *J. Cell. Mol. Med.* **15**, 2539-2551 (2011).
41 Macadangdang, J. *et al.* Capillary force lithography for cardiac tissue engineering. *J. Vis. Exp.* (2014).
42 Tsui, J. H. *et al.* Harnessing sphingosine-1-phosphate signaling and nanotopographical cues to regulate skeletal muscle maturation and vascularization. *ACS Nano* **11**, 11954-11968 (2017).
43 Zhu, W. Z., Van Biber, B. & Laflamme, M. A. Methods for the derivation and use of cardiomyocytes from human pluripotent stem cells. *Methods Mol. Biol.* **767**, 419-431 (2011).
44 Zhang, X. H., Baughman, C. B. & Kaplan, D. L. In vitro evaluation of electrospun silk fibroin scaffolds for vascular cell growth. *Biomaterials* **29**, 2217-2227 (2008).
45 Meinel, A. J. *et al.* Optimization strategies for electrospun silk fibroin tissue engineering scaffolds. *Biomaterials* **30**, 3058-3067 (2009).
46 Stoppel, W. L., Hu, D. J., Domian, I. J., Kaplan, D. L. & Black, L. D. Anisotropic silk biomaterials containing cardiac extracellular matrix for cardiac tissue engineering. *Biomed. Mater.* **10** (2015).
47 Larson, J. D. *et al.* Enhanced actuation performance of silk-polypyrrole composites. *Mater. Chem. Phys.* **186**, 67-74 (2017).
48 Roth, B. J. Electrical conductivity values used with the bidomain model of cardiac tissue. *IEEE Trans. Biomed. Eng.* **44**, 326-328 (1997).
49 Salameh, A. *et al.* Cyclic mechanical stretch induces cardiomyocyte orientation and polarization of the gap junction protein connexin43. *Circ. Res.* **106**, 1592-1602 (2010).
50 Morkin, E. Control of cardiac myosin heavy chain gene expression. *Microsc. Res. Tech.* **50**, 522-531 (2000).
51 Park, D. S. & Fishman, G. I. The cardiac conduction system. *Circulation* **123**, 904-915 (2011).
52 Yu, Q. K. *et al.* Control and characterization of individual grains and grain boundaries in graphene grown by chemical vapour deposition. *Nat. Mater.* **10**, 443-449 (2011).
53 Yang, H. S. *et al.* Electroconductive nanopatterned substrates for enhanced myogenic differentiation and maturation. *Adv. Healthc. Mater.* **5**, 137-145 (2016).
54 Smith, A. S. T. *et al.* Micro- and nano-patterned conductive graphene-PEG hybrid scaffolds for cardiac tissue engineering. *Chem. Commun.* **53**, 7412-7415 (2017).

55 Hibberd, M. G. & Jewell, B. R. Calcium- and length-dependent force production in rat ventricular muscle. *J. Physiol.* **329**, 527-540 (1982).
56 Bird, S. D. *et al.* The human adult cardiomyocyte phenotype. *Cardiovasc. Res.* **58**, 423-434 (2003).
57 Lundy, S. D., Zhu, W. Z., Regnier, M. & Laflamme, M. A. Structural and functional maturation of cardiomyocytes derived from human pluripotent stem cells. *Stem Cells Dev.* **22**, 1991-2002 (2013).
58 Rodriguez, A. G., Rodriguez, M. L., Han, S. J., Sniadecki, N. J. & Regnier, M. Enhanced contractility with 2-deoxy-ATP and EMD 57033 is correlated with reduced myofibril structure and twitch power in neonatal cardiomyocytes. *Integr. Biol.* **5**, 1366-1373 (2013).
59 Roell, W. *et al.* Engraftment of connexin 43-expressing cells prevents post-infarct arrhythmia. *Nature* **450**, 819-824 (2007).
60 Bukauskas, F. F. *et al.* Clustering of connexin 43-enhanced green fluorescent protein gap junction channels and functional coupling in living cells. *Proc. Natl. Acad. Sci. U. S. A.* **97**, 2556-2561 (2000).
61 Fromaget, C., el Aoumari, A. & Gros, D. Distribution pattern of connexin 43, a gap junctional protein, during the differentiation of mouse heart myocytes. *Differentiation* **51**, 9-20 (1992).
62 Ross, R. S. & Borg, T. K. Integrins and the myocardium. *Circ. Res.* **88**, 1112-1119 (2001).
63 Biggs, M. J. P., Richards, R. G. & Dalby, M. J. Nanotopographical modification: a regulator of cellular function through focal adhesions. *Nanomedicine* **6**, 619-633 (2010).
64 Hakuno, D., Takahashi, T., Lammerding, J. & Lee, R. T. Focal adhesion kinase signaling regulates cardiogenesis of embryonic stem cells. *J. Biol. Chem.* **280**, 39534-39544 (2005).
65 Simpson, D. G. *et al.* Modulation of cardiac myocyte phenotype in vitro by the composition and orientation of the extracellular matrix. *J. Cell. Physiol.* **161**, 89-105 (1994).
66 Stephens, L. E. *et al.* Deletion of beta 1 integrins in mice results in inner cell mass failure and peri-implantation lethality. *Genes Dev.* **9**, 1883-1895 (1995).
67 Baudoin, C., Goumans, M. J., Mummery, C. & Sonnenberg, A. Knockout and knockin of the beta1 exon D define distinct roles for integrin splice variants in heart function and embryonic development. *Genes Dev.* **12**, 1202-1216 (1998).
68 Peng, X. *et al.* Cardiac developmental defects and eccentric right ventricular hypertrophy in cardiomyocyte focal adhesion kinase (FAK) conditional knockout mice. *Proc. Natl. Acad. Sci. U. S. A.* **105**, 6638-6643 (2008).
69 van Vliet, P. *et al.* Hyperpolarization Induces Differentiation in Human Cardiomyocyte Progenitor Cells. *Stem Cell Rev. Rep.* **6**, 178-185 (2010).
70 Molino, P. J., Higgins, M. J., Innis, P. C., Kapsa, R. M. I. & Wallace, G. G. Fibronectin and bovine serum albumin adsorption and conformational dynamics on inherently conducting polymers: a QCM-D study. *Langmuir* **28**, 8433-8445 (2012).

71 Wan, A. M. D. *et al.* 3D conducting polymer platforms for electrical control of protein conformation and cellular functions. *J. Mater. Chem. B* **3**, 5040-5048 (2015).
72 McCaig, C. D., Rajnicek, A. M., Song, B. & Zhao, M. Controlling cell behavior electrically: current views and future potential. *Physiol. Rev.* **85**, 943-978 (2005).
73 Ku, S. H., Lee, S. H. & Park, C. B. Synergic effects of nanofiber alignment and electroactivity on myoblast differentiation. *Biomaterials* **33**, 6098-6104 (2012).
74 Chen, M. C., Sun, Y. C. & Chen, Y. H. Electrically conductive nanofibers with highly oriented structures and their potential application in skeletal muscle tissue engineering. *Acta Biomater.* **9**, 5562-5572 (2013).
75 Thrivikraman, G., Mallik, P. K. & Basu, B. Substrate conductivity dependent modulation of cell proliferation and differentiation in vitro. *Biomaterials* **34**, 7073-7085 (2013).
76 Heidi Au, H. T., Cui, B., Chu, Z. E., Veres, T. & Radisic, M. Cell culture chips for simultaneous application of topographical and electrical cues enhance phenotype of cardiomyocytes. *Lab Chip* **9**, 564-575 (2009).
77 Wendel, J. S., Ye, L., Zhang, P. Y., Tranquillo, R. T. & Zhang, J. Y. J. Functional consequences of a tissue-engineered myocardial patch for cardiac repair in a rat infarct model. *Tissue Eng. Part A* **20**, 1325-1335 (2014).
78 Dvir, T. *et al.* Nanowired three-dimensional cardiac patches. *Nat. Nanotechnol.* **6**, 720-725 (2011).
79 Zhou, J. *et al.* Engineering the heart: evaluation of conductive nanomaterials for improving implant integration and cardiac function. *Sci. Rep.* **4** (2014).

Appendix C. Harnessing Sphingosine-1-Phosphate Signaling and Nanotopographical Cues to Regulate Skeletal Muscle Maturation and Vascularization

This appendix has been published in the following co-first-authored manuscript:

J.H. Tsui*, K. Janebodin*, N. Ieronimakis, D.M.P. Yama, H.S. Yang, R. Chavanachat, A.L. Hays, H. Lee, M. Reyes, D.H. Kim. Harnessing sphingosine-1-phosphate signaling and nanotopographical cues to regulate skeletal muscle maturation and vascularization. *ACS Nano.* **11**, 11954-11968 (2017).

C.1 Abstract

Despite possessing substantial regenerative capacity, skeletal muscle can suffer from loss of function due to catastrophic traumatic injury or degenerative disease. In such cases, engineered tissue grafts hold the potential to restore function and improve patient quality of life. Requirements for successful integration of engineered tissue grafts with the host musculature include cell alignment that mimics host tissue architecture and directional functionality, as well as vascularization to ensure tissue survival. Here we have developed biomimetic nanopatterned poly(lactic-co-glycolic acid) (PLGA) substrates conjugated with sphingosine-1-phosphate (S1P), a potent angiogenic and myogenic factor, to enhance myoblast and endothelial maturation. Primary muscle cells cultured on these functionalized S1P nanopatterned substrates developed a highly aligned and elongated morphology, and exhibited higher expression levels of myosin heavy chain, in addition to genes characteristic of mature skeletal muscle. We also found that S1P enhanced angiogenic potential in these cultures, as evidenced by elevated expression of endothelial-related genes. Computational analyses

of live-cell videos showed a significantly improved functionality of tissues cultured on S1P-functionalized nanopatterns as indicated by greater myotube contraction displacements and velocities. In summary, our study demonstrates that biomimetic nanotopography and S1P can be combined to synergistically regulate the maturation and vascularization of engineered skeletal muscles.

C.2 Introduction

The loss of skeletal muscle function and volume due to traumatic injury and myopathies such as muscular dystrophy is a significant healthcare problem for which there are currently few interventions[1-3]. Tissue grafts have shown potential in animal models for restoring damaged or wasted muscles. However, autologous and allogeneic tissue grafting is often associated with detrimental effects such as donor site morbidity or long-term immunosuppression[4]. Likewise, although stem cell-based therapies have shown some promise for improving patient outcomes[5-7], such techniques are associated with poor survival, maturation and functional integration of transplanted cells[8-11]. To address these shortcomings, tissue engineering approaches have been extensively investigated[12,13], with the overarching goal of generating tissues *in vitro* that are capable of restoring function to diseased or injured muscles when engrafted *in vivo.*

Skeletal muscle is comprised of dense, multinucleated muscle fibers that are anisotropically oriented to allow for longitudinal contraction and force generation. As such, one of the most important requirements for engineering functional skeletal muscle tissues is the recapitulation of this highly-organized structure. Muscle extracellular matrix (ECM) architecture has been found to influence cellular behavior and processes

critical for overall tissue function. Ultrastructural analysis has revealed that muscle ECM is comprised of highly aligned collagen fiber bundles that feature widths of several hundred nanometers[14,15]. Advances in micro- and nanofabrication techniques have led to the development of substrates or scaffolds that mimic these structures, and studies have shown that substrates with biomimetic nanotopographies can induce the formation of ordered muscle tissue *in vitro* in a physiologically-relevant manner by influencing both cellular organization and maturation[16-18].

Skeletal muscle is a metabolically demanding tissue, which necessitates a high degree of vascularization. Consequently, engineered muscle should also meet this requirement, particularly if the eventual goal of generating 3D tissue constructs is to be realized. Additionally, vascularization improves cell survival upon implantation by promoting blood perfusion and in turn reducing apoptosis[19,20]. To date, most approaches for generating vascularized tissues have revolved around the use of one or multiple angiogenic factors such as vascular endothelial growth factor (VEGF), basic fibroblast growth factor (bFGF), and platelet-derived growth factor (PDGF) that are delivered *via* scaffolds or integrated depots such as microspheres[21-25]. Although significant progress has been achieved with these methods, many challenges remain. The use of angiogenic growth factors has proven to be effective at inducing vascularization, although some of these factors have been shown to repress myogenesis[26,27]. In addition, the use of recombinant growth factors can be inefficient, as their high cost may mitigate further development or their application for large scale implants.

In this study, we developed an approach for engineering vascularized and more mature skeletal muscle in which biodegradable and biomimetically nanopatterned

substrates were conjugated with sphingosine-1-phosphate (S1P), a sphingolipid G-protein-coupled receptor ligand known to have potent angiogenic and myogenic effects[28-31]. Use of this small molecule agonist is advantageous for modulating both processes and obviates the need for multiple growth factors, greatly simplifying the culture platform. Substrate functionalization was achieved using 3,4-dihydroxy-L-phenylalanine (DOPA), a naturally-occurring amino acid derived from mussel adhesive pads[32]. DOPA is capable of forming both strong ionic and covalent bonds with organic molecules through a Michael-addition type reaction without requiring harsh solvents or reagents, and is therefore a process that is likely to maintain the biological activity of S1P. It was hypothesized that the benefits of biomimetic nanotopography and sustained S1P signaling could be harnessed synergistically to induce the formation of structurally organized skeletal muscle tissues that are both mature and vascularized. This capability for generating tissues comprised of functional muscle fibers with a vascular component for nutrient delivery will serve as a promising method for developing therapeutic or investigative platforms.

C.3 Materials and Methods

C.3.1 Substrate Fabrication

Flat and nanopatterned substrates were generated using a capillary force lithography (CFL) technique that has been detailed previously[17]. Briefly, polyurethane acrylate (PUA; Minuta Technology, Korea), and polydimethylsiloxane (PDMS, Sylgard 184, Dow Corning, MI, USA) were first prepared to form the molds and solvent-

absorbing sheets, respectively. PUA molds were fabricated by first dispensing PUA precursor onto a patterned silicon wafer master which had been made using standard photolithography techniques, and lightly pressing a polyethylene terephthalate (PET, Skyrol®, SKC Inc., Korea) film (thickness = 75 μm) against the PUA. The PUA precursor spontaneously filled the cavities of the master mold by means of capillary action and was cured by exposure to UV light (λ = 250-400 nm) for approximately 30 s (dose = 100 mJ/cm^2). After this initial curing, the PUA mold was peeled off from the substrate and further exposed to UV light overnight for complete curing. PDMS sheets were made by first combining polymer precursor and curing agent at a mixing ratio of 10:1 and cured at 60°C for 10 hrs before manually cutting prior to use.

To generate the substrates used in this study, a 100 μL drop of 15% w/v PLGA (MW: 50,000 – 75,000, 50:50 lactide:glycolide ratio, Sigma-Aldrich, MO, USA) dissolved in chloroform was dispensed onto a clean glass coverslip, and a PDMS sheet was placed on top of the polymer solution. Slight pressure (~10 kPa) was applied evenly on the PDMS for 5 min before the sheet was removed. The PLGA-coated coverslip was then placed onto a hot plate preheated to 120°C for 5 min to allow any residual solvent to evaporate. A nanopatterned PUA mold was then placed on top with constant pressure (~100 kPa) applied for 15 min before the entire assembly was removed from heat and allowed to cool to room temperature. The mold was carefully peeled off and the nanopatterned PLGA substrate is stored under desiccation until ready for use. For this study, substrates with 800 x 800 x 600 nm (groove width x ridge width x groove depth) feature sizes were used. Flat PLGA substrates were fabricated by skipping the patterning steps, and were also stored under desiccation.

C.3.2 Substrate Functionalization with S1P

Fabricated PLGA substrates were functionalized with sphingosine 1-phosphate (S1P; Cayman Chemical, MI, USA) or fluorescein-S1P (Echelon Biosciences, UT, USA) using 3,4-dihydroxy-L-phenylalanine (DOPA; Sigma Aldrich). A 2 mg/mL working solution of was generated by dissolving DOPA in 10 mM tris(hydroxymethyl)aminomethane (Tris; Fisher Scientific, NH, USA) buffer with a pH of 8.5. DOPA working solution was combined with a 500 µM S1P stock solution for each sample to achieve the appropriate S1P concentration. Samples were then incubated at room temperature overnight on a rocker. Afterwards, the DOPA-S1P solution was aspirated and substrates were washed three times with PBS before being dried using nitrogen gas. Substrates not functionalized with S1P were incubated with DOPA only.

C.3.3 Scanning Electron Microscopy (SEM)

S1P-functionalized nanopatterned substrates were sputter-coated with Au/Pd alloy prior to imaging, which was accomplished using a scanning electron microscope (Sirion XL30, FEI, OR, USA) at an accelerating voltage of 5 kV.

C.3.4 Atomic Force Microscopy (AFM)

An atomic force microscope (Dimension Icon-PT, Bruker, MA, USA) was used to measure the topography of nanopatterned substrates post-functionalization. The AFM was operated in non-contact mode with scan frequency of 0.5 Hz, and images were taken in 256 x 256 pixel resolution over a 10 µm x 10 µm area.

C.3.5 X-Ray Photoelectron Spectroscopy (XPS)

All XPS spectra were taken using a Surface Science Instruments S-probe spectrometer, and peak areas were determined using Service Physics ESCA2000A Analysis Software. X-ray spot size was approximately 800 µm, and pass energy for survey and high-resolution spectra was 150 eV and 50 eV, respectively. The take-off angle was approximately 55°, which translates to a sampling depth of approximately 50 Å. Three spots were analyzed on each PLGA sample (bare and functionalized).

C.3.6 Water Contact Angle Measurements

A 10 µL droplet of diH_2O was deposited onto substrates with DOPA and DOPA+S1P. Droplets were imaged and their contact angles with the substrates measured using a goniometer (FTA200, First Ten Ångstroms, VA, USA). Six samples of each group were used for these measurements.

C.3.7 Transgenic Mouse Generation

For all experiments in which primary muscle cells from transgenic mice were used, we utilized mice harboring the tamoxifen-inducible knock-in/knock-out *Pax7CreERT2* allele[33]. These were mated with mice homozygous for the mT/mG flox, heterozygous for the GCamP3 flox, and homozygous for the $S1P_1$ receptor to generate each respective Cre-lox system[34-36]. Reporter mice required only one generation to produce genotypes of *Pax7CreERT*$^{+/-}$ x *mT/mG*$^{+/-}$ or *Pax7CreERT*$^{+/-}$ x *GCamP3*$^{+/-}$. *Pax7CreERT*$^{+/-}$ x *S1P*$_1$ *flox*$^{+/+}$ mice were achieved within 3 generations by crossing F1 *Pax7CreERT*$^{+/-}$ x *S1P*$_1$

flox$^{+/-}$ with unrelated *S1P*$_1$ *flox*$^{+/+}$ animals. All mouse models were acquired from Jackson labs with the following catalog numbers: 012476, 007575, 014538, and 019141. Genotyping was accomplished using 1-2 mm tail clips that per collected and frozen in 1.5 mL Eppendorf tubes at -20°C until ready for processing. Genomic DNA was extracted by boiling tail snips at 95°C in 75 µL of 50 mM NaOH for approximately 1 hr, with vortexing every 15 minutes. Reactions were then neutralized by adding 25 µL 1M tris-HCl pH 6.8 and then samples were centrifuges at 13,000 g for 2 mins. Polymerase chain reaction (PCR) analysis was conducted using 1 µL of template from our extraction buffer in a final reaction of 20 µL with the Bioline 2x Master mix following the manufacturer's instructions. Primer pairs and polymerase reaction parameters are listed in **Table C.1**. NIH guidelines for the care and use of laboratory animals (NIH Publication #85-23 Rev. 1985) were observed throughout this study.

Table C.1. Primer sequences used to genotype transgenic mouse models used in this study.

Allele	Forward WT	Reverse WT	Forward Mutant	Reverse Mutant
Pax7Cre ERT2	N/A	N/A	ACTAGGCTCCACTCT GTCCTTC	GCAGATGTAGGGACA TCCCAGTG
mT/mG	AAGGGAGCTGCAGT GGAGTA	CCGAAAATCTGTGGG AAGTC	GGCATTAAAGCAGCG TATCC	CTGTTCCTGTACGGC ATGG
GCaMP3	CTTCAAGATCCGCCA CAACATCG	TTGAAGAAGATGGTG CGCTCCTG	CCAAAGTCGCTCTGA GTTGTTATC	GAGCGGGAGAAATG GATATG
S1P*$_1$ *flox	N/A	N/A	GAGCGGAGGAAGTTA AAAGTG	CCTCCTAAGAGATTG CAGCAA

C.3.8 Cell Isolation and Culture

Hind limb muscle mononuclear cells used in culture were isolated as previously described[17,37]. Briefly, three days prior to tissue harvesting, the tibialis anterior (TA), gastrocnemius and quadriceps muscles of both limbs in each mouse were injected with a 10 nM solution of cardiotoxin (CTX) from *Naja mossambica* (Sigma Aldrich) dissolved

in water. TA were injected with 50 µL, and gastrocnemius and quadriceps were injected with 100 µL each. Mice were sacrificed 3 days post-injury at the peak of satellite cell activation following CTX injury. The timing of collection was chosen to enrich mononuclear cell isolations with myogenic cells that are otherwise a minority in these skeletal muscles. Previous characterization of cells obtained using this isolation protocol have revealed that of the non-hematopoietic cell types, approximately 32% and 35% were comprised of myogenic and endothelial cells, respectively. The remainder of the cell population was comprised of fibroblasts and other non-myogenic cell types[37,38]. Injured muscles were harvested under sterile conditions and cleaned of any fat and tendons and then digested in a buffer containing both collagenase type IV and dispase II (Worthington Biochemical, NJ, USA) for a total of 45 min at 37°C. Cell/tissue mixtures were then transferred to warmed F10 medium (Hyclone, PA, USA) supplemented with 15% horse serum to inhibit enzyme digestion. The mixture was then passed sequentially through cell strainers with 70 µm and 40 µm mesh sizes to remove debris, muscle fibers, and multinucleated cells. Collected mononuclear cells were then seeded onto each respective substrate at a density of 50,000 cells/cm^2. Cells were maintained in F10 medium supplemented with 2 µM $CaCl_2$, 15% horse serum, and 20 ng/mL mouse basic fibroblast growth factor (bFGF), and media was changed every 4th day of culture. For induction of Cre-lox knock-in/knock-out in cells from transgenic mice, media was further supplemented for the first 4 days of culture with 20 µg/mL 4-hydroxytamoxifen (Sigma Aldrich). For vascular endothelial growth factor receptor 2 (VEGFR2) inhibition studies, media was supplemented with 5 µM cabozantinib (XL184; Selleck Chemicals, TX, USA) dissolved in dimethyl sulfoxide (DMSO).

C.3.9 Fluorescence Activated Cell Sorting

Isolated primary cells were resuspended in PBS with 1% BSA and incubated with fluorophore-conjugated mouse antibodies for CD31, CD34, CD45, α7 integrin, and Sca1 for 60 minutes at room temperature. Cells were then washed and resuspended in PBS with 2% PBS before being sorted into myogenic and endothelial cell populations as previously described.[90] Briefly, cells that were $CD31^{+}/CD45^{-}$ were sorted as endothelial cells, while cells that were $CD31^{-}/Sca1^{-}/CD34^{+}/\alpha7^{+}$ were sorted as myogenic cells.

C.3.10 Immunostaining and Fluorescence Microscopy

Cultures for imaging were fixed at day 10 with 4% paraformaldehyde in PBS for 10 minutes at room temperature before permeation with 0.1% Triton-X for 10 minutes. For myosin heavy chain staining, myotubes were incubated overnight at 4°C with purified mouse IgG against myosin heavy chain type I (1:100, BA-D5, Developmental Studies Hybridoma Bank, deposited by Schiaffino, S.), then with rabbit anti-mouse IgG conjugated with Alexa Fluor 647 (1:500 for 1 hour at room temperature). For endothelial cell identification, FITC-conjugated BS1 (1:500 for 1 hour at room temperature, Sigma-Aldrich) was utilized to stain cells for imaging. Staining for apoptosis was achieved using an antibody for cleaved caspase-3 (Cell Signaling Technology, MA, USA) diluted at 1:200. Antibodies for ceramide (Sigma Aldrich) and CerS2 (Boster Biological Technology, CA, USA) were also used at a 1:200 dilution for staining and imaging. F-actin was stained using Alexa Fluor 488-conjugated phalloidin (Invitrogen, CA, USA). All secondary antibodies were utilized at a 1:500 dilution. Nuclei were stained with DAPI (Invitrogen). Stained cells were then imaged using a Zeiss Axiovert 200 widefield

fluorescence microscope. Quantitative analysis of images was accomplished using ImageJ software (National Institutes of Health, MD, USA), and were conducted by two blinded researchers independently.

C.3.11 Gene Expression Quantification

After 10 days of culture, RNA from approximately 1 x 10^6 cells cultured cells was collected from 10 different cultures using the E.Z.N.A. Total RNA Kit I (Omega Bio-Tek, GA, USA) according to the manufacturer's protocol. Quantity and purity of RNA was determined by 260/280 nm absorbance. First-strand cDNA was synthesized from 1 µg of RNA using the high capacity cDNA synthesis kit from Applied Biosystems (CA, USA) per manufacturer's protocols using a randomized primer. The relative expression levels of selected genes were obtained using quantitative reverse-transcription polymerase chain reaction (qRT-PCR) analyses. cDNA of cultured cells in different condition (10 ng) was prepared using the Maxima SYBR Green/ROX qPCR master mix (Thermo Scientific, MA, USA). Reactions were processed by the ABI 7900HT PCR system with the following parameters: 50°C/2 min and 95°C/10 min, followed by 40 cycles of 95°C/15 s and 60°C/1 min. Results were analyzed using SDS 2.3 software, and relative expression was calculated using the comparative Ct method. Each sample was run in triplicate reactions for each gene. To examine myogenic differentiation and myogenic potential, *Pax7*, *Myf5*, *MyoD*, *MyoG* (myogenin), and *Myh15* were used as markers, while *CD31*, *Ve-Cad*, *vWF*, and *eNOS* were used as markers for the vascular differentiation of endothelial cells. Primers for the myogenic regulatory factors *Pax7*, *Myf5, MyoD* and *MyoG* were as previously reported[33]. Primers used for the vascular

related genes *CD31*, *Ve-Cad*, *vWF*, and *eNOS* were also as previously reported[39]. Primer pairs for *Myh15* were designed in-house and were (5'-TGA GCC TAA GAA AAA GCT GGG-3', forward) and (5'-CCA AAA CGC GAA GAG TTG TCA-3', reverse). For validation of the $S1P_1$ flox-out mouse model, primers used for assessing the expression of this receptor were as previously reported[40]. Primers for *Sphk1*, *Sphk2*, *Sgpp1*, *$S1P_1$*, *$S1P_2$*, and *$S1P_3$* were purchased from Bio-Rad Laboratories, Inc., and used as supplied. *GAPDH* was used as a housekeeping gene and conventional tissue culture polystyrene substrates with no S1P were used as a control in all analyses.

C.3.12 Calcium Imaging and Analysis

Fluorescent live cell videos at 20X magnification and an excitation wavelength of 488 nm were taken of contracting GCaMP3$^+$ myotubes. Videos were analyzed for fluorescence intensity using ImageJ. Peak fluorescence values from contracting myotubes were averaged for each condition across at least 20 fields of view. Videos were captured using a Zeiss Axiovert 200 widefield fluorescence microscope.

C.3.13 Correlation-based Contraction Quantification (CCQ)

Bright-field videos of contracting myotubes obtained at 20X magnification were analyzed using a custom MATLAB (MathWorks, MA, USA) script for CCQ that utilizes particle image velocimetry (PIV) and digital image correlation (DIC) algorithms[41]. In brief, an initial reference video frame is established and divided into a grid of windows of a set size. Each of these windows is run through a correlation algorithm with a subsequent frame, and any displacement that occurs between frames is converted into

a vector map. This map provides contraction angles, and when spatially averaged, contraction magnitudes and velocities. A Gaussian correlation peak with a probabilistic nature is used in the correlation equation, providing sub-pixel accuracy. The bright-field videos analyzed using CCQ were captured using a Nikon TS100 microscope at 30 frames per second.

C.3.14 Statistical Analyses

All quantitative data is presented as mean ± standard error of the mean (SEM). One-way ANOVA with Tukey's *post-hoc* multiple comparisons method was used to analyze data sets that include more than two experimental groups, while a Student's *t*-test was used to compare data sets looking at only two variables. In all analyses, a p value less than 0.05 was considered significant and n was defined by the number of discrete cultured substrates.

C.4 Results

Nanopatterned PLGA substrates were fabricated using capillary force lithography (CFL), a well-established and simple method that allows for the reproducible fabrication of substrates with high-fidelity nanoscale features across centimeter length scales (**Figure C.1a**)[42]. In this study, substrates featured aligned ridges and grooves that were 800 nm wide, as this nanotopography best mimicked native tissue ECM, and was previously shown to induce beneficial maturation effects on primary myoblasts[17]. PLGA substrates were then placed in a solution comprised of soluble S1P and DOPA, thereby

utilizing a “one-pot” functionalization scheme, the substrates could then be coated with the sphingolipid in a simple and effective manner. Surface functionalization with S1P did not negatively affect the patterned nanotopography, as scanning electron microscope (SEM) and atomic force microscopy (AFM) imaging revealed the maintenance of high pattern fidelity (**Figure C.1b**). Additionally, successful functionalization of substrates was confirmed using X-ray photoelectron spectroscopy (XPS), where nitrogen, phosphorous, and C-N bond peaks, characteristic of the S1P molecule, were present in conjunction with an attenuation of O-C=O and C=O bond peaks associated with the underlying PLGA (**Figure C.2**). To determine whether bound S1P would degrade over time in cell culture conditions, PLGA substrates were functionalized with fluorescein-S1P and incubated at 37°C for 10 days in PBS. PBS supernatant was collected throughout the 10-day period and their fluorescence, as well as that of the substrates at the beginning and end of the experiment, were measured using a fluorescent plate reader. It was found that substrate fluorescence was significantly greater than that of PLGA without S1P, and that their fluorescence values remained unchanged over time, while supernatant fluorescence remained at levels identical to that of ordinary PBS (**Figure C.3**). These results are indications that the S1P attached to substrates was not significantly degrading over this timeframe and under typical cell culture conditions.

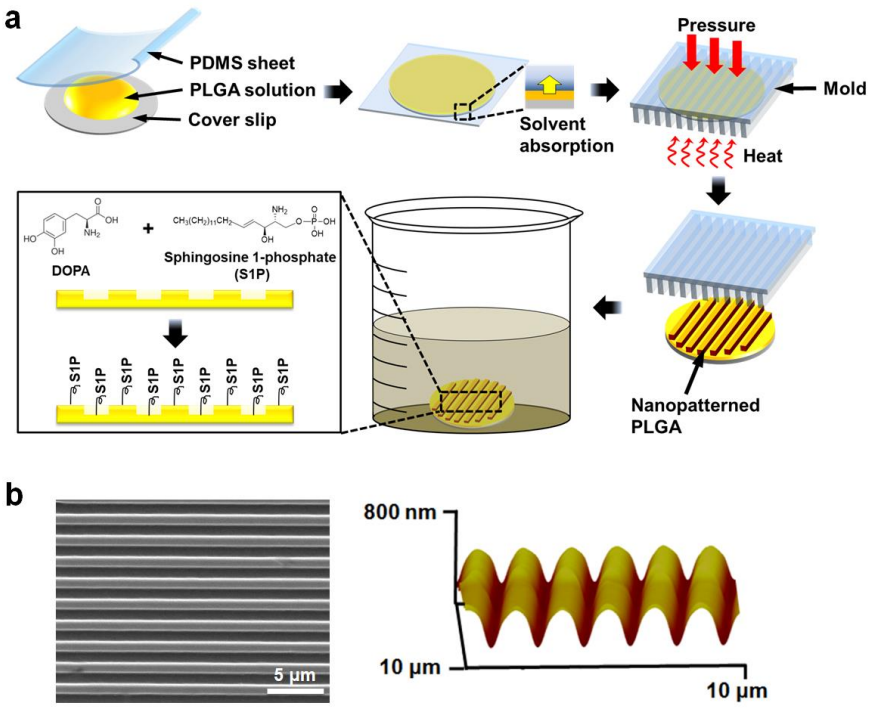

Figure C.1. Nanotopography fabrication and functionalization of biodegradable S1P-conjugated nanotopographically patterned substrates. (a) PLGA is nanopatterned using capillary force lithography and functionalized with S1P with one-pot DOPA-mediated chemistry. (b) Representative SEM and (b) AFM images of nanopatterned PLGA substrates post-functionalization with S1P.

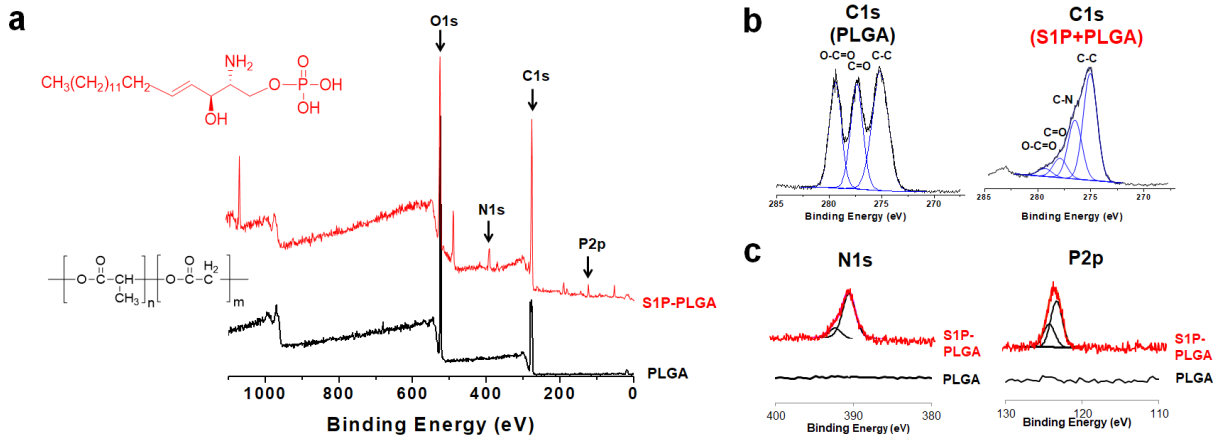

Figure C.2. XPS scans of non-functionalized and functionalized PLGA. (a) XPS analysis confirms S1P conjugation to substrate surfaces. Spectra shown is a survey scan in which nitrogen (N1s) and phosphorous (P2p) peaks characterstic of S1P appear post-functionalization (red spectra). (b) Comparative spectra of the C1s peak in which the signal from O-C=O and C=O bonds are attenuated due to the deposition of S1P, while a peak associated with the C-N appears. (c) The N1s and P2p peaks, which are not present on non-functionalized PLGA, appears post-functionalization.

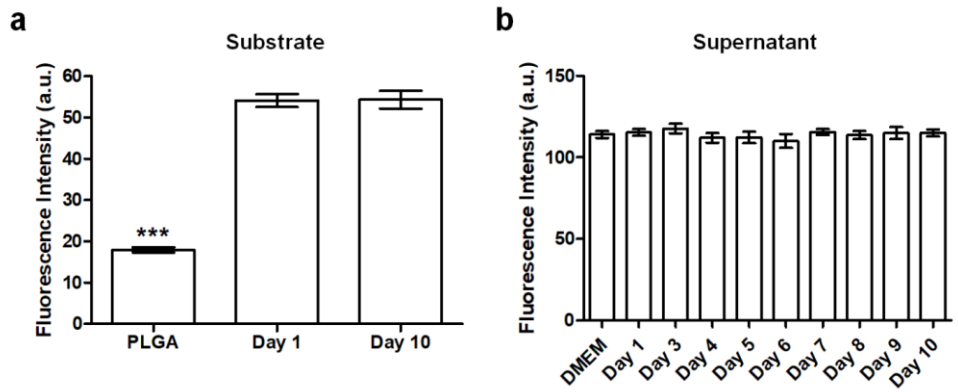

Figure C.3. Fluorescence measurements of S1P-functionalized substrates and collected phenol red-free DMEM supernatant. (a) No significant difference in substrate fluorescence was found between the beginning and end of the study, but values were significantly greater than that of non-functionalized substrates. (b) No significant difference was observed in fluorescence values compared to phenol red-free DMEM. All quantitative data are presented as means ± SEM, n=6 different substrates. ***$p < 0.001$ (one-way ANOVA with Tukey's post-hoc).

In order to distinguish myogenic cells from other populations present in skeletal muscle, we utilized the *Pax7-CreERT2* allele which is definitively expressed by the majority of satellite cells[43-46]. Transgenic mice harboring the *Pax7-CreERT2* and *mT/mG flox* alleles were generated to induce irreversible labeling of *Pax7* expressing myogenic cells with membrane localized GFP[34]. In this dual fluorescence fate-mapping model, non-myogenic cells were distinguishable by their expression of membrane localized tdTomato. Primary muscle cells from these mice were isolated from mouse limb muscles *via* enzymatic digestion and seeded onto flat and patterned substrates conjugated with S1P at varying concentrations (0, 50, 100, 175, and 250 μM). Cultures were maintained for 10 days and fixed for imaging or collected for gene expression analysis. These cultures were comprised of a heterogeneous mononuclear cell population that included satellite cells and their progeny, endothelial cells, and fibroblasts. As previously observed[17], nanopatterned substrates induced a greater degree of structural organization in the form of aligned myotubes (**Figure C.4a**). These

substrates also appeared to enhance the myogenic potential of cultured progenitor cells as a greater number of GFP^+ cells were observed in the patterned environment (**Figure C.4b**). Interestingly, myogenesis appeared to be S1P dose-dependent, as myotube count peaked at 175 μM S1P. These trends also held true when examining the fusion index (number of nuclei per myotube), with topography and S1P imparting a synergistic effect on myotube formation as a result of myoblast fusion. However, S1P at the highest concentration of 250 μM appeared to have a detrimental effect on myogenesis, as GFP^+ cell count and fusion index decreased sharply on both flat and patterned substrates under this condition. To further examine the maturation of the engineered muscle tissue, cultures of primary muscle cells from wild-type (WT) mice were stained for myosin heavy chain type I (MHC), an isoform of slow MHC expressed by mature muscles[47]. A significantly greater number of MHC-I^+ myotubes was observed on patterned substrates *versus* flat with most S1P concentrations. The greatest number of differentiated myotubes observed on patterned substrates was also with 175 μM of S1P, followed by a sharp decrease at 250 μM S1P (**Figure C.5a, b**).

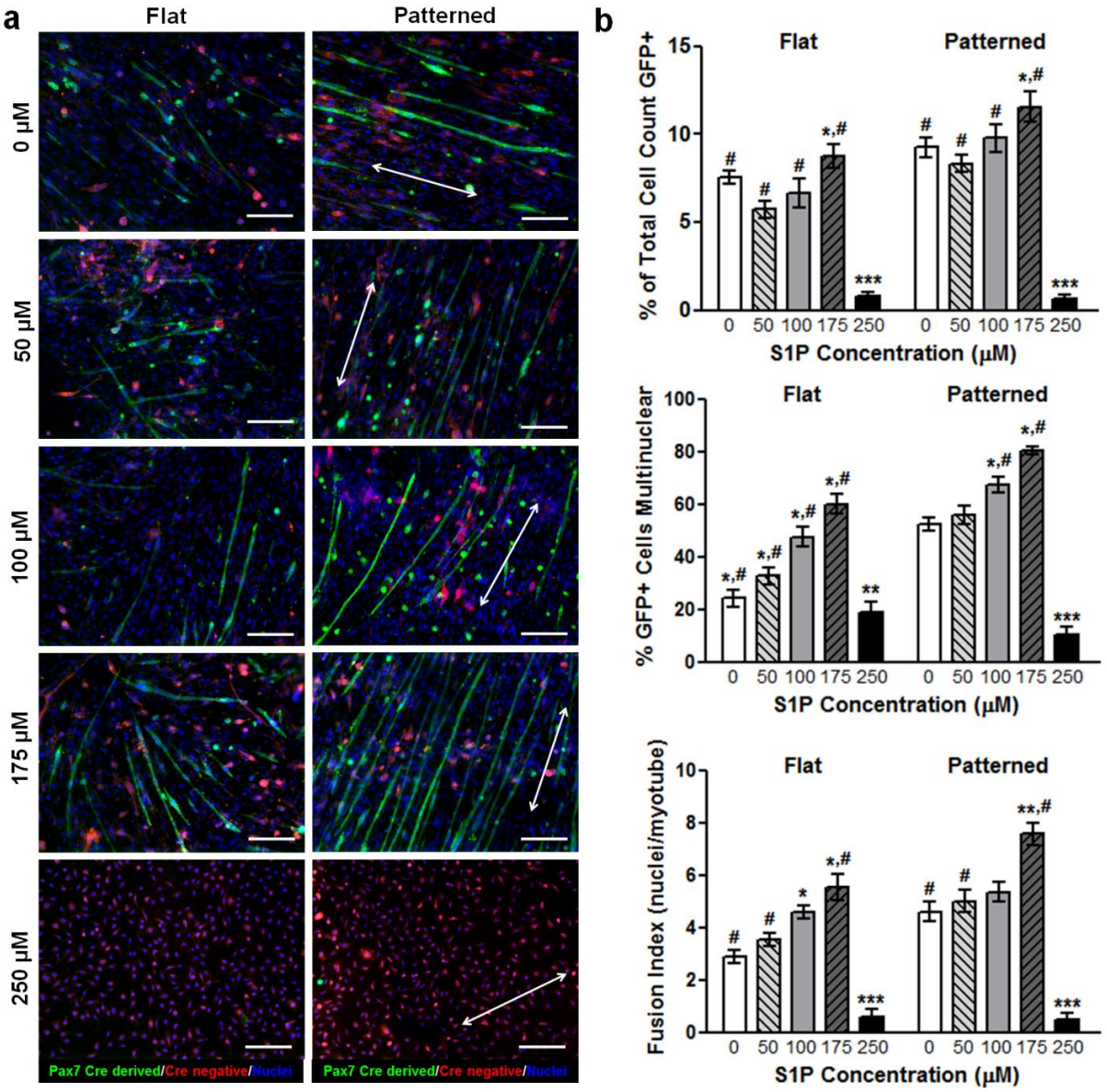

Figure C.4. S1P signaling and nanotopographical cues induce greater myogenic potential of cultured primary satellite cells and myoblasts. (a) Representative fluorescent images of cells and myotubes that are Pax7⁺ (green), which identifies them as either progeny of differentiated myogenic progenitor cells, or are progenitors themselves. Scale bars: 50 µm; direction of nanopatterning indicated by white double arrows. (b) Quantitative analyses of Pax7-GFP imaging for indicators of active myogenesis and myotube development. All quantitative data are presented as means ± SEM, n≥10 different cultures. *p < 0.05, **p < 0.01, ***p < 0.001 (comparing groups within substrate topography; one-way ANOVA with Tukey's *post-hoc*); #p < 0.05 (comparing flat vs. patterned at the same S1P concentration; Student's *t*-test).

Subsequently, we analyzed the transcriptional profile of myogenic regulatory factors to understand the mechanisms of S1P on myotube maturation that occurred in a dose-

dependent manner. The relative expression levels in cultured cells of several genes that spanned the spectrum of myogenic development were quantified using quantitative reverse-transcription polymerase chain reaction (qRT-PCR) analyses (**Figure C.5c**). As aforementioned, *Pax7* plays a critical role in the proper function of satellite cells and is therefore a well-established indicator of immature skeletal precursors (satellite cells). Examination of this gene revealed a significantly greater expression level in cells cultured on patterned substrates as compared to their flat substrate counterparts, regardless of S1P concentration. S1P-mediated expression also appeared to follow the previously observed biphasic trend. However, for patterned substrates, relative expression peaks at 100 μM S1P, rather than at 175 μM. In contrast to *Pax7,* which is specific for undifferentiating muscle precursors that can self-renew, *Myf5* is expressed in differentiating myoblasts and immature myocytes[48-50]. We observed that cells cultured on flat substrates exhibited greater expression levels of this gene compared to those cultured on patterned substrates, with no apparent differences due to S1P. The expression of *MyoD*, *MyoG* (myogenin) and *Myh15* (myosin heavy chain 15), which are expressed in late-stage or terminally differentiated muscle cells[51,52], was greater in cells not only on patterned substrates, but also significantly in cells on substrates with 175 μM S1P, regardless of underlying topography. Since a peak in expression of markers for more mature cells at 175 μM S1P was observed, it is plausible that this increase in maturation led to a corresponding lower expression of *Pax7* at this concentration of S1P. In all examined genes, there was a drastic decrease in expression levels in cells cultured on substrates functionalized with 250 μM of S1P.

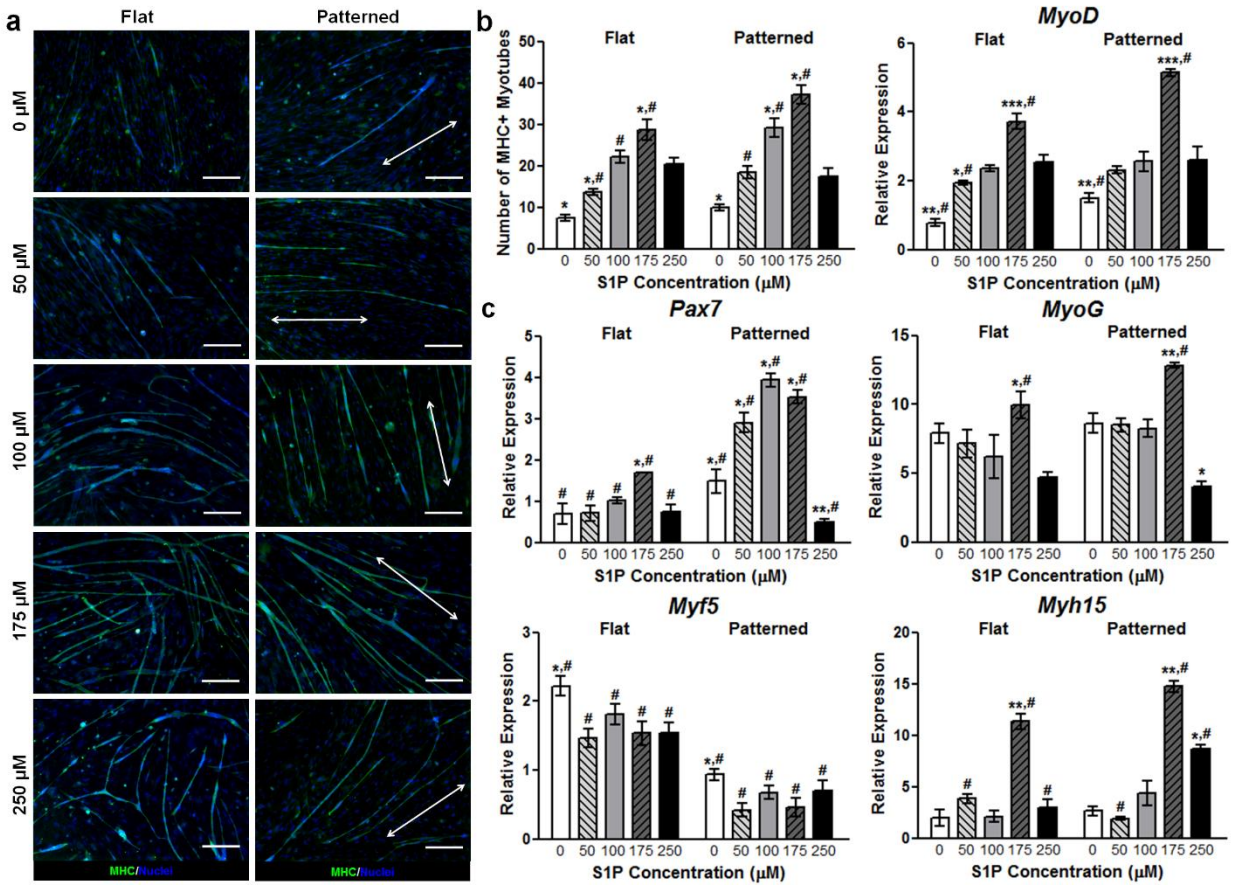

Figure C.5. S1P signaling and nanotopographical cues enhance the maturation of differentiated muscle cells. (a) Representative images of myotubes stained for MHC (pseudo-color in green). Scale bars: 50 μm; direction of nanopatterning indicated by white double arrows. (b) Images were analyzed for the total number of MHC^+ myotubes, with the greatest number seen on nanopatterned substrates functionalized with 175 μM S1P. (c) qRT-PCR analyses of primary muscle cells cultured on substrates for 10 days. Genes examined are markers representative of progenitor activation (*Pax7*) and various stages of myogenic differentiation, ranging from immature (*Myf5*) to more mature (*MyoD*, *MyoG*, *Myh15*). All quantitative data are presented as means ± SEM, n≥10 different cultures. *$p < 0.05$, **$p < 0.01$, ***$p < 0.001$ (comparing groups within substrate topography; one-way ANOVA with Tukey's *post-hoc*); #$p < 0.05$ (comparing flat vs. patterned at the same S1P concentration; Student's *t*-test).

Although the enhancement of myogenesis and maturation of the engineered skeletal muscle cultures was demonstrated with the aforementioned analyses, molecular markers of myogenesis are not direct indicators of muscle function. Thus, experiments were conducted to determine whether the maturation observed due to synergistic signaling from S1P and nanopatterning translated to improvements in myotube function. Using a correlation-based contraction quantification (CCQ) MATLAB script developed

by our lab[41], bright-field microscopy videos of contracting myotubes were analyzed. The maturation effects of biomimetic nanopatterning led to a corresponding improvement in myotube function, as myotubes on these substrates featured an average contraction displacement of 1.11 ± 0.13 μm, while those on flat substrates had an average contraction displacement of 0.79 ± 0.11 μm. Myotubes on nanopatterned substrates functionalized with 175 μM S1P exhibited an average contraction displacement of 3.37 ± 0.39 μm, while those cultured on functionalized flat substrates had an average displacement of 2.18 ± 0.36 μm (**Figure C.6a**). The addition of S1P led to a significant increase in displacement values for myotubes on both flat and patterned topographies, although patterning still led to a functional maturation advantage. A similar trend was observed in regard to the contraction velocities of myotubes, where significant increases occurred when nanotopography and S1P were present. Representative of the two ends of the spectrum, myotubes on nanopatterned substrates functionalized with 175 μM S1P had an average contraction velocity of 9.11 ± 1.18 μm/s, while myotubes on non-functionalized flat substrates had an average contraction velocity of 1.44 ± 0.34 μm/s (**Figure C.6b**).

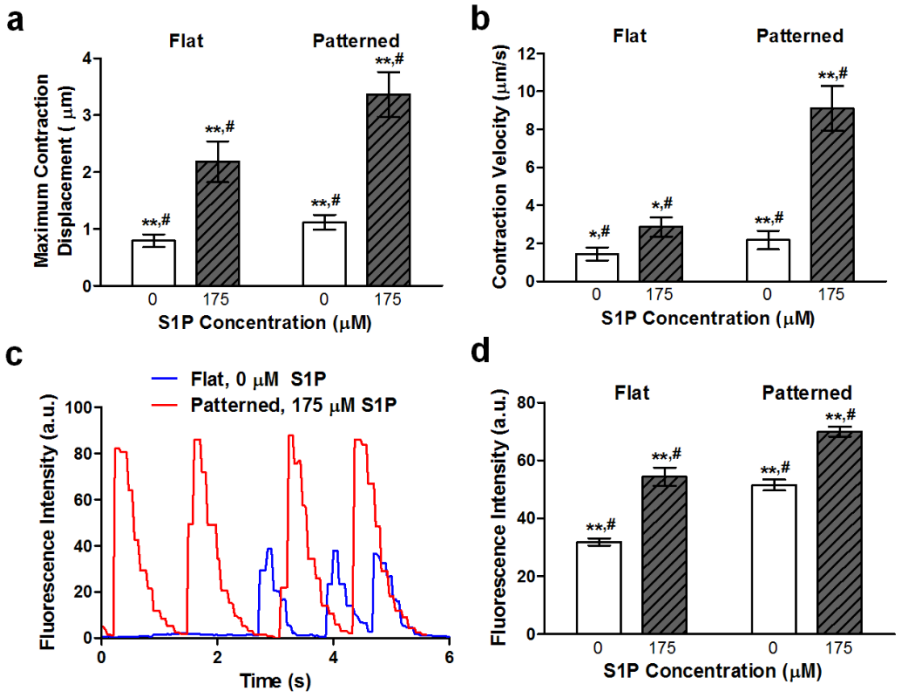

Figure C.6. Enhanced myogenic maturation leads to improved skeletal muscle tissue function. (a) The average contraction displacement of myotubes on flat or patterned substrates with and without 175 μM S1P. The combination of patterning and S1P led to the largest displacements. (b) The average contraction velocity of myotubes on flat or patterned substrates with and without 175 μM S1P. Myotubes developed from cells on patterned substrates functionalized with S1P contracted with the greatest velocities. (c) Representative traces of fluorescence intensity over time for myotubes on flat (blue) and nanopatterned substrates with 175 μM S1P (red) illustrating their respective contractile regularity. (d) Average fluorescence intensities of contracting GCaMP-expressing myotubes on flat or patterned substrates with and without 175 μM S1P. All quantitative data are presented as means ± SEM, n≥10 different cultures. *p < 0.05, **p < 0.01 (comparing groups within substrate topography; Student's *t*-test); #p < 0.05 (comparing flat vs. patterned at the same S1P concentration; Student's *t*-test).

S1P and nanotopography effects on myotube Ca^{2+} handling capabilities were examined by generating transgenic mice in which *Pax7CreERT2* expressing cells and their progeny would express GCaMP3, a well-characterized GFP-based calcium indicator for imaging Ca^{2+} dynamics in cells[36,53]. Once more, primary muscle cells were cultured on flat and patterned substrates with and without 175 μM S1P and imaged after 10 days with fluorescence live cell microscopy. Myotubes that had formed from these GCaMP3-expressing progenitor cells were observed to fluoresce as they spontaneously contracted, and the fluorescence intensity of these myotubes was tracked and plotted

over time. Interestingly, the contractile rhythm of myotubes differed based on culture conditions, where those on flat substrates contracted irregularly, while those on nanopatterned substrates with S1P exhibited more regular and consistent contractions (**Figure C.6c**). Quantification of the average fluorescence intensities revealed that myotubes cultured with S1P on nanopatterned substrates exhibited significantly greater levels of fluorescence corresponding to calcium ion flux, and thus an indication of improved calcium handling (**Figure C.6d**). Combined, the results of contraction and calcium dynamics analyses show that the increased expression of skeletal muscle maturation markers due to the combination of topographical and S1P signaling cues led to a corresponding enhancement of the engineered tissue's functional capabilities.

Primary cell cultures from wild-type mice were simultaneously stained with BS1 lectin, an endothelial cell marker[54] (green), and MHC (red) to examine the neovascularization potential of S1P-functionalized substrates (**Figure C.7a**). The potency of S1P as angiogenic factor was observed with increasing concentrations corresponding to a greater number of $BS1^+$ cells, regardless of topography. In contrast to myogenic indicators that peaked with 175 μM of S1P, the number of $BS1^+$ cells was greatest with 250 μM of S1P (**Figure C.7b**). On some of the 175 μM patterned substrates, $BS1^+$ cells appeared to organize themselves along the axis of myotubes. To confirm that the dose dependent increase of $BS1^+$ cells corresponded with a presence of active endothelial cells, we examined the transcription levels of angiogenic markers. The expression of genes related to endothelial adhesion (PECAM, *CD31*), function (von Willebrand factor, *vWF*), integrity (VE-cadherin, *Ve-Cad*), and vascular tone regulation (endothelial nitric oxide synthase, *eNOS*) were assessed quantitatively (**Figure C.7c**). A

correlation between S1P concentration and detection of endothelial transcripts was observed, with the greatest and most significant expression levels found in cells cultured on substrates functionalized with 250 μM S1P. In general, topography did not appear to play a significant role in regulating vascularization, although qualitatively alignment of vascular cells with myotubes was only observed on patterned substrates.

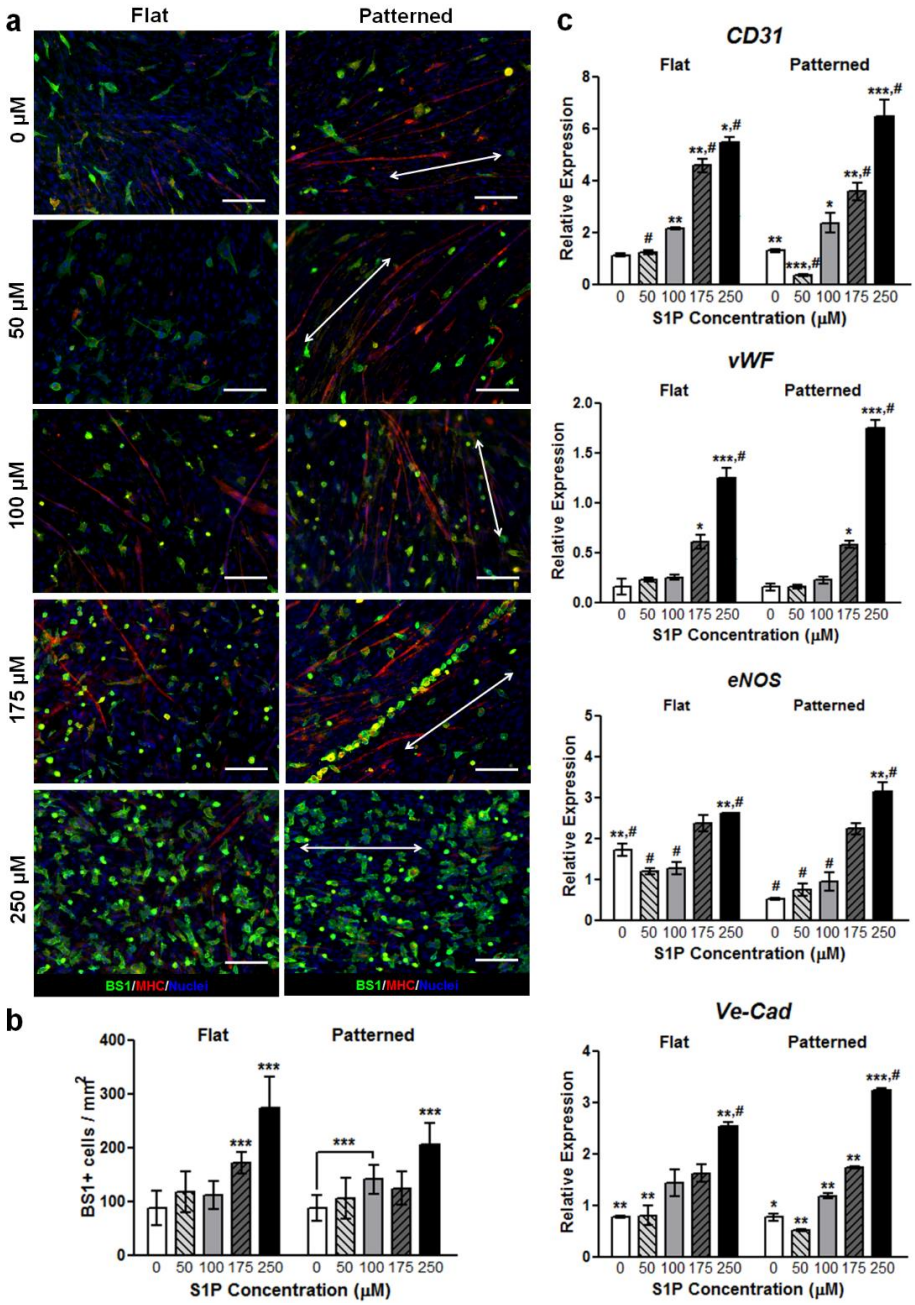

Figure C.7. S1P induces endothelial cell differentiation and enhanced pre-vascularization in a dose-dependent manner. (a) Staining for BS1 (pseudo-green), an endothelial cell marker, shows significantly greater numbers of $BS1^+$ cells on substrates with S1P, regardless of underlying nanotopography. Interestingly, some endothelial cells appear to localize around formed myotubes (pseudo-red). Scale bars: 50 µm; direction of nanopatterning indicated by white double arrows. (b) Quantification of BS1 staining, with the greatest number of positively-stained cells present on 250 µM S1P-functionalized substrates. (c) qRT-PCR assays show an increased expression of endothelial cell (CD31) and vascular development markers (*vWF*, *eNOS*, *Ve-Cad*) with respect to increasing S1P concentration. All quantitative data are presented as means ± SEM, n≥10 different cultures. *p < 0.05, **p < 0.01, ***p < 0.001 (comparing groups within substrate topography; one-way ANOVA with Tukey's *post-hoc*); #p < 0.05 (comparing flat vs. patterned at the same S1P concentration; Student's *t*-test).

To gain insight on the molecular mechanism by which S1P, in combination with nanotopography, modulates myogenesis, we examined the role of S1P receptor 1 ($S1P_1$) in myogenic cells. Although S1P signaling in skeletal musculature is highly complex and confers a variety of functions that are mediated mainly by S1P receptors 1 through 3[55], $S1P_1$ was chosen due to it being the most highly expressed in satellite cells during skeletal muscle regeneration, as well as in primary myoblasts cultured on nanopatterned substrates functionalized with 175 μM S1P (**Figure C.8**)[56,57]. We employed tamoxifen inducible genetic deletion of $S1P_1$ specifically in satellite cells by utilizing *Pax7CreERT2* mice that were homozygous for the *$S1P_1$ flox* allele[35]. To validate the effectiveness of the Cre-lox gene ablation, primary muscle cells from these and WT mice were cultured onto flat and patterned substrates functionalized with either no S1P or with 175 μM S1P for 10 days. Using qRT-PCR analysis, it was found that the expression of $S1P_1$ was significantly reduced in cells from *Pax7CreERT*$^{+/-}$ x *$S1P_1$ flox*$^{+/+}$ mice (**Table C.2**). Staining for MHC in myotubes formed from these cells revealed no significant difference in expression despite the presence of S1P, while patterned substrates induced greater expression of this protein compared to flat substrates (**Figure C.9a, b**). Furthermore, quantitative genetic analysis also revealed that topographical cues were still able to upregulate *Pax7* and *MyoG* expression, while S1P did not (**Figure C.9c**). Since $S1P_1$ was only knocked out in the myogenic cells that would eventually differentiate and form myotubes, the effects of S1P on endothelial cell maturation should be maintained. This was confirmed with qRT-PCR analysis of markers for vascular development (*CD31*, *Ve-Cad*), which showed significant

upregulation independent of substrate topography when these cells were exposed to S1P (**Figure C.9d**).

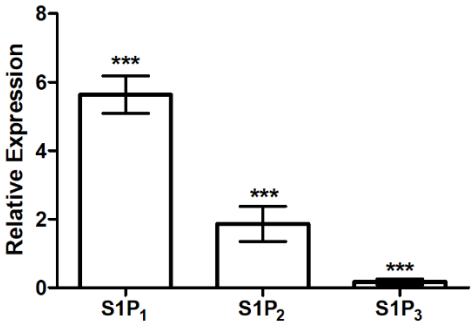

Figure C.8. Amongst S1P receptors, $S1P_1$ is expressed highest in primary murine myoblasts. Analysis of S1P receptor expression in primary myoblasts cultured on nanopatterned substrates functionalized with 175 µM S1P shows that expression of $S1P_1$ is greatest. All quantitative data are presented as means ± SEM, n=8 different cultures. ***p < 0.001 (one-way ANOVA with Tukey's *post-hoc*).

Table C.2. Expression of $S1P_1$ in cells from *Pax7CreERT*$^{+/-}$ x *S1P$_1$ flox*$^{+/+}$ mice relative to WT.

Culture Condition	**$S1P_1$ Expression Relative to WT**
Tissue culture polystyrene (TCPS)	0.00096 ± 0.00027
Flat PLGA	0.00161 ± 0.00032
Nanopatterned PLGA	0.00175 ± 0.00017
Flat PLGA + 175 µM S1P	0.00099 ± 0.00019
Nanopatterned PLGA + 175 µM S1P	0.00162 ± 0.00014
All conditions	**0.00139 ± 0.00017**

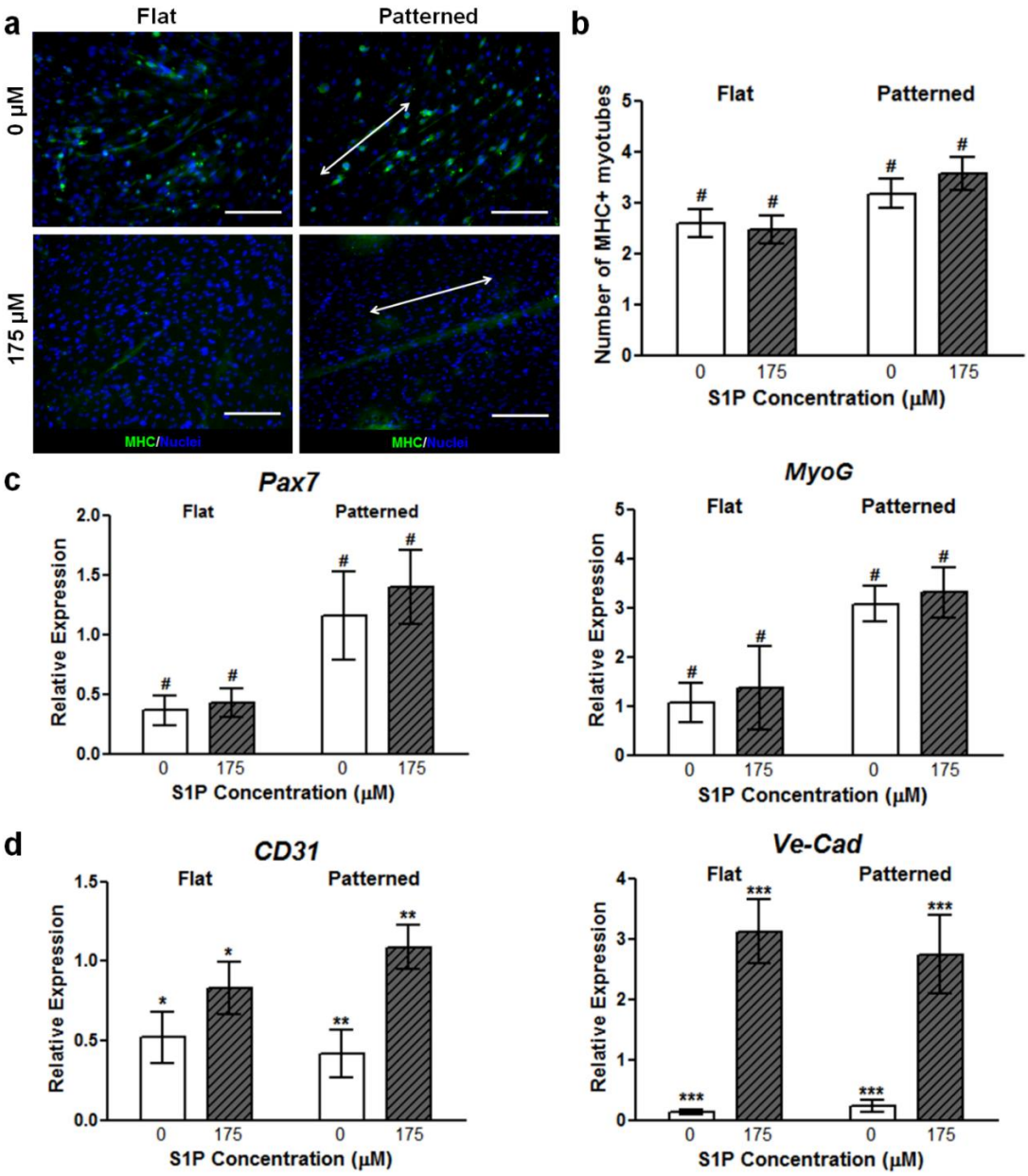

Figure C.9. Flox-out of $S1P_1$ results in predominantly nanotopography-mediated myogenic differentiation and maturation. (a) There is no significant difference in the number of MHC^+ myotubes when comparing functionalization states in $S1P_1$ flox-out cultures. However, myotube formation and alignment is still enhanced by nanopatterning. Scale bars: 100 μm; direction of nanopatterning indicated by white double arrows. (b) Quantification of MHC staining further illustrates the lack of S1P-induced myogenic maturation. (c) qRT-PCR of representative genetic markers for myogenesis, where marker expression is increased in the presence of biomimetic nanotopgraphy, but not in the presence of S1P. (d) Gene marker analysis of markers for endothelial cells and vascular integrity illustrate continued effect of S1P on non-myogenic cells. All quantitative data are presented as means ± SEM, n≥10 different cultures. *p < 0.05, **p < 0.01, ***p < 0.001 (comparing groups within substrate topography; Student's *t*-test); #p < 0.05 (comparing flat vs. patterned at the same S1P concentration; Student's *t*-test).

C.5 Discussion

From a scaffold design and engineering aspect, our results provide important insights into the utilization of DOPA-mediated chemistries for functionalizing synthetic materials with bioactive ligands. In our approach, a one-pot method where S1P and DOPA were added simultaneously to the substrates was used, as opposed to a sequential deposition of a DOPA coating followed by S1P conjugation to this layer. In theory, by using the one-pot technique, S1P is better able to form conjugates with free DOPA, thereby allowing for a denser packing of S1P molecules on a substrate. While others have reported success in functionalizing surfaces using this technique with dopamine[58,59], this study demonstrates the viability of one-pot functionalization when using DOPA. Of particular significance is the ability to utilize this technique to immobilize a lipid on a non-flat polymer-based substrate, which is a non-trivial task[60]. For example, when using conventional techniques for depositing biomolecules on nanopatterned substrates, such as microcontact printing, it is often difficult to ensure that the surface coverage of both ridges and grooves is achieved. Moreover, use of this DOPA-based technique allowed for the technically-challenging functionalization of a hydrolytically-degradable polymer (PLGA) with a poorly water-soluble biomolecule (S1P) under conditions that did not adversely affect the lipid's biological function.

Although the detailed mechanism for DOPA-mediated functionalization is still under investigation, the chemistry of catechol groups was recently demonstrated, and this mechanism may be involved in the attachment of S1P's α-amine to PLGA's catechol side group[61]. This would allow the long acyl chain and polar headgroup of S1P to remain free to interact with S1P receptors. Specifically, the phosphonate headgroup can

be surrounded by a ring of positively-charged polar residues provided by the receptor's capping N-terminal capping helix and helices III and VII, and the acyl chain can fully extend into the receptor's hydrophobic pocket with stable hydrophobic interactions[62,63]. Indeed, water contact angle measurements of substrates with and without S1P revealed that the functionalized substrates featured a more hydrophobic surface, with an average water contact angle of 75.34° ± 2.17°, compared to 62.54° ± 2.29° for bare PLGA (**Figure C.10**). However, while this data is indicative of S1P acyl chain integrity, it does not exclude the possibility that some degradation of the polar headgroup still occurs.

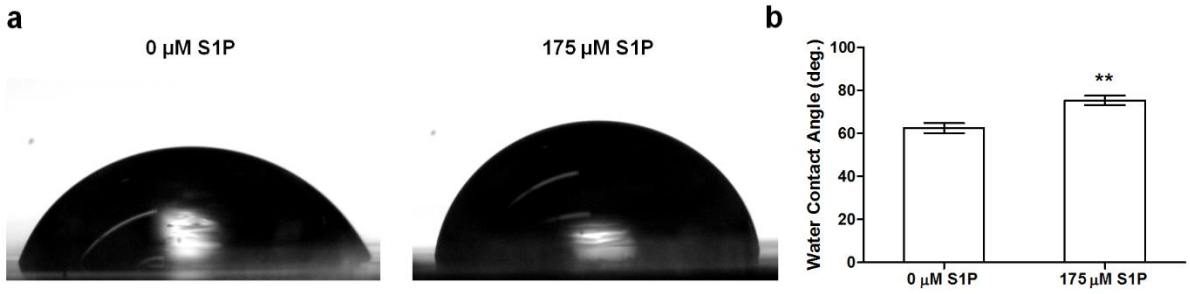

Figure C.10. Water contact angle measurements of PLGA substrates with and without S1P. (a) Representative images of a 10 µL droplet deposited onto each substrate type. (b) Water contact angles on S1P-functionalized substrates were significantly greater than those on non-functionalized substrates, indicating a more hydrophobic surface. All quantitative data are presented as means ± SEM, n=6 different substrates. **p < 0.01 (Student's *t*-test).

The significance of sphingolipids and the extent of their signaling has yet to be fully elucidated[64], and S1P in particular has been found to play a role in the regulation of a variety of critical cell processes, such as division, survival, migration, and adhesion[65-68], with recent studies suggesting that S1P is also involved in skeletal muscle regeneration. Under homeostatic conditions, low circulation concentrations of S1P (~ 2 µM) can be found in mammalian plasma; however, upon focal muscle injury, plasma S1P levels can increase by up to 50%[69]. There are strong indications that this increase in S1P synthesis and subsequent availability as a circulating ligand in response to injury is

required to mediate the migration, activation, and entry of satellite cells into the cell cycle in order to differentiate and form new muscle[30,31,56,70]. Our results appear to support these findings, as myogenic progenitor activation and differentiation significantly improved as S1P concentration increased, with a functionalization concentration of 175 μM eliciting a peak response. The finding of a larger presence of *Pax7*$^{+}$ cells present on patterned substrates conjugated with this concentration of S1P suggests that there is a greater induction of immature myoblast proliferation, or perhaps that there is a stable population of progenitor cells present that would enable the long-term differentiation and restoration of lost or damaged tissue. At the same time, lower expression levels of *Myf5* on patterned substrates, regardless of S1P, is an indication that in addition to the maintenance or recapitulation of the satellite cell niche, biomimetic nanotopographies also induce those cells that do become activated to readily differentiate towards the formation of mature skeletal muscle tissue. However, the expression of genes and proteins indicative of late stage myogenic maturation once again increased with S1P, and this corresponded with improved tissue function in the form of increased myotube contraction displacement and velocity, which can be translated to an increase in contractile force. The irregularity of the spontaneous contractions observed in myotubes on flat substrates *versus* those on functionalized patterned substrates is a further indication of the improved contractile machinery development due to nanotopographical and S1P signaling. The improved Ca^{2+} handling of myotubes on functionalized nanopatterned substrates is also a sign of tissue maturation attributed to enhanced myogenic development due to S1P, as S1P has been shown to increase intracellular calcium levels[71], with calcium in turn acting as a mediator of myoblast differentiation[72].

By mimicking the nanotopographical cues that would normally be seen by myoblasts and satellite cells *in vivo*, our aim was to recapitulate signaling cascades that would lead to improved functional maturation. While the role of specific mechanotransduction pathways in this process is still being elucidated, it has been demonstrated that Rho GTPases involved in cytoskeletal reorganization positively regulate MyoD expression and skeletal muscle differentiation[73]. It has also been found that in myoblastic cells, cytoskeletal remodeling and the formation of stress fibers promote the opening of stretch-activated channels and the subsequent increase in Ca^{2+} influx[74,75]. This is reflected in the data shown in **Figure C.6**, and since Ca^{2+} is an important second messenger for skeletal muscle differentiation, this is another potential mechanism for nanotopography-mediated maturation. Studies have also suggested that the PI3K/Akt pathway is involved in contact guidance and mechanotransduction signaling, and that activation of this pathway leads to skeletal muscle hypertrophy and myogenesis[76,77]. The benefits of biomimetic nanotopography is perhaps most apparent in the $S1P_1$ flox-out experiments where nanotopographical cues were still able to induce myotube formation, cellular alignment, and upregulated expression of late-stage maturation muscle maturation markers, even as the myogenic effects of S1P were being mitigated. It is possible that as part of the downstream effects of this mechanotransduction signaling, S1P is produced and secreted by the myogenic cells themselves *via* sphingosine kinases to induce S1P-mediated effects downstream[70]. To investigate this further, the relative expression levels of sphingosine kinase 1 (*Sphk1*), sphingosine kinase 2 (*Sphk2*), and sphingosine phosphatase 1 (*Sgpp1*) in both primary murine muscle cells and C2C12 myoblasts cultured on flat and patterned substrates with and

without S1P were analyzed. With the exceptions of an upregulation of *Sphk1* in primary myoblasts on substrates with no S1P and an upregulation of *Sgpp1* in C2C12 myoblasts on patterned substrates with S1P, no other significant differences in expression levels were observed (**Figure C.11**). The results suggest that kinase activity and S1P synthesis is unaffected by nanotopographical cues, and that in some cases, the lack of exogenous S1P induces an increase in the production of endogenous S1P. Furthermore, if the bulk of the maturation responses observed in this study were due to endogenously-formed S1P, we should expect to see similar levels of expression of maturation markers and functional capabilities in all cultures in which nanopatterning was present. Instead, we see a significant upregulation of these markers in addition to improvements in myotube function at higher concentrations of exogenous substrate-bound S1P. These results are thus an indication that there is a synergistic effect on functional maturation that is achieved when cells are subjected to both S1P signaling and nanotopographical cues, and that this effect is greatly enhanced by the S1P-functionalized nanopatterned substrates utilized in this study.

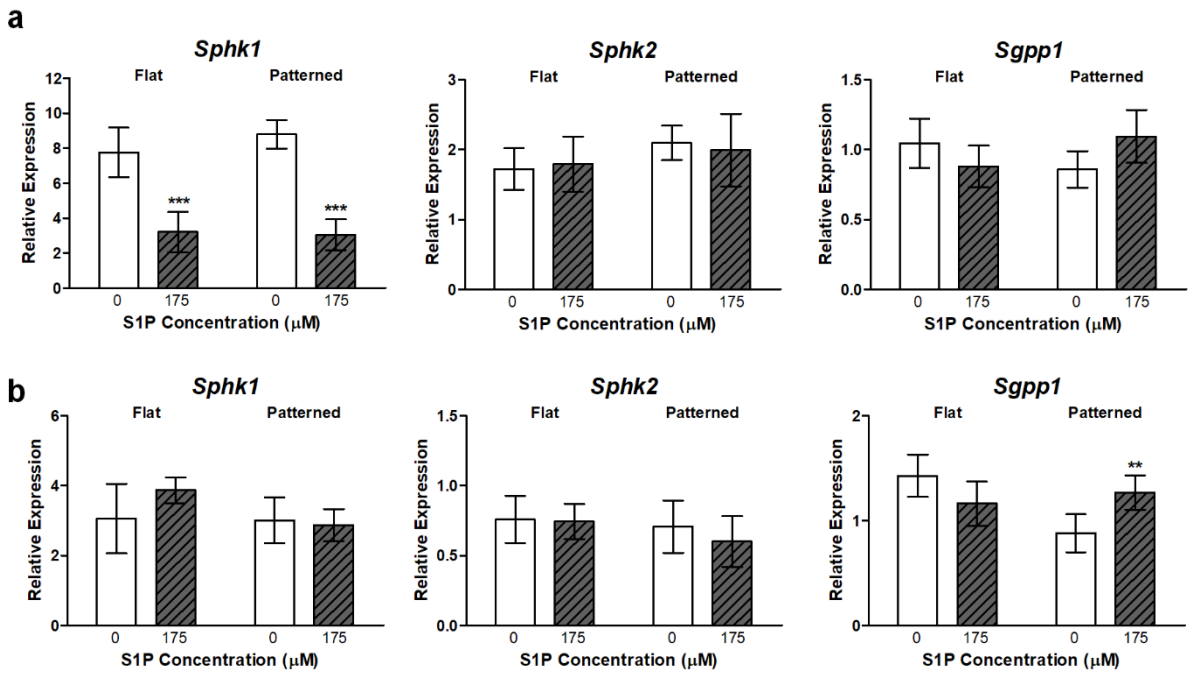

Figure C.11. Sphingosine kinase and phosphatase expression in myoblasts is not significantly changed by differences in nanotopography. The relative expression levels of *Sphk1*, *Sphk2*, and *Sgpp1* were assayed in (a) primary muscle cells and (b) C2C12 murine myoblasts cultured on flat and patterned substrates and with or without S1P. Significant differences in expression was only observed in the upregulated expression of *Sphk1* in primary cells cultured in S1P-free conditions, and in the upregulated expression of *Sgpp1* in C2C12 myoblasts on nanopatterned substrates functionalized with S1P. All quantitative data are presented as means ± SEM, n=6 different cultures. **p < 0.01, ***p < 0.001 (Student's *t*-test).

While the most effective concentration of S1P for muscle maturation in this study was found to be orders of magnitude greater than physiological levels, this may be a function of a situation in which the presented ligands are bound to a substrate, rather than being freely available in solution as it is the case *in vivo*. This could in fact provide an additional benefit when these muscle sheets are implanted. As the biodegradable substrates are broken down over time, bound S1P would be released locally and induce prolonged regeneration that would further enhance tissue development and function, even in dystrophic muscles[57].

In addition to inducing myogenic differentiation, S1P signaling has long been acknowledged to play a key role in vascular development and angiogenesis.

Specifically, it has been shown by others that vascular endothelial cells cultured with S1P exhibited increased motility, eNOS enzyme activity, and cell barrier integrity, leading to a corresponding increase in tube formation over time[28,78-80]. Additionally, disruption of S1P signaling *in vivo* results in blood flow dysregulation and vascular leakage due to junctional destabilization resulting from VE-cadherin mislocalization[35,81,82]. These pro-vascularization effects were also seen in this study with the increased expression of genetic markers for not only endothelial cell maturity, but also for vessel formation and stabilization. Furthermore, once implanted, the presence of S1P could also induce the migration of endothelial and vascular smooth muscle cells present in the host tissue to the implantation site and contribute to the formation of neovessels[29,83]. In addition to the long-term functional and survival benefits of generating vascularized skeletal muscle tissues, the presence of mature endothelial cells can also assist with myogenic development, since the secretion of VEGF from these cells has been shown to stimulate myotube hypertrophy and further improve myogenic differentiation[84]. Differentiating myogenic cells also secrete VEGF, and this could induce pronounced localized angiogenesis, thus creating a positive feedback loop in which reciprocal interaction between these two cell types can support continued angio-myogenesis[85]. This is perhaps best illustrated by the close juxtaposition of endothelial cells with myotubes present on nanopatterned substrates functionalized with 175 μM, which was shown to induce the greatest degree of myogenic differentiation and maturation. Indeed, when cells were cultured on flat and patterned substrates functionalized with 175 μM S1P were fed with media supplemented with 5 μM of cabozantinib (XL184), a potent VEGF receptor 2 (VEGFR2) inhibitor, markers for late-

stage and terminal skeletal muscle maturation (*MyoG, Myh15*) were downregulated in comparison to cultures without VEGFR2 inhibition (**Figure C.12a**). However, these markers were more expressed in cells cultured on nanopatterned substrates than in cells on flat substrates, indicating that mechanotransduction cues were still exerting an effect. Meanwhile, the expression of markers of vascular endothelial maturation (*eNOS, Ve-Cad)* was significantly downregulated in cultures with cabozantinib (**Figure C.12b**). Taken together, these results suggest that inhibiting VEGF function in these co-cultures reduces the benefits of engineering an environment in which mutually beneficial maturation can occur as it does *in vivo*.

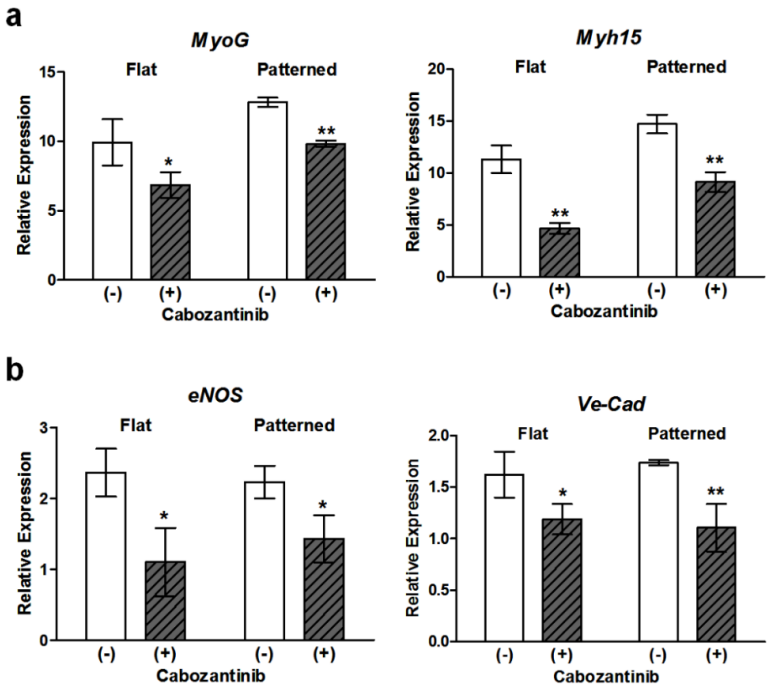

Figure C.12. Inhibition of VEGFR2 in cells cultured on substrates functionalized with 175 μM S1P results in reduced skeletal muscle and endothelial maturation. (a) Expression of markers for late-stage or terminal differentiation were significantly downregulated in comparison to cells in which VEGFR2 function was uninhibited. (b) Expression markers for vascular endothelial maturation were significantly downregulated in the presence of cabozantinib. All quantitative data are presented as means ± SEM, n=6 different cultures. *$p < 0.05$, **$p < 0.01$ (Student's *t*-test).

Interestingly, it was observed that there was an apparent biphasic dependence of myogenesis on S1P concentration, and that this trend did not carry over to vascular development. In fact, at the highest concentration tested (250 μM), the number of myoblasts and myogenic progenitors were greatly reduced in number and some even appeared to be apoptotic. Ceramide, a metabolite of S1P that is produced by the conversion of sphingosine *via* ceramide synthases (CerS), is generally associated with growth arrest and cell death[86-88]. Since this conversion is reversible, it has been proposed that it is the relative levels of these two lipid signaling molecules in response to external stimuli that determines cell fate, and thus acts as a "sphingolipid rheostat"[88,89]. Therefore, with the production of a large amount of ceramide at 250 μM S1P, this balance may have been shifted towards a pro-apoptotic state in myoblasts, thereby negating the beneficial myogenic effects of S1P. Immunostaining of cultures at this concentration of S1P for cleaved caspase-3, a marker for apoptosis, revealed that the percentage of apoptotic cells is in fact significantly greater than in controls (**Figure C.13**). However, it has been found that the activity of ceramide synthase 2 (CerS2) is inhibited by S1P, and that the distribution of CerS2 is greatest in highly-vascularized organs such as the liver and kidney[90]. It is then plausible that this inhibited activity of CerS2 in the cultured endothelial cells decreases the conversion rate of S1P to ceramide, and thus maintains the pro-angiogenic response of these cells to increased S1P stimulation. To further explore this hypothesis, primary cells were sorted into myoblast and endothelial cell populations before being cultured on substrates functionalized with 250 μM S1P and subsequently immunostained for ceramide and CerS2. In addition to displaying a more apoptotic morphology, ceramide accumulation

was found to be significantly greater in myoblasts than in endothelial cells. At the same time, CerS2 expression was found to be greater in endothelial cells which correlates with other findings in literature (**Figure C.14**)[91]. This data thus suggests that the inhibition of this specific synthase in endothelial cells is indeed helping with the shifting of the sphingolipid rheostat away from the overwhelming ceramide synthesis and resulting apoptosis seen in the myogenic cell population.

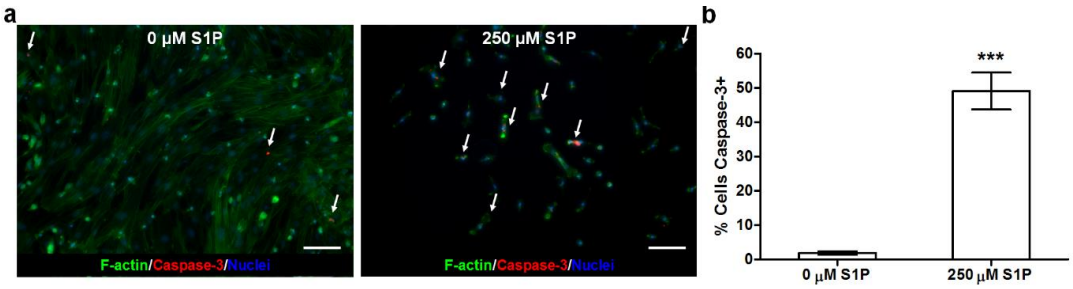

Figure C.13. Staining and quantification of cultures stained for a marker for apoptosis. (a) Representative images of cultures on PLGA substrates with no S1P and with 250 μM S1P. Cells are stained for F-actin (green) and cleaved caspase-3 (red). Scale bars:100 μm; cells stained positive for caspase-3 indicated by white arrows. (b) Quantitative analysis of images reveals a significantly greater percentage of cells stained positive for cleaved caspase-3 on substrates with 250 μM S1P. All quantitative data are presented as means ± SEM, n=6 different cultures. ***$p < 0.001$ (Student's *t*-test).

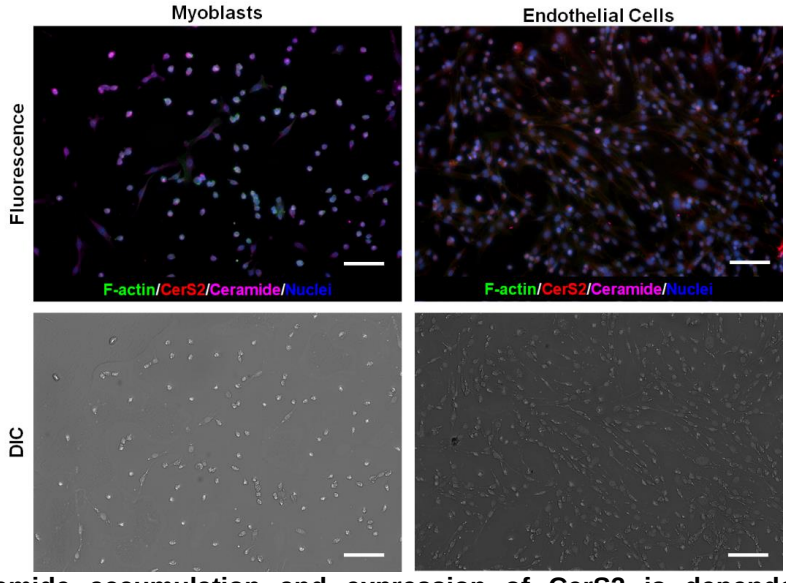

Figure C.14. Ceramide accumulation and expression of CerS2 is dependent on cell type. Representative fluorescent (top) and DIC (bottom) images of sorted myoblast and endothelial cell subpopulations cultured for 10 days on substrates functionalized with 250 μM S1P before being stained for F-actin (green), CerS2 (red), and ceramide (magenta). In addition to the presence of more cells with an apoptotic morphology, ceramide accumulation was significantly greater in myoblasts. Meanwhile, CerS2 expression was greater in endothelial cells than in myoblasts. Scale bars:100 μm.

While the capabilities of biomimetic nanotopographies on inducing cellular maturation have been reported on previously[17,92], the incorporation of the sphingolipid S1P as a ligand for simultaneously enhancing both the myogenic and neovascularization potential of cultured cells is an important aspect of this work. The resulting tissues were structurally ordered, and at higher S1P concentrations, were comprised of numerous differentiated and contracting myotubes, along with a sub-population of *Pax7*-expressing muscle precursors. Additionally, the increased expression levels of endothelial markers in these tissues is an indication of *in vitro* vascular development and improved potential for tissue integration and survival. In future work, by utilizing cell-sheet fabrication techniques that enable the generation of highly-ordered 3D tissues in a scaffold-free manner[93] and subsequently culturing these multi-layered constructs in the presence of S1P, it would be possible to create 3D skeletal muscle tissues that are primed for continued myogenic development and vascularization once implanted *in vivo*. Aside from their potential application as a form of implantable therapy for treating chronic or traumatic skeletal muscle loss, tissues generated using the techniques reported herein can also be considered as an effective *in vitro* platform for further characterizing the molecular mechanisms behind muscle development, as well as for disease modeling or drug screening.

C.6 References

1 Kalyani, R. R., Corriere, M. & Ferrucci, L. Age-related and disease-related muscle loss: the effect of diabetes, obesity, and other diseases. *Lancet Diabetes Endocrinol.* **2**, 819-829 (2014).

2 Puthucheary, Z. A. *et al.* Acute skeletal muscle wasting in critical illness. *J. Am. Med. Assoc.* **310**, 1591-1600 (2013).

3 MacKenzie, E. J. *et al.* Health-care costs associated with amputation or reconstruction of a limb-threatening injury. *J. Bone Joint Surg. Am.* **89**, 1685-1692 (2007).

4 Muramatsu, K., Doi, K. & Kawai, S. The outcome of neurovascularized allogeneic muscle transplantation under immunosuppression with cyclosporine. *J. Reconstr. Microsurg.* **10**, 77-81 (1994).

5 Collins, C. A. *et al.* Stem cell function, self-renewal, and behavioral heterogeneity of cells from the adult muscle satellite cell niche. *Cell* **122**, 289-301 (2005).

6 Montarras, D. *et al.* Direct isolation of satellite cells for skeletal muscle regeneration. *Science* **309**, 2064-2067 (2005).

7 Sacco, A., Doyonnas, R., Kraft, P., Vitorovic, S. & Blau, H. M. Self-renewal and expansion of single transplanted muscle stem cells. *Nature* **456**, 502-506 (2008).

8 Burdzinska, A. *et al.* Dynamics of acute local inflammatory response after autologous transplantation of muscle-derived cells into the skeletal muscle. *Mediators Inflamm.* **2014**, 482352 (2014).

9 Cosgrove, B. D., Sacco, A., Gilbert, P. M. & Blau, H. M. A home away from home: challenges and opportunities in engineering in vitro muscle satellite cell niches. *Differentiation* **78**, 185-194 (2009).

10 Fan, Y., Maley, M., Beilharz, M. & Grounds, M. Rapid death of injected myoblasts in myoblast transfer therapy. *Muscle Nerve* **19**, 853-860 (1996).

11 Qu, Z. *et al.* Development of approaches to improve cell survival in myoblast transfer therapy. *J. Cell Biol.* **142**, 1257-1267 (1998).

12 Qazi, T. H., Mooney, D. J., Pumberger, M., Geissler, S. & Duda, G. N. Biomaterials based strategies for skeletal muscle tissue engineering: existing technologies and future trends. *Biomaterials* **53**, 502-521 (2015).

13 Bach, A. D., Beier, J. P., Stern-Staeter, J. & Horch, R. E. Skeletal muscle tissue engineering. *J. Cell Mol. Med.* **8**, 413-422 (2004).

14 Gillies, A. R. & Lieber, R. L. Structure and function of the skeletal muscle extracellular matrix. *Muscle Nerve* **44**, 318-331 (2011).

15 Gillies, A. R. *et al.* High resolution three-dimensional reconstruction of fibrotic skeletal muscle extracellular matrix. *J. Physiol.* **595**, 1159-1171 (2017).

16 Juhas, M., Engelmayr, G. C., Jr., Fontanella, A. N., Palmer, G. M. & Bursac, N. Biomimetic engineered muscle with capacity for vascular integration and functional maturation in vivo. *Proc. Natl. Acad. Sci. U. S. A.* **111**, 5508-5513 (2014).

17 Yang, H. S. *et al.* Nanopatterned muscle cell patches for enhanced myogenesis and dystrophin expression in a mouse model of muscular dystrophy. *Biomaterials* **35**, 1478-1486 (2014).

18 Choi, J. S., Lee, S. J., Christ, G. J., Atala, A. & Yoo, J. J. The influence of electrospun aligned poly(epsilon-caprolactone)/collagen nanofiber meshes on the formation of self-aligned skeletal muscle myotubes. *Biomaterials* **29**, 2899-2906 (2008).
19 Auger, F. A., Gibot, L. & Lacroix, D. The pivotal role of vascularization in tissue engineering. *Annu. Rev. Biomed. Eng.* **15**, 177-200 (2013).
20 Levenberg, S. *et al.* Engineering vascularized skeletal muscle tissue. *Nat. Biotechnol.* **23**, 879-884 (2005).
21 Richardson, T. P., Peters, M. C., Ennett, A. B. & Mooney, D. J. Polymeric system for dual growth factor delivery. *Nat. Biotechnol.* **19**, 1029-1034 (2001).
22 Borselli, C. *et al.* Bioactivation of collagen matrices through sustained VEGF release from PLGA microspheres. *J. Biomed. Mater. Res. A* **92A**, 94-102 (2010).
23 Demirdogen, B., Elcin, A. E. & Elcin, Y. M. Neovascularization by bFGF releasing hyaluronic acid-gelatin microspheres: in vitro and in vivo studies. *Growth Factors* **28**, 426-436 (2010).
24 Karal-Yilmaz, O., Serhatli, M., Baysal, K. & Baysal, B. M. Preparation and in vitro characterization of vascular endothelial growth factor (VEGF)-loaded poly(D,L-lactic-co-glycolic acid) microspheres using a double emulsion/solvent evaporation technique. *J. Microencapsul.* **28**, 46-54 (2011).
25 Chen, R. R., Silva, E. A., Yuen, W. W. & Mooney, D. J. Spatio-temporal VEGF and PDGF delivery patterns blood vessel formation and maturation. *Pharm. Res.* **24**, 258-264 (2007).
26 Olwin, B. B. & Rapraeger, A. Repression of myogenic differentiation by aFGF, bFGF, and K-FGF is dependent on cellular heparan sulfate. *J. Cell Biol.* **118**, 631-639 (1992).
27 Pena, T. L., Chen, S. H., Konieczny, S. F. & Rane, S. G. Ras/MEK/ERK Up-regulation of the fibroblast KCa channel FIK is a common mechanism for basic fibroblast growth factor and transforming growth factor-beta suppression of myogenesis. *J. Biol. Chem.* **275**, 13677-13682 (2000).
28 Lee, O. H. *et al.* Sphingosine 1-phosphate induces angiogenesis: its angiogenic action and signaling mechanism in human umbilical vein endothelial cells. *Biochem. Biophys. Res. Commun.* **264**, 743-750 (1999).
29 Liu, Y. *et al.* Edg-1, the G protein-coupled receptor for sphingosine-1-phosphate, is essential for vascular maturation. *J. Clin. Invest.* **106**, 951-961 (2000).
30 Nagata, Y., Partridge, T. A., Matsuda, R. & Zammit, P. S. Entry of muscle satellite cells into the cell cycle requires sphingolipid signaling. *J. Cell Biol.* **174**, 245-253 (2006).
31 Rapizzi, E., Donati, C., Cencetti, F., Nincheri, P. & Bruni, P. Sphingosine 1-phosphate differentially regulates proliferation of C2C12 reserve cells and myoblasts. *Mol. Cell. Biochem.* **314**, 193-199 (2008).
32 Lee, H., Scherer, N. F. & Messersmith, P. B. Single-molecule mechanics of mussel adhesion. *Proc. Natl. Acad. Sci. U. S. A.* **103**, 12999-13003 (2006).
33 Lepper, C., Conway, S. J. & Fan, C. M. Adult satellite cells and embryonic muscle progenitors have distinct genetic requirements. *Nature* **460**, 627-631 (2009).

34 Muzumdar, M. D., Tasic, B., Miyamichi, K., Li, L. & Luo, L. A global double-fluorescent Cre reporter mouse. *Genesis* **45**, 593-605 (2007).
35 Allende, M. L., Yamashita, T. & Proia, R. L. G-protein-coupled receptor S1P1 acts within endothelial cells to regulate vascular maturation. *Blood* **102**, 3665-3667 (2003).
36 Zariwala, H. A. *et al.* A Cre-dependent GCaMP3 reporter mouse for neuronal imaging in vivo. *J. Neurosci.* **32**, 3131-3141 (2012).
37 Ieronimakis, N. *et al.* Absence of CD34 on murine skeletal muscle satellite cells marks a reversible state of activation during acute injury. *PloS One* **5**, e10920 (2010).
38 Ieronimakis, N., Balasundaram, G. & Reyes, M. Direct isolation, culture and transplant of mouse skeletal muscle derived endothelial cells with angiogenic potential. *PloS One* **3**, e0001753 (2008).
39 Pratumvinit, B., Reesukumal, K., Janebodin, K., Ieronimakis, N. & Reyes, M. Isolation, characterization, and transplantation of cardiac endothelial cells. *BioMed Res. Int.* **2013**, 359412 (2013).
40 Lo, C. G., Xu, Y., Proia, R. L. & Cyster, J. G. Cyclical modulation of sphingosine-1-phosphate receptor 1 surface expression during lymphocyte recirculation and relationship to lymphoid organ transit. *J. Exp. Med.* **201**, 291-301 (2005).
41 Macadangdang, J. *et al.* Nanopatterned Human iPSC-Based Model of a Dystrophin-Null Cardiomyopathic Phenotype. *Cell. Mol. Bioeng.* **8**, 320-332 (2015).
42 Suh, K. Y., Park, M. C. & Kim, P. Capillary force lithography: a versatile tool for structured biomaterials interface towards cell and tissue engineering. *Adv. Funct. Mater.* **19**, 2699-2712 (2009).
43 Seale, P. *et al.* Pax7 is required for the specification of myogenic satellite cells. *Cell* **102**, 777-786 (2000).
44 von Maltzahn, J., Jones, A. E., Parks, R. J. & Rudnicki, M. A. Pax7 is critical for the normal function of satellite cells in adult skeletal muscle. *Proc. Natl. Acad. Sci. U. S. A.* **110**, 16474-16479 (2013).
45 Zammit, P. S. *et al.* Pax7 and myogenic progression in skeletal muscle satellite cells. *J. Cell Sci.* **119**, 1824-1832 (2006).
46 Lepper, C., Partridge, T. A. & Fan, C. M. An absolute requirement for Pax7-positive satellite cells in acute injury-induced skeletal muscle regeneration. *Development* **138**, 3639-3646 (2011).
47 Torgan, C. E. & Daniels, M. P. Regulation of myosin heavy chain expression during rat skeletal muscle development in vitro. *Mol. Biol. Cell* **12**, 1499-1508 (2001).
48 Francetic, T. & Li, Q. Skeletal myogenesis and Myf5 activation. *Transcription* **2**, 109-114 (2011).
49 Cooper, R. N. *et al.* In vivo satellite cell activation via Myf5 and MyoD in regenerating mouse skeletal muscle. *J. Cell Sci.* **112 (Pt 17)**, 2895-2901 (1999).
50 Gunther, S. *et al.* Myf5-positive satellite cells contribute to Pax7-dependent long-term maintenance of adult muscle stem cells. *Cell Stem Cell* **13**, 590-601 (2013).

51 Wagers, A. J. & Conboy, I. M. Cellular and molecular signatures of muscle regeneration: current concepts and controversies in adult myogenesis. *Cell* **122**, 659-667 (2005).
52 Rossi, A. C., Mammucari, C., Argentini, C., Reggiani, C. & Schiaffino, S. Two novel/ancient myosins in mammalian skeletal muscles: MYH14/7b and MYH15 are expressed in extraocular muscles and muscle spindles. *J. Physiol.* **588**, 353-364 (2010).
53 Borges-Pereira, L., Campos, B. R. & Garcia, C. R. The GCaMP3 - A GFP-based calcium sensor for imaging calcium dynamics in the human malaria parasite Plasmodium falciparum. *MethodsX* **1**, 151-154 (2014).
54 Kalka, C. *et al.* Transplantation of ex vivo expanded endothelial progenitor cells for therapeutic neovascularization. *Proc. Natl. Acad. Sci. U. S. A.* **97**, 3422-3427 (2000).
55 Danieli-Betto, D. *et al.* Sphingosine 1-phosphate signaling is involved in skeletal muscle regeneration. *Am. J. Physiol., Cell Physiol.* **298**, C550-558 (2010).
56 Calise, S. *et al.* Sphingosine 1-phosphate stimulates proliferation and migration of satellite cells: role of S1P receptors. *Biochim. Biophys. Acta* **1823**, 439-450 (2012).
57 Ieronimakis, N. *et al.* Increased sphingosine-1-phosphate improves muscle regeneration in acutely injured mdx mice. *Skelet. Muscle* **3**, 20 (2013).
58 Kang, S. M. *et al.* One-step multipurpose surface functionalization by adhesive catecholamine. *Adv. Funct. Mater.* **22**, 2949-2955 (2012).
59 Kailasa, S. K. & Wu, H. F. One-pot synthesis of dopamine dithiocarbamate functionalized gold nanoparticles for quantitative analysis of small molecules and phosphopeptides in SALDI- and MALDI-MS. *Analyst* **137**, 1629-1638 (2012).
60 Nair, P. M., Salaita, K., Petit, R. S. & Groves, J. T. Using patterned supported lipid membranes to investigate the role of receptor organization in intercellular signaling. *Nat. Protoc.* **6**, 523-539 (2011).
61 Song, I. T. *et al.* PEGylation and HAylation via catechol: alpha-Amine-specific reaction at N-terminus of peptides and proteins. *Acta Biomater.* **43**, 50-60 (2016).
62 Rosen, H., Stevens, R. C., Hanson, M., Roberts, E. & Oldstone, M. B. Sphingosine-1-phosphate and its receptors: structure, signaling, and influence. *Annu. Rev. Biochem.* **82**, 637-662 (2013).
63 O'Sullivan, C. & Dev, K. K. The structure and function of the S1P1 receptor. *Trends Pharmacol. Sci.* **34**, 401-412 (2013).
64 Blaho, V. A. & Hla, T. An update on the biology of sphingosine 1-phosphate receptors. *J. Lipid Res.* **55**, 1596-1608 (2014).
65 Spiegel, S. & Milstien, S. Sphingosine-1-phosphate: an enigmatic signalling lipid. *Nat. Rev. Mol. Cell Biol.* **4**, 397-407 (2003).
66 Hla, T. Physiological and pathological actions of sphingosine 1-phosphate. *Semin. Cell Dev. Biol.* **15**, 513-520 (2004).
67 Aarthi, J. J., Darendeliler, M. A. & Pushparaj, P. N. Dissecting the role of the S1P/S1PR axis in health and disease. *J. Dent. Res.* **90**, 841-854 (2011).
68 Hannun, Y. A. & Obeid, L. M. Principles of bioactive lipid signalling: lessons from sphingolipids. *Nat. Rev. Mol. Cell Biol.* **9**, 139-150 (2008).

69 Loh, K. C. *et al.* Sphingosine-1-phosphate enhances satellite cell activation in dystrophic muscles through a S1PR2/STAT3 signaling pathway. *PloS One* **7**, e37218 (2012).
70 Sassoli, C. *et al.* Effects of S1P on skeletal muscle repair/regeneration during eccentric contraction. *J. Cell. Mol. Med.* **15**, 2498-2511 (2011).
71 Meacci, E. *et al.* Sphingosine 1-phosphate evokes calcium signals in C2C12 myoblasts via Edg3 and Edg5 receptors. *Biochem. J.* **362**, 349-357 (2002).
72 Porter, G. A., Jr., Makuck, R. F. & Rivkees, S. A. Reduction in intracellular calcium levels inhibits myoblast differentiation. *J. Biol. Chem.* **277**, 28942-28947 (2002).
73 Travaglione, S. *et al.* Cytotoxic necrotizing factor 1 hinders skeletal muscle differentiation in vitro by perturbing the activation/deactivation balance of Rho GTPases. *Cell Death Differ.* **12**, 78-86 (2005).
74 Formigli, L. *et al.* Sphingosine 1-phosphate induces cytoskeletal reorganization in C2C12 myoblasts: physiological relevance for stress fibres in the modulation of ion current through stretch-activated channels. *J. Cell Sci.* **118**, 1161-1171 (2005).
75 Benavides Damm, T. & Egli, M. Calcium's role in mechanotransduction during muscle development. *Cell. Physiol. Biochem.* **33**, 249-272 (2014).
76 Lai, K. M. *et al.* Conditional activation of akt in adult skeletal muscle induces rapid hypertrophy. *Mol. Cell. Biol.* **24**, 9295-9304 (2004).
77 Briata, P. *et al.* PI3K/AKT signaling determines a dynamic switch between distinct KSRP functions favoring skeletal myogenesis. *Cell Death Differ.* **19**, 478-487 (2012).
78 Garcia, J. G. *et al.* Sphingosine 1-phosphate promotes endothelial cell barrier integrity by Edg-dependent cytoskeletal rearrangement. *J. Clin. Invest.* **108**, 689-701 (2001).
79 Lee, M. J. *et al.* Vascular endothelial cell adherens junction assembly and morphogenesis induced by sphingosine-1-phosphate. *Cell* **99**, 301-312 (1999).
80 Igarashi, J. & Michel, T. S1P and eNOS regulation. *Biochim. Biophys. Acta* **1781**, 489-495 (2008).
81 Jung, B. *et al.* Flow-regulated endothelial S1P receptor-1 signaling sustains vascular development. *Dev. Cell* **23**, 600-610 (2012).
82 Gaengel, K. *et al.* The sphingosine-1-phosphate receptor S1PR1 restricts sprouting angiogenesis by regulating the interplay between VE-cadherin and VEGFR2. *Dev. Cell* **23**, 587-599 (2012).
83 Liu, F. *et al.* Differential regulation of sphingosine-1-phosphate- and VEGF-induced endothelial cell chemotaxis. Involvement of Gi α 2-linked Rho kinase activity. *Am. J. Respir. Cell Mol. Biol.* **24**, 711-719 (2001).
84 Bryan, B. A. *et al.* Coordinated vascular endothelial growth factor expression and signaling during skeletal myogenic differentiation. *Mol. Biol. Cell* **19**, 994-1006 (2008).
85 Christov, C. *et al.* Muscle satellite cells and endothelial cells: close neighbors and privileged partners. *Mol. Biol. Cell* **18**, 1397-1409 (2007).

86 Hannun, Y. A. & Obeid, L. M. The Ceramide-centric universe of lipid-mediated cell regulation: stress encounters of the lipid kind. *J. Biol. Chem.* **277**, 25847-25850 (2002).
87 Kolesnick, R. The therapeutic potential of modulating the ceramide/sphingomyelin pathway. *J. Clin. Invest.* **110**, 3-8 (2002).
88 Hait, N. C., Oskeritzian, C. A., Paugh, S. W., Milstien, S. & Spiegel, S. Sphingosine kinases, sphingosine 1-phosphate, apoptosis and diseases. *Biochim. Biophys. Acta* **1758**, 2016-2026 (2006).
89 Cuvillier, O. *et al.* Suppression of ceramide-mediated programmed cell death by sphingosine-1-phosphate. *Nature* **381**, 800-803 (1996).
90 Laviad, E. L. *et al.* Characterization of ceramide synthase 2: tissue distribution, substrate specificity, and inhibition by sphingosine 1-phosphate. *J. Biol. Chem.* **283**, 5677-5684 (2008).
91 Berdyshev, E. V. *et al.* FTY720 inhibits ceramide synthases and up-regulates dihydrosphingosine 1-phosphate formation in human lung endothelial cells. *J. Biol. Chem.* **284**, 5467-5477 (2009).
92 Carson, D. *et al.* Nanotopography-induced structural anisotropy and sarcomere development in human cardiomyocytes derived from induced pluripotent stem cells. *ACS Appl. Mater. Interfaces* **8**, 21923-21932 (2016).
93 Jiao, A. *et al.* Thermoresponsive nanofabricated substratum for the engineering of three-dimensional tissues with layer-by-layer architectural control. *ACS Nano* **8**, 4430-4439 (2014).

VITA

Jonathan H. Tsui was born in Mesa, AZ, and has also resided in Hong Kong and Woodland Hills, CA. He received his Bachelor of Science in Materials Science & Engineering from Cornell University in 2008 and his Master of Engineering in Biomedical Engineering from Cornell University in 2009. From 2009 to 2012, he worked as a Research Assistant in the Laboratory for Biomaterials and Drug Delivery at Boston Children's Hospital. He earned his Ph.D. in Bioengineering from the University of Washington in 2019.